8-2010

Robust Analysis of Electromagnetic Responses of Resonant Structures using Early-time and Low-Frequency Data

James Frye, jr.
Clemson University, frye.michael@gmail.com

ROBUST ANALYSIS OF ELECTROMAGNETIC RESPONSES OF RESONANT STRUCTURES USING EARLY-TIME AND LOW-FREQUENCY DATA

A Dissertation
Presented to
the Graduate School of
Clemson University

In Partial Fulfillment
of the Requirements for the Degree
Doctor of Philosophy
Electrical Engineering

---

by
J. Michael Frye
August 2010

Accepted by:
Dr. Anthony Q. Martin, Committee Chair
Dr. Chalmers M. Butler
Dr. Xiao-Bang Xu
Dr. Taufiquar R. Khan

ABSTRACT

Computational electromagnetic (CEM) methods and other numerical tools are a vital component of the design process used for many important applications, such as the development of antennas with the performance needed to meet requirements for modern wireless communications or the design of enclosures to harden electronic devices against electromagnetic interference (EMI). With CEM methods an engineer is provided the means to accurately simulate and study the EM behavior of a system or structure before constructing a physical prototype. Through repeated numerical simulations, the parameters of a structure can be adjusted and optimized to meet performance goals.

The rapid increase of affordable computing resources combined with the continued development and refinement of CEM methods has yielded a wide range of accurate and well-verified EM modeling tools; however, improvements are required to keep pace with the current and future requirements of EM systems. One such need is the development of robust, computationally-efficient methods which provide one the means to understand complex resonant systems through the by analyzing EM responses. The characteristics of resonant systems often make the determination of a wideband response with CEM methods computationally very intensive. Also, a numerical solution may not directly provide one with the physical insight needed to identify the characteristics of a complex system that influence its EM behavior. With a clear understanding of *why* a system behaves as it does, one can make better-informed choices on *how* to modify and design structures which have the desired properties. Even with the widespread use of optimization techniques, such as the genetic algorithm, to automate the search for an optimal combination of parameters, physical insight provides a valuable perspective. It can provide guidance in the design process and also allows one to better understand why a design works, which can lead to

additional ideas to pursue.

Procedures to efficiently and reliably extrapolate a wideband EM response of a resonant structure in the time- and frequency-domain are presented. Values of the response at discrete points in early time, low frequency, and space are determined with CEM methods, and the data are extrapolated to determine a representation of the complete response in time and frequency as a sum of weighted polynomials and pole terms. The representation is accurate and compact, and it is shown to provide valuable physical insight in the resonant behavior of the structure.

By fitting early-time and low-frequency numerical data a response can be simultaneously extrapolated in time and frequency. In 1999, Rao and Sarkar presented a technique to represent a response as a sum of weighted orthogonal polynomials; however, applying this technique to extrapolate a response of a resonant structure, which typically decays slowly in the time domain and is highly peaked in frequency domain, is computationally inefficient and often numerically unstable. Additionally, the accuracy of the extrapolation depends critically on the proper selection of several parameters. Selecting these parameters is very difficult in practice. In Chapter 1, a procedure is presented to address these limitations. Pole terms are incorporated into the representation of the response and are shown to accurately and efficiently model the effects of resonances. An optimization routine is developed that automates the selection of all the necessary parameters and provides confidence in the accuracy of the result. The advantages of the new procedure are demonstrated by extrapolating the wideband driving-point current of several antennas.

In Chapter 2, further improvements to the procedure in Chapter 1 are described, and three pole-estimation techniques are presented. It is shown that a response can be accurately extrapolated with poles estimated from either early-time data or low-frequency data. By comparing the two approaches, a time or frequency bias is discovered when estimating

poles from early-time or low-frequency data, respectively. A procedure to combine the sets of poles determined from early time and low frequency into a single set is also presented and shown to reduce the amount of CEM data needed to successfully apply the extrapolation procedure. The relative performance of the three pole-estimation methods is studied, and the combined method is used to extrapolate the responses of a multi-band antenna and a cavity structure of interest to EMI applications.

While responses at a single spatial location are of great practical importance, many applications require the determination of spatial responses. In Chapter 3, a reliable and computationally-efficient procedure to extrapolate a response defined in a general spatial region is developed by extending the procedure of Chapter 2, which is applicable to point responses. The spatial variation of the response can be accurately modeled with spatially-dependent polynomial coefficients and pole residues, and it is shown that a single set of poles, common to each discrete spatial location, is sufficient to describe the resonant behavior over the entire spatial region. In the representation of the response poles are either physical poles, which correspond to structural resonances, or fitting poles, which are not associated with resonances but can improve accuracy of the representation. Identifying the physical poles of a response is valuable but often difficult; however, a new procedure to automate this process is developed. The physical poles of a dipole are compared to complex natural resonances determined with the singularity expansion method (SEM), and the physical poles of a patch antenna are compared to the modes of a cavity model. The spatial variation of the residues of physical pole terms, referred to as modal residues, is found to provide valuable physical insight into the resonant behavior of a structure.

In Chapter 4, the use of modal residues for the analysis of antennas is explored. Modal residues, determined with the procedure of Chapter 3, are seen to be similar to the natural modes found with SEM. While applicable to many different types of resonant systems, the

modal residues of patch antennas are determined to demonstrate the value of the approach. The extrapolation procedure is applied to data corresponding to the electric field between the patch and ground plane for several antennas. It is found that the spatial distribution of the modal residues illustrate the influential parameters of each resonance and can be used to identify the resonances that will be excited for a given probe location. Additionally, the spatial variation of modal residues is seen to be similar to the input resistance at resonant frequencies as a function of the probe location. Rectangular and non-rectangular patch shapes are considered to illustrate the generality of the approach.

DEDICATION

This dissertation is dedicated to my wife, Karen.

ACKNOWLEDGMENTS

I would like to thank my advisor, Dr. Anthony Martin, for his assistance and guidance in preparing this dissertation and for all the support he's provided me. I would also like to thank Dr. Butler, Dr. Xu, and Dr. Khan for serving on my committee.

Finally, I would like to thank my mother for her constant encouragement and my family for their love and support.

TABLE OF CONTENTS

Page

Page

LIST OF FIGURES

Figure Page

CHAPTER 1
EXTRAPOLATION OF TIME AND FREQUENCY RESPONSES OF RESONANT ANTENNAS USING DAMPED SINUSOIDS AND ORTHOGONAL POLYNOMIALS

Abstract

A procedure is presented to extrapolate an electromagnetic response of a resonant structure by fitting early-time and low-frequency numerical data[1]. It has been shown that a wideband response can be extrapolated by fitting early-time and low-frequency data with a sum of orthogonal polynomials; however, extrapolating responses of resonant structures with this approach proves computationally inefficient and can lead to numerical instabilities. In this work, damped sinusoids are used in conjunction with polynomials to efficiently, accurately, and reliably extrapolate responses of resonant antennas. An automated procedure is described to select the necessary extrapolation parameters, and the wideband driving-point current of several resonant antennas is accurately extrapolated. The transmission-line matrix method and the method of moments are used to determine early-time and low-frequency data, respectively. Numerical data determined from fundamentally different spatial discretizations of the structure are successfully extrapolated, illustrating the independence of the procedure and the choice of computational methods used to provide the directly-computed data.

[1]The extrapolation procedure in this chapter is presented in [1] and the Master's thesis of the author. It is described again here to provide background for Chapters 2-4, which also focus on extrapolation procedures and extend the work of [1]. An appendix describing properties of associate Hermite functions is also included.

1.1 Introduction

To determine a wideband electromagnetic (EM) response of an antenna or structure, such as the driving-point current or an EM field value, one typically solves Maxwell's equations numericallu in either the time or frequency domain with a computational electromagnetic (CEM) method. If the structure has strong, or high-Q, resonances in the frequency range of interest, the numerical solution in both time and frequency domains is often computationally difficult. A time-domain CEM method can be used to determine a wideband response by exciting a structure with a narrow pulse, time-stepping until the transient response decays to zero, and applying a Fourier transform to the resulting response. Energy dissipation can be exceedingly slow for resonant structures, and consequently obtaining the complete time response can require thousands of time steps and significant computation times, especially for complex structures. Additionally, numerical dispersion can limit the accuracy of late time computations. Frequency-domain methods, on the other hand, require a separate evaluation at each frequency, which for wideband characterization can be difficult. Maintaining accuracy at higher frequencies generally requires increased spatial discretization, which leads to larger system matrices and greater computational expense. Additionally, sharp spikes near resonances necessitate fine sampling over the frequency range of interest.

In [2, 3, 4], it is shown that a response due to a wideband excitation can be simultaneously extrapolated in time and frequency by fitting early-time and low-frequency data. The response is approximated as a weighted sum of N orthogonal polynomials. This representation provides a *closed-form approximation* that can be evaluated at time and/or frequency points of interest, including late-time and high-frequency ranges where the respective responses are unknown (not determined with CEM methods). However, representing re-

sponses of resonant structures with polynomials alone, which typically decay slowly in the time-domain and are highly-peaked in the frequency domain, is computationally inefficient and often numerically difficult.

The extrapolation procedure in [2, 3, 4] is extended in this work by using M damped sinusoids in addition to N orthogonal polynomials to represent a response. Damped sinusoids provide the support to efficiently and accurately represent resonant behavior. Thus, fewer functions are needed to represent the response, computation time is decreased, and the accuracy of the extrapolation is improved [1, 5, 6, 7, 8]. Including M damped sinusoids allows multiple resonances to be represented. Consequently, wideband responses from multi-resonant structures, such as multi-band or cavity-type antennas can be extrapolated. The matrix pencil method (MPM) [9] is used to determine damped-sinusoid parameters by processing numerical values of the early-time response. Several other signal processing techniques, such as Prony's method [10], MUSIC [11], ARMA [12], and ESPRIT [13] have also been used to extract similar parameters from discrete time-domain data.

The stability and accuracy of the extrapolation procedure depends critically on the non-trivial selection of several parameters which define the polynomials and damped sinusoids. In this work, parameters are selected using a genetic algorithm (GA). This GA-based procedure automates the extrapolation of a response and provides confidence that an accurate result has been obtained.

The wideband driving-point current of several resonant antennas is extrapolated by representing the response as sums of damped sinusoids and polynomials. The performance is compared to extrapolation with only polynomials. The transmission-line matrix (TLM) method [14] is applied to determine the desired time-domain response, whereas the frequency-domain response is determined using the method of moments (MoM) to solve the electrical field integral equation (EFIE) [15]. These directly-computed responses pro-

vide early-time and low-frequency data, respectively, and are also used to assess the accuracy of the extrapolation. The two CEM methods selected employ fundamentally different discretizations of the structure of interest; however, the response can still be accurately extrapolated. In [2]-[4], the EFIE is solved in the time and frequency domain using an identical triangular surface patch discretization for both models. In this work, different spatial discretizations are used which illustrates the independence of the extrapolation procedure and the CEM methods used to generate the early-time and low-frequency data.

This chapter is organized as follows. In Section 1.2, an overview of extrapolation using orthogonal polynomials is presented. The incorporation of damped sinusoids is presented in Section 1.3. In Section 1.4, the use of a GA to select the necessary extrapolation parameters is described. Section 1.5 presents several numerical examples, and conclusions are discussed in Section 1.6. Properties of the Associate Hermite functions used to represent a response are presented in Appendix A.

1.2 Overview of Polynomial Extrapolation

The fundamental basis of the orthogonal polynomial extrapolation procedure in [2]-[4] is that the early-time and low-frequency portions of a wideband response contain mutually complementary information that can be used to generate the remaining late-time and high-frequency information. Early-time data contain high-frequency information whereas low-frequency data contain late-time information. Consequently, early-time and low-frequency data can be used to fit the response with a sum of weighted orthogonal polynomials which accurately represents the remaining late-time and high-frequency behavior. No new information is created, but rather numerical values of the response are processed to yield a representation of the complete response. Computationally, this approach is beneficial be-

cause low-frequency and early-time data are relatively easy to obtain by applying CEM methods. Early-time data points are determined first in time-stepping formulations and low-frequency evaluations are generally less demanding because the required level of spatial discretization increases with frequency.

Let $x(t)$ and $X(f)$ denote the time and frequency representations, respectively, of a response due to a wideband excitation. The response can be any electromagnetic quantity defined in both domains, such as the driving-point current of an antenna or the electric field at a point in space. A time-domain CEM method is used to determine an early-time portion of $x(t)$ whereas a frequency-domain method determines a low-frequency portion $X(f)$. Discretized versions of the structure of interest are developed and the response is determined at discrete time and frequency points. Each model is determined by the underlying numerical formulation utilized and may differ depending on the specific CEM method.

The discrete time-domain response $\mathbf{x}$ contains P data points sampled at Δt intervals and is partitioned into early-time and late-time data $\mathbf{x}_{\mathrm{ET}}$ and $\mathbf{x}_{\mathrm{LT}}$. The spatial discretization of the time-domain model typically dictates the value of Δt. The discrete frequency-domain response $\mathbf{X}$ contains Q data points sampled at Δf intervals and is partitioned into low-frequency and high-frequency data $\mathbf{X}_{\mathrm{LF}}$ and $\mathbf{X}_{\mathrm{HF}}$. The complete responses can be written as $\mathbf{x} = [\mathbf{x}_{\mathrm{ET}}; \mathbf{x}_{\mathrm{LT}}]$ and $\mathbf{X} = [\mathbf{X}_{\mathrm{LF}}; \mathbf{X}_{\mathrm{HF}}]$. A time-domain CEM method is used to compute $\mathbf{x}_{\mathrm{ET}}$ which contains the first p time samples of $\mathbf{x}$. A frequency-domain CEM method is used to compute $\mathbf{X}_{\mathrm{LF}}$ which contains the first q frequency points of $\mathbf{X}$.

The data vectors can be explicitly written as

$$\begin{aligned}
\mathbf{x}_{\mathrm{ET}} &= \left[x\left(t_1\right), x\left(t_2\right), \ldots, x\left(t_p\right)\right]^{\mathrm{T}} \\
\mathbf{x}_{\mathrm{LT}} &= \left[x\left(t_{p+1}\right), x\left(t_{p+2}\right), \ldots, x\left(t_P\right)\right]^{\mathrm{T}} \\
\mathbf{X}_{\mathrm{LF}} &= \left[X\left(f_1\right), X\left(f_2\right), \ldots, X\left(f_q\right)\right]^{\mathrm{T}} \\
\mathbf{X}_{\mathrm{HF}} &= \left[X\left(f_{q+1}\right), X\left(f_{q+2}\right), \ldots, X\left(f_Q\right)\right]^{\mathrm{T}}
\end{aligned} \tag{1.1}$$

where $t_j = (j-1)\,\Delta t$ and $f_j = (j-1)\,\Delta f$. The goal of the extrapolation is to use early-time and low-frequency data $\mathbf{x}_{\mathrm{ET}}$ and $\mathbf{X}_{\mathrm{LF}}$ to determine representations of the complete response which accurately represent late-time and high-frequency data $\mathbf{x}_{\mathrm{LT}}$ and $\mathbf{X}_{\mathrm{HF}}$.

Let the functions $\hat{x}(t)$ and $\hat{X}(f)$ denote the extrapolated representations of $x(t)$ and $X(f)$, respectively. To determine $\hat{x}(t)$ and $\hat{X}(f)$, both $x(t)$ and $X(f)$ are fitted by a sum of N orthogonal polynomials as

$$\begin{aligned}
x(t) \approx \hat{x}(t) &= \sum_{n=0}^{N-1} a_n \phi_n(t/\ell_1) \\
X(f) \approx \hat{X}(f) &= \sum_{n=0}^{N-1} a_n \Phi_n(f/\ell_2).
\end{aligned} \tag{1.2}$$

The functions $\phi_n\left(t/\ell_1\right)$ and $\Phi_n\left(f/\ell_2\right)$ in (1.2) represent nth-order polynomials [4] which are related by the Fourier transform and scaled by factors ℓ_1 and ℓ_2, where $\ell_1 = 1/\left(2\pi\ell_2\right)$. Appendix A presents a justification for (1.2) and describes the important parameters. As indicated in (1.2), a single set of N weighting coefficients $\mathbf{a}_N$ is used for both time and frequency representations. These coefficients can be determined by solving a system of linear equations which fits the representation in (1.2) with values of the response determined at each early-time and low-frequency point in $\mathbf{x}_{\mathrm{ET}}$ and $\mathbf{X}_{\mathrm{LF}}$, respectively [2].

The system of $(p+2q)$ equations to determine $\mathbf{a}_N$ can be written in matrix form as

$$\begin{bmatrix} \phi_0(t_1/\ell_1) & \cdots & \phi_{N-1}(t_1/\ell_1) \\ \vdots & \ddots & \vdots \\ \phi_0(t_p/\ell_1) & \cdots & \phi_{N-1}(t_p/\ell_1) \\ \mathrm{Re}\left\{ \begin{matrix} \Phi_0(f_1/\ell_2) & \cdots & \Phi_{N-1}(f_1/\ell_2) \\ \vdots & \ddots & \vdots \\ \Phi_0(f_q/\ell_2) & \cdots & \Phi_{N-1}(f_q/\ell_2) \end{matrix} \right\} \\ \mathrm{Im}\left\{ \begin{matrix} \Phi_0(f_1/\ell_2) & \cdots & \Phi_{N-1}(f_1/\ell_2) \\ \vdots & \ddots & \vdots \\ \Phi_0(f_q/\ell_2) & \cdots & \Phi_{N-1}(f_q/\ell_2) \end{matrix} \right\} \end{bmatrix} \begin{bmatrix} a_0 \\ \vdots \\ a_{N-1} \end{bmatrix} = \begin{bmatrix} x(t_1) \\ \vdots \\ x(t_p) \\ \mathrm{Re}\left\{ \begin{matrix} X(f_1) \\ \vdots \\ X(f_q) \end{matrix} \right\} \\ \mathrm{Im}\left\{ \begin{matrix} X(f_1) \\ \vdots \\ X(f_q) \end{matrix} \right\} \end{bmatrix} \tag{1.3}$$

where $\mathrm{Re}\{\cdot\}$ and $\mathrm{Im}\{\cdot\}$ denote the real and imaginary parts of the complex argument, respectively. The matrix equation of (1.3) can also be expressed as $\mathbf{B}\mathbf{a}_N = \mathbf{c}$ where $\mathbf{B}$, $\mathbf{a}_N$, and $\mathbf{c}$ have dimensions $(p+2q)\times N$, $N\times 1$, and $(p+2q)\times 1$, respectively. The N polynomials in (1.2) are evaluated to fill $\mathbf{B}$, data computed with CEM methods are used to fill $\mathbf{c}$, and $\mathbf{a}_N$ contains the N unknown polynomial coefficients. In practical cases $(p+2q) > N$ and (1.3) is an overdetermined system. A least-squares solution for $\mathbf{a}_N$ can be found using a variety of methods [16]. Singular value decomposition (SVD) is used in [2]-[4]. After determining $\mathbf{a}_N$ the representations of the responses are found by evaluating (1.2). If the extrapolation is successful, $\hat{x}(t)$ and $\hat{X}(f)$ closely approximate $x(t)$ and $X(f)$, including in the late-time and high-frequency ranges [2]-[4].

1.3 Incorporation of Damped Sinusoids

Accurately representing responses of resonant antennas, which characteristically decay slowly in the time-domain and are highly-peaked in the frequency-domain, can potentially require hundreds or thousands of orthogonal polynomials. The total number of polynomials N dictates the number of equations in (1.3), so computationally it is desirable to minimize N, while maintaining accuracy. Furthermore, rapid oscillations in higher-order polynomials can lead to computation errors and numerical instabilities [2, 3, 17, 18]. For these reasons, damped sinusoids are incorporated into (1.2) to accurately and efficiently represent responses of resonant structures.

The responses $x(t)$ and $X(f)$ can each be viewed as a superposition of two partial responses with distinct characteristics:

$$\begin{aligned} x(t) &= x^T(t) + x^R(t) \\ X(f) &= X^T(f) + X^R(f). \end{aligned} \tag{1.4}$$

In (1.4), $x^R(t)$ and $X^R(f)$ denote functions containing the resonant behavior of $x(t)$ and $X(f)$. Oscillation and exponential decay characterize $x^R(t)$, whereas spikes around resonant frequencies dominate the behavior of $X^R(f)$. The time and frequency forms of damped sinusoids exhibit this behavior and thus can efficiently represent $x^R(t)$ and $X^R(f)$. The remaining transient behavior of $x(t)$ and $X(f)$ is contained in $x^T(t)$ and $X^T(f)$. These functions decay rapidly in the time domain and are relatively smooth in the frequency domain. Accordingly, $x^T(t)$ and $X^T(f)$ are fitted by polynomials whose support can efficiently represent this behavior. By using two types of functions with distinct characteristics well suited to fit a specific behavior, the accuracy of the extrapolation is improved, and the computation time is decreased because fewer terms are needed.

The responses $x(t)$ and $X(f)$ are approximated by $\hat{x}(t)$ and $\hat{X}(f)$ which are sums of N orthogonal polynomials and M damped sinusoid terms:

$$\begin{aligned} x(t) \approx \hat{x}(t) &= \sum_{n=0}^{N-1} a_n \phi_n(t/\ell_1) + \sum_{m=0}^{M-1} g_m(t) \\ X(f) \approx \hat{X}(f) &= \sum_{n=0}^{N-1} a_n \Phi_n(f/\ell_2) + \sum_{m=0}^{M-1} G_m(f). \end{aligned} \tag{1.5}$$

In (1.5), the functions $g_m(t)$ and $G_m(f)$ represent the time and frequency forms of the mth damped sinusoids are related by the Fourier transform. In general, each pair is defined by amplitude constants, a resonant frequency, and an exponential decay or damping factor. The explicit forms of these functions are presented in Section 1.4, *B*. The addition of a single damped sinusoid with N polynomials can yield significant computational advantages when used to extrapolate a response dominated by one strong resonance [8]. The representation in (1.5), however, includes M damped sinusoids which allows for the efficient representation of multiple resonances.

In (1.5), $\mathbf{a}_N$ can be determined by isolating the portion of the response which is represented by the sum of polynomials. The M damped sinusoids are subtracted in (1.5) to yield an expression similar to (1.2) which equates the sum of polynomials directly with the response it approximates:

$$\begin{aligned} x(t) - \sum_{m=0}^{M-1} g_m(t) &\approx \sum_{n=0}^{N-1} a_n \phi_n(t/\ell_1) \\ X(f) - \sum_{m=0}^{M-1} G_m(f) &\approx \sum_{n=0}^{N-1} a_n \Phi_n(f/\ell_2). \end{aligned} \tag{1.6}$$

In (1.6), the terms containing the effects of resonances are subtracted from $x\,(t)$ and $X\,(f)$ and the resulting responses in the time- and frequency-domain are approximated as

a sum of N polynomials. Removing the resonant behavior allows the remaining response to be represented by polynomials alone. Observing the similarity between (1.6) and (1.2) reveals $\mathbf{a}_N$ in (1.6) can be determined using the matrix equation in (1.3) with the right-hand side **c** replaced by

$$\mathbf{c} = \begin{bmatrix} x(t_1) - \sum_{m=0}^{M-1} g_m(t_1) \\ \vdots \\ x(t_p) - \sum_{m=0}^{M-1} g_m(t_p) \\ \text{Re}\left\{ \begin{matrix} X(f_1) - \sum_{m=0}^{M-1} G_m(f_1) \\ \vdots \\ X(f_q) - \sum_{m=0}^{M-1} G_m(f_q) \end{matrix} \right\} \\ \text{Im}\left\{ \begin{matrix} X(f_1) - \sum_{m=0}^{M-1} G_m(f_1) \\ \vdots \\ X(f_q) - \sum_{m=0}^{M-1} G_m(f_q) \end{matrix} \right\} \end{bmatrix} \tag{1.7}$$

The expression for **c** in (1.7) incorporates the subtraction of the damped sinusoids in (1.6). With this approach a least-squares solution for $\mathbf{a}_N$ can be determined and used in (1.5) to construct $\hat{x}(t)$ and $\hat{X}(f)$ which, if the extrapolation is successful, accurately represent $x(t)$ and $X(f)$. Constants characterizing each damped sinusoid must be determined prior to solving for $\mathbf{a}_N$ because these functions are needed to fill **c** in (1.7). For an accurate extrapolation the damped sinusoids must precisely represent the resonances of the response.

1.4 GA-Based Selection of Extrapolation Parameters

To reliably extrapolate a wideband response the proper selection of several parameters is critical. Polynomial parameters must be carefully chosen to yield accurate and stable results. If the representation also contains damped sinusoids, then constants defining each term must be determined. In this work GA optimization is used to automate the selection process. The Powell method has also been applied to the nonlinear problem of selecting polynomial parameters [19].

The objective is to determine a set of parameters which minimize the difference between the extrapolated responses $\hat{x}(t)$ and $\hat{X}(f)$, and the true responses $x(t)$ and $X(f)$. This difference E can be quantified using a normalized root-mean-square (RMS) comparison as

$$E = \frac{1}{2}\left\{ \frac{\|\mathbf{x} - \hat{\mathbf{x}}\|}{\|\mathbf{x}\|} + \frac{\left\|\mathbf{X} - \hat{\mathbf{X}}\right\|}{\|\mathbf{X}\|} \right\} \tag{1.8}$$

where $\|\cdot\|$ denotes the $l^2 -$ norm, e.g. $\|\mathbf{x}\| = \frac{1}{P}\sqrt{\sum_{i=1}^{P} |x\,(i\Delta t)|^2}$. The leading $1/2$ is included to average differences in the time and frequency domains. Computing E in (1.8) requires complete knowledge of $\mathbf{x}$ and $\mathbf{X}$; however, in practice only $\mathbf{x}_{\mathrm{ET}}$ and $\mathbf{X}_{\mathrm{LF}}$ are available because $\mathbf{x}_{\mathrm{LT}}$ and $\mathbf{X}_{\mathrm{HF}}$ must be extrapolated. Therefore, an estimate of E using only $\mathbf{x}_{\mathrm{ET}}$ and $\mathbf{X}_{\mathrm{LF}}$ is desired.

It has been found in this work that E can be estimated by $\hat{E}$, defined as

$$\hat{E}_i = \frac{1}{2}\left\{ \frac{\|\mathbf{x}_{\mathrm{ET}} - \hat{\mathbf{x}}_{\mathrm{ET}}\| + \left\| IFFT\left\{\hat{\mathbf{X}}\right\}_{\mathrm{LT}} - \hat{\mathbf{x}}_{\mathrm{LT}} \right\|}{\|\mathbf{x}_{\mathrm{ET}}\|} + \frac{\left\|\mathbf{X}_{\mathrm{LF}} - \hat{\mathbf{X}}_{\mathrm{LF}}\right\| + \left\| FFT\left\{\hat{\mathbf{x}}\right\}_{\mathrm{HF}} - \hat{\mathbf{X}}_{\mathrm{HF}} \right\|}{\|\mathbf{X}_{\mathrm{LF}}\|} \right\} \quad (1.9)$$

In (1.9), FFT and $IFFT$ denote the fast Fourier transform and its inverse, respectively. At early-time and low-frequency points, agreement is calculated by computing the norm of the difference between the extrapolated and directly-computed CEM data. These comparisons correspond to the first expressions in the numerator of both terms in (1.9). In late-time and high-frequency ranges CEM data are not available to compare with, and therefore the FFT and $IFFT$ are utilized to estimate agreement in these ranges. The late-time portion of the extrapolated time data $\hat{\mathbf{x}}_{\mathrm{LT}}$ is compared to the late-time portion of the $IFFT$ of the complete extrapolated frequency response $\hat{\mathbf{X}}$. Similarly, the high-frequency portion of the extrapolated frequency data $\hat{\mathbf{X}}_{\mathrm{HF}}$ is compared to the high-frequency portion of the FFT of the complete extrapolated time response $\hat{\mathbf{x}}$. The norms of the known data $\mathbf{x}_{\mathrm{ET}}$ and $\mathbf{X}_{\mathrm{LF}}$ are used to normalize the terms in $\hat{E}$. To reliably extrapolate a response a GA is used to minimize $\hat{E}$ in (1.9) as a function of the necessary extrapolation parameters. Sections *A* and *B* explicitly describe the parameters which must be selected.

Optimization times can be decreased by reducing the computations required to solve the system of equations in (1.3) to determine $\mathbf{a}_N$. In addition to SVD, several other techniques [16] can be used to determine the least-squares solution of (1.3). One computationally efficient approach is the pseudo-inverse of $\mathbf{B}$. With this approach the polynomial coefficients are computed as $\mathbf{a}_N = (\mathbf{B}^*\mathbf{B})^{-1}\mathbf{B}^*\mathbf{c}$, where $\mathbf{B}^*$ denotes the conjugate transpose of $\mathbf{B}$

and $(\mathbf{B}^*\mathbf{B})^{-1}$ denotes the inverse of the square matrix $\mathbf{B}^*\mathbf{B}$. For the responses considered here, using either SVD or the pseudo-inverse to solve (1.3) did not affect the extrapolation accuracy obtained; however, the pseudo-inverse solution is significantly faster. Optimization times can be further reduced by checking the condition number of the square matrix before computing the pseudo-inverse. If the condition number is large for a given set of parameters, then the pseudo-inverse solution will likely be inaccurate and the extrapolation numerically unstable. Therefore, no further calculations are needed, and the GA fitness value can be automatically penalized. For a parameter set with a large condition number, the quantities $\hat{\mathbf{x}}$, $\hat{\mathbf{X}}$, and $\hat{E}$ need not be determined, and thus the computation time is reduced. The additional burden of checking the condition number is offset by the time savings it produces. The pseudo-inverse and condition number check are utilized for the examples in Section 1.5.

A. Orthogonal Polynomial Parameters

The accuracy and stability of the polynomial extrapolation depends critically on the selection of N and the scaling factor ℓ_1 [2]-[4]. Empirical stability bounds for N and ℓ_1 have been presented for several polynomial types [18]; however, there remain no precise criteria to select the optimal values to represent an arbitrary response. Consequently, in this work both N and ℓ_1 are set as GA optimization variables with their range defined by applying the bounds in [18]. For the numerical examples in Section 1.5, associate Hermite (AH) functions are used as the polynomials which represent the response. Appendix A describes some important properties of AH functions. Laguerre and Bessel-Chebyshev functions could also have been used [4], [18]; however, for a convergent extrapolation the performance with each polynomial considered is nearly the same [4].

Because AH functions provide equal support around their origin and it is assumed that

$x(t) = 0$ for $t \leq 0$, it is beneficial to center each polynomial around $t = \tau$, rather than at $t = 0$ [2, 3]. Typically, the optimal time center is around half of the time support of the response [2, 3], but again no precise selection criteria exists, so τ is selected as a third optimization variable. Thus, when representing a response as a sum of polynomials, a GA is used to minimize $\hat{E}$ in (1.9) as a function of three variables $\{N, \ell_1, \tau\}$.

B. Damped Sinusoid Parameters

In addition to selecting polynomial parameters, representing a response as damped sinusoids and polynomials as in (1.5) also requires the determination of parameters defining the M damped sinusoids. Their selection is critical to the success of the extrapolation and, in practice, must be accomplished using only $\mathbf{x}_{\mathrm{ET}}$ and $\mathbf{X}_{\mathrm{LF}}$. In this work, the necessary damped sinusoid parameters are determined using the matrix pencil method (MPM) [9]. Other techniques, such as Prony's method [10], could have potentially been used; however, MPM was chosen for its computational efficiency and numerical stability [9].

With MPM a time-domain function $y(t)$ is represented as K complex exponentials as

$$y(t) \approx \sum_{k=0}^{K-1} (A_k + jB_k) \exp\left\{(-\alpha_k + j\omega_k)t\right\}. \tag{1.10}$$

In (1.10), A_k and B_k signify the real and imaginary parts of the complex amplitude of the kth term whereas α_k and ω_k denote the damping factor and angular frequency, respectively. The MPM algorithm processes an early-time portion of $y(t)$, sampled at discrete intervals, to determine A_k, B_k, α_k, ω_k, and K. The details of the algorithm can be found in [9]. The representation of (1.5) includes damped sinusoids, but the terms of (1.10) are complex exponentials. The sum of two complex conjugate terms of (1.10) yields a single damped sinusoid. In this work, complex conjugate pairs in (1.10) are determined using MPM and

combined to specify the desired M damped sinusoids. These terms can be expressed as

$$g_m^{MPM}(t) = 2e^{-\alpha_m t}\left\{A_m \text{cos}\omega_m t - B_m \text{sin}\omega_m t\right\} \tag{1.11}$$

and

$$G_m^{MPM} = 2\left\{\frac{A_m\alpha_m - B_m\omega_m + jA_m\omega}{(\omega_m)^2 + (\alpha_m + j\omega)^2}\right\} \tag{1.12}$$

where (1.12) is obtained by taking the Fourier transform of (1.11). In (1.11) and (1.12), A_m, B_m, α_m, and ω_m correspond to the same quantities as in (1.10), however, each is now associated with the mth damped sinusoid, rather than the kth complex exponential.

Because (1.11) does not in general have the property $g_m^{MPM}(t) = 0$ for $t \leq 0$, the term is multiplied by a ramping envelop $\left(1 - e^{-\beta_m t}\right)$ to enforce the condition. The constant β_m is selected such that the mth term ramps up to 99% of its peak value after five periods, or at $t = (10\pi)/\omega_m$. This modification allows the polynomials to more accurately represent the response after removing each damped sinusoid as in (1.6).

With the ramping envelop included (1.11) and (1.12) become

$$g_m^{MPM}(t) = 2\left(1 - e^{-\beta_m t}\right)e^{-\alpha_m t}\left\{A_m \text{cos}\omega_m t - B_m \text{sin}\omega_m t\right\} \tag{1.13}$$

and

$$G_m^{MPM} = 2\left\{\frac{A_m\alpha_m - B_m\omega_m + jA_m\omega}{(\omega_m)^2 + (\alpha_m + j\omega)^2} + \frac{A_m(\alpha_m + \beta_m) - B_m\omega_m + jA_m\omega}{(\omega_m)^2 + (\alpha_m + \beta_m + j\omega)^2}\right\} \tag{1.14}$$

where (1.14) is obtained by taking the Fourier transform of (1.13). Terms with the form of (1.13) and (1.14) are used in (1.5) to represent resonances and define the mth damped sinusoid in time and frequency denoted $g_m(t)$ and $G_m(f)$.

While excellent results have been obtained using MPM, its accurate application requires the selection of a *time window* which defines the subset of numerical time samples processed [20]. Three parameters specify this time window: the beginning time sample p_1, the ending time sample p_2, and the decimation factor d. Some decimation is generally required because Δt is selected based on the spatial discretization of the time-domain CEM model and is often not the optimal for MPM. While some guidelines have been presented, e.g. [20, 21], no exact criteria exists for optimal selection of $\{p_1, p_2, d\}$. Therefore, in this work these parameters are selected using a GA.

When applying MPM alone to extrapolate a time-domain response, it is unclear how to optimize these parameters using only early-time data. For the procedure in this work, however, $\hat{E}$ in (1.9) provides a metric which can be minimized to reliably select the necessary parameters. As discussed, $\hat{E}$ is computed using only early-time and low-frequency data. Because these data sets contain mutually complementary information, $\hat{E}$ is a good indication of the true agreement between directly-computed and extrapolated responses for all time and frequency points of interest. Consequently, when extrapolating using both polynomials and damped sinusoids as in (1.5), a GA is used to minimize $\hat{E}$ in (1.9) as a function of six variables $\{p_1, p_2, d, N, l_1, t_0\}$.

1.5 Numerical Results

For three resonant antennas the driving-point current response due to a wideband voltage source, denoted as $x(t)$ and $X(f)$, is extrapolated using only early-time and low-frequency data. Early-time values of $x(t)$ are determined with the TLM method which discretizes a volume around the structure as cubical nodes interconnected by virtual transmission lines [14]. Low-frequency values of $X(f)$ are determined with MoM to solve the EFIE for the surface current on the structure using a triangular patch discretization. The current is represented with Rao-Wilton-Glission edge elements [22, 23]. Not only does the discretization of the time and frequency numerical models differ, but whereas MoM calculates current values directly, TLM uses adjacent fields to determine current values at a point. Thus, it is expected that these directly-computed responses will differ slightly due to *modeling* or *discretization differences*. It is shown in this work that despite these differences the response can still be accurately extrapolated; and therefore, the choice of CEM methods utilized is not unique. Alternative formulations such as the finite-difference time-domain method (FDTD) [24] or the finite element method (FEM) [25] could have also been utilized to determine $\mathbf{x}_{\mathrm{ET}}$ and $\mathbf{X}_{\mathrm{LF}}$, respectively.

A differentiated Gaussian pulse (DGP) is used to provide wideband voltage excitation. The pulse is expressed in the time domain as

$$v_0(t) = -\frac{(t-t_d)}{\sqrt{2\pi\sigma}}\exp\left\{-\frac{(t-t_d)}{2\sigma^2}\right\} \tag{1.15}$$

and in the frequency domain as

$$V_0(\omega) = j\omega\sigma^2\exp\{-j\omega t_d\}\exp\left\{-\left(\omega^2\sigma^2\right)/2\right\}. \tag{1.16}$$

In (1.15) and (1.16), σ specifies the time width and t_d represents the time delay. The maximum value of the magnitude of $V_0(\omega)$ occurs at $\omega = 1/\sigma$ and the pulse has no DC content. The parameter σ is selected to be $\sigma = 3.5/(2\pi f_{max})$ where f_{max} specifies the highest frequency of interest. At $f = f_{max}$ the magnitude of $V_0(\omega)$ is approximately 1% of its maximum value. The time delay t_d is selected to be $t_d = 10\sigma$ to ensure $v_0 \approx 0$ for $t \leq 0$. A DGP with $f_{max} = 4\,\text{GHz}$ is illustrated in Fig. 1.1.

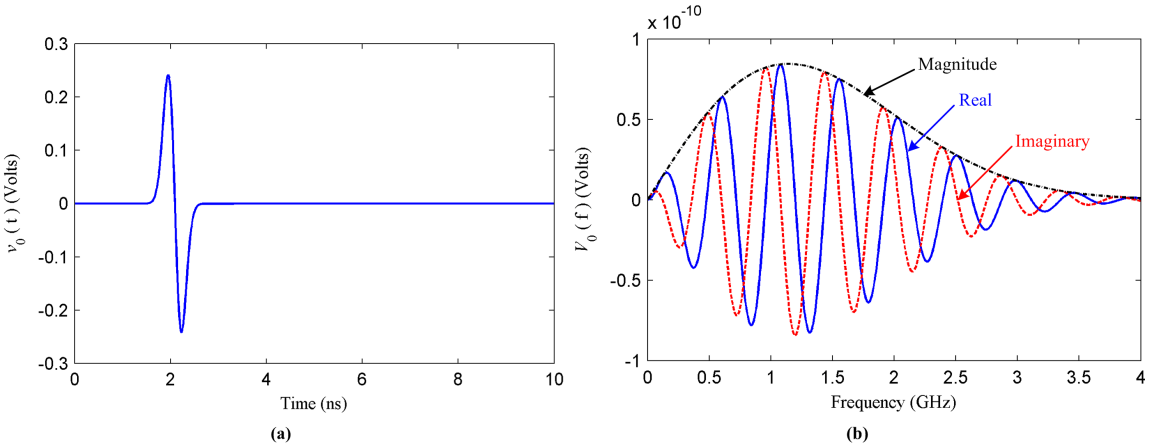

Figure 1.1**:** The differentiated Gaussian pulse voltage source in (1.15) and (1.16) for $f_{max} = 4$ is illustrated in the (a) time domain and (b) frequency domain.

To quantify the extrapolation accuracy, the extrapolated and directly-computed responses are compared in late-time and high-frequency ranges by defining E_{ext} as

$$E_{ext} = \frac{1}{2}\left\{ \frac{\|\mathbf{x}_{\text{LT}} - \hat{\mathbf{x}}_{\text{LT}}\|}{\|\mathbf{x}_{\text{LT}}\|} + \frac{\left\|\mathbf{X}_{\text{HF}} - \hat{\mathbf{X}}_{\text{HF}}\right\|}{\|\mathbf{X}_{\text{HF}}\|} \right\} \tag{1.17}$$

where the leading $1/2$ is included to average time and frequency differences. The expression in (1.17) is a good measure of the success of the extrapolation. Computing E_{ext} in (1.17) requires $\mathbf{x}_{\text{LT}}$ and $\mathbf{X}_{\text{HF}}$ and therefore cannot be directly minimized in practice; however, it provides a valuable measure to compare against the performance of the extrapolation when minimizing $\hat{E}$ in (1.9).

Accuracy is assessed here by comparing extrapolated responses to those directly-computed with CEM methods. If accurate responses cannot be directly computed, due to numerical dispersion or limited computing resources for example, measurements could also provide a benchmark.

Example 1: Monopole with Four Parasitic Elements

The first antenna considered is a monopole with height $h_1 = 16\,\text{cm}$ centered on a finite ground plane and loaded by four parasitic elements (Fig. 1.2). Each element is cylindrical with radius $a = 1\,\text{mm}$ and is assumed to be perfectly conducting. The ground plane is $26\,\text{cm} \times 26\,\text{cm}$ and assumed to be vanishingly thin and perfectly conducting. Compared with a single-element monopole, the parasitic elements significantly increase the strength of the resonance at $440\,\text{MHz}$ where the height of the center element is approximately $\lambda/4$.

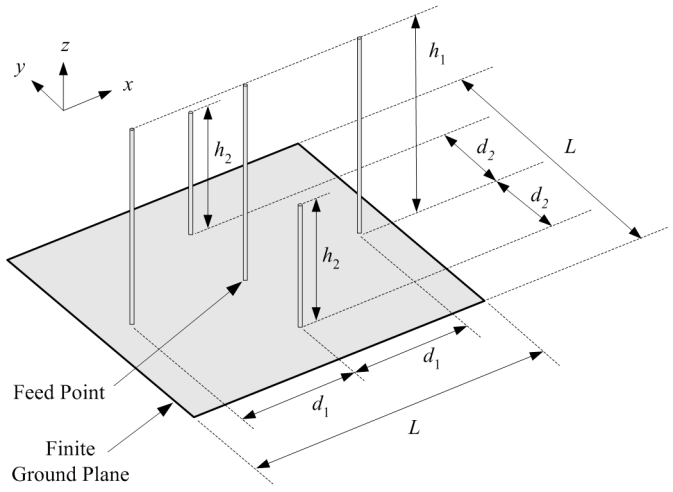

Figure 1.2**:** Geometry of monopole with parasitic elements: $h_1 = 16\,\text{cm}$, $h_2 = 10\,\text{cm}$, $d_1 = 10\,\text{cm}$, $d_2 = 7\,\text{cm}$, $L = 26\,\text{cm}$.

The antenna is driven by a DGP voltage source $(f_{\text{max}} = 3.5\,\text{GHz})$ applied at the base of the center element. The time-domain current at the feed point was determined at $\Delta t = 10\,\text{ps}$ up to $T = 248\,\text{ns}$ where it decays to zero. The frequency-domain current at the feed

point is determined at $\Delta f = 2\,\text{MHz}$ up to $W = 3.5\,\text{GHz}$. The frequency response is multiplied by the spectrum of the DGP to obtain the response due to the excitation pulse. The parameters T and W denote, respectively, the span of time and band of frequency of interest.

Fig. 1.3 compares the directly-computed current responses with an extrapolated representation using polynomials and damped sinusoids as in (1.5). Excellent agreement is seen. The vertical dashed lines indicate the partition between early-time/late-time and low-frequency/high-frequency. The range to the left of the dashed line is assumed to be known whereas range to the right is unknown and must be extrapolated. Only 12% of time span ($0.12T$) and 25% of the frequency band ($0.25W$) were required for direct computation to accurately extrapolate the complete response. All necessary parameters were selected by minimizing $\hat{E}$ in (1.9) with a GA. The response is efficiently represented with only $N = 49$ polynomials and $M = 14$ damped sinusoids. Conversely, representing the response as polynomials does not result in an accurate extrapolation (Fig. 1.4).

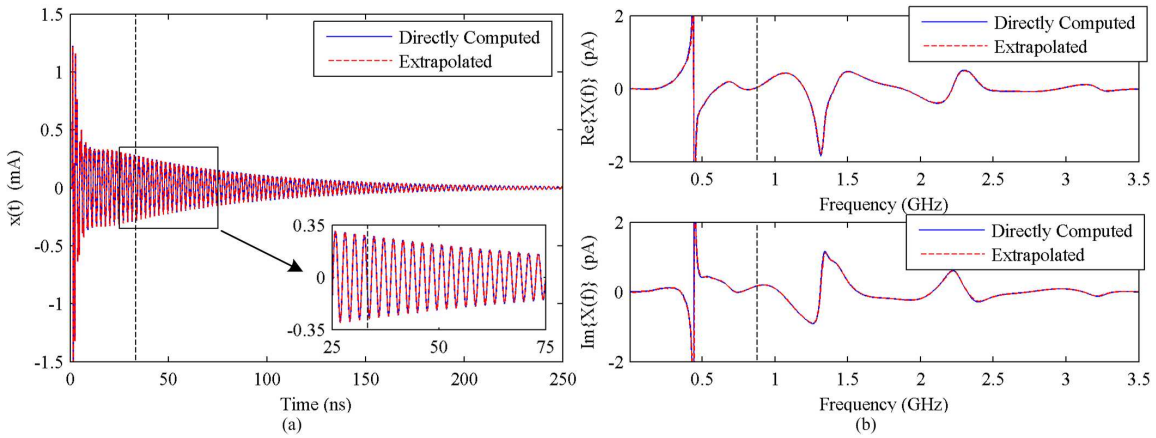

Figure 1.3**:** Extrapolation of driving-point current of the monopole with parasitic elements using damped sinusoids and polynomials: (a) time domain, inset: $25\,\text{ns} - 75\,\text{ns}$, (b) frequency domain. The directly-computed and extrapolated responses are nearly indistinguishable, indicating an accurate extrapolation.

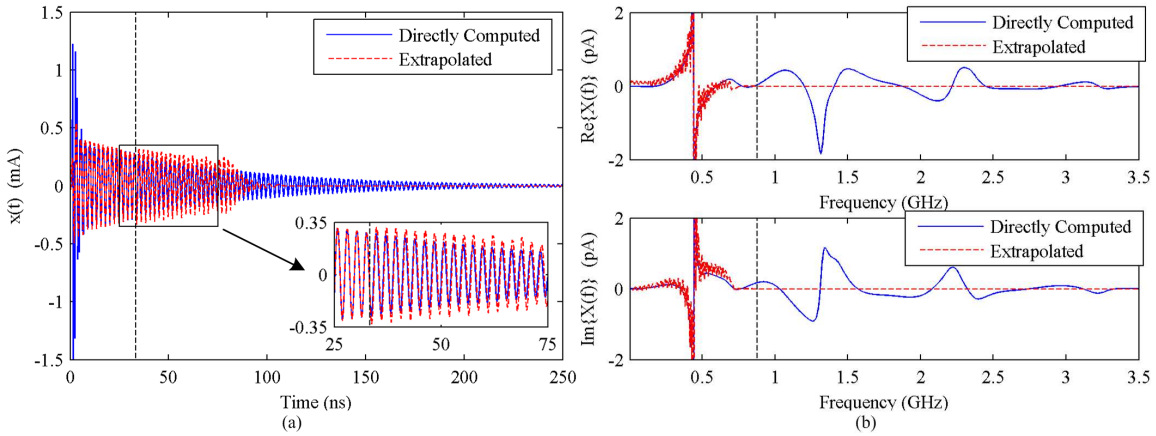

Figure 1.4**:** Extrapolation of driving-point current of the monopole with parasitic elements using only polynomials: (a) time domain, inset: 25 ns - 75 ns, (b) frequency domain. The directly-computed and extrapolated responses do not agree, thus the extrapolation is inaccurate.

Fig. 1.5(a) shows E_{ext} in (1.17) plotted versus the percentage of the time span T used for directly-computed time data. The directly-computed frequency data range is held constant at 25% of the band W. The solid lines denote extrapolation using both polynomials and damped sinusoids (DS/Poly.) whereas the dashed lines denote using only polynomials (Poly.). It is seen that accuracy is significantly improved with the addition of damped sinusoids. The two curves with circle markers were determined using a GA to minimize E_{ext} which effectively defines a lower bound on the performance of the procedure for the given amount of directly-computed data. The curves with square markers were obtained by minimizing $\hat{E}$ which requires only $\mathbf{x}_{\mathrm{ET}}$ and $\mathbf{X}_{\mathrm{LF}}$ to compute and thus can be used in practical applications. As seen in Fig. 1.5(a), when using both damped sinusoids and polynomials, nearly the same accuracy is achieved by minimizing either $\hat{E}$ or E_{ext} with $0.10T$ and $0.25W$.

Fig. 1.5(b) illustrates the value of $\hat{E}$ obtained using polynomials and damped sinusoids plotted versus the amount of directly-computed data as in Fig. 1.5(a). When enough early-time/low-frequency data is available for an accurate extrapolation (in this case, around

$0.10T$ and $0.25W$), the value of $\hat{E}$ is seen to converge.

For practical applications checking the convergence of $\hat{E}$ provides an automated procedure to decide when enough directly-computed data is available. A lower-bound criterion is not effective because the lowest value of $\hat{E}$ obtainable depends on the modeling/discretization differences of the directly-computed responses which will not be known in practice. In this work, a stopping criterion was employed by assuming $\hat{E}$ to be sufficiently converged when its value varied by less than 1% over three successive applications of the extrapolation. For this example, the extrapolation procedure was applied at increments of 277 time steps ($0.10T$) with direct computation of 25% of the frequency band ($0.25W$). The convergence criterion was met by directly computing $0.12T$ and $0.25W$ of the response.

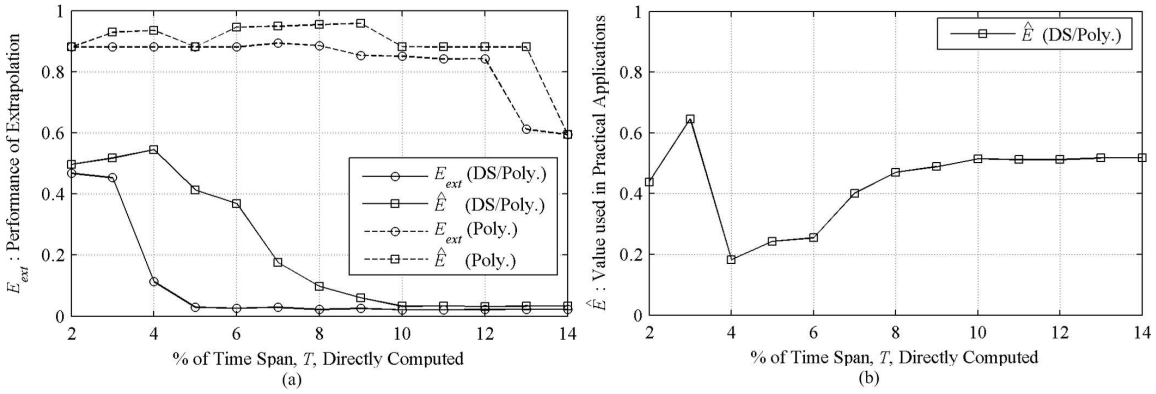

Figure 1.5**:** Extrapolation of driving-point current of the monopole with parasitic elements plotted versus the percentage of time span T directly computed (25% of frequency band W directly computed): (a) E_{ext} obtained by minimizing quantities in the legend, (b) $\hat{E}$ for DS/Poly.

Example 2: E-Shaped Patch Antenna

Next, the driving-point current of a dual-band E-shaped patch antenna (Fig. 1.6) is extrapolated. The antenna is designed to radiate effectively at $1.9\,\text{GHz}$ and $2.4\,\text{GHz}$ for wireless communications applications [26]. A DGP voltage source with $f_{\text{max}} = 4\,\text{GHz}$ is applied at the base of the probe feed. The time response is evaluated at $\Delta t = 10\,\text{ps}$ up to $T = 211\,\text{ns}$ where it effectively decays to zero. The frequency response is determined at $\Delta f = 2\,\text{MHz}$ up to $W = 4.0\,\text{GHz}$.

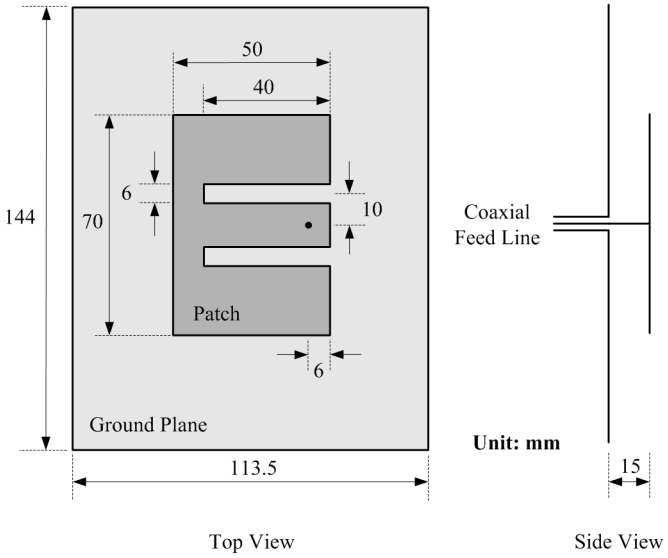

Figure 1.6**:** Geometry of the E-shaped patch antenna.

The current is accurately extrapolated using $0.06T$ and $0.25W$ directly-computed data with $N = 32$ polynomials and $M = 9$ damped sinusoids (Fig. 1.7). As seen in Fig. 1.8, the response is not accurately represented by polynomials alone. All necessary parameters are again selected by minimizing $\hat{E}$ with a GA. By extrapolating the response no direct frequency-domain computations are required at the designed frequencies of operation $1.9\,\text{GHz}$ and $2.4\,\text{GHz}$. Instead, this information is determined from early-time data. Thus, the computational burden of modeling the structure at high frequencies with a frequency-

domain CEM method is reduced, however, care must be take to sufficiently discretize the time-domain CEM model for accuracy at $f = f_{\max}$.

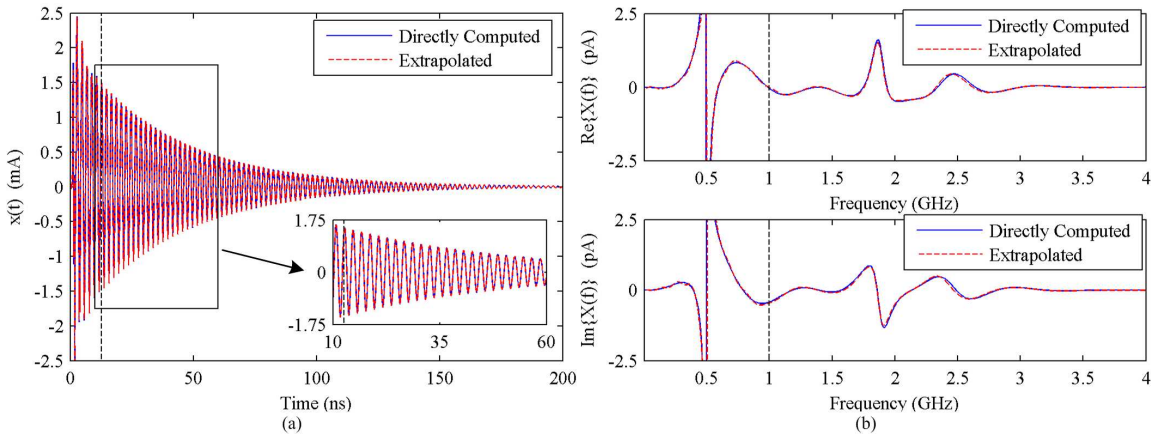

Figure 1.7**:** Extrapolation of driving-point current of the E-shaped patch antenna using damped sinusoids and polynomials: (a) time domain, inset: $10\,\text{ns} - 60\,\text{ns}$, (b) frequency domain. The directly-computed and extrapolated responses are nearly indistinguishable, indicating an accurate extrapolation.

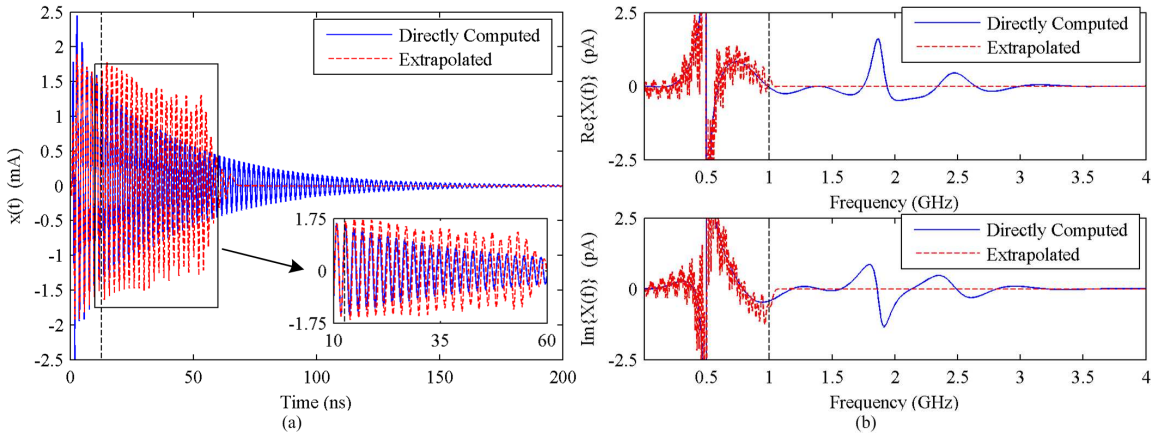

Figure 1.8**:** Extrapolation of driving-point current of the E-shaped patch antenna using only polynomials: (a) time domain, inset: $10\,\text{ns} - 60\,\text{ns}$, (b) frequency domain. The directly-computed and extrapolated responses do not agree, thus the extrapolation is inaccurate.

As in Fig. 1.5(a), E_{ext} is plotted in Fig. 1.9(a) versus the percentage of T directly computed. The percentage of W directly computed is held constant at 25%. The representation with damped sinusoids is again seen to more accurately represent the response than

with polynomials alone. The curves representing minimizing $\hat{E}$ and E_{ext} with a GA converge for cases with at least 4% of T directly computed and 25% of W directly computed; therefore, optimal parameters can be determined using only early-time/low-frequency data by minimizing $\hat{E}$. The convergence of $\hat{E}$ was again used as a stopping criterion to determine when enough data had been directly-computed. For this example the extrapolation procedure was applied at increments of 211 time steps ($0.01T$) with direct computation of $0.25W$. The convergence criterion was met by directly computing $0.06T$ and $0.25W$ of the response.

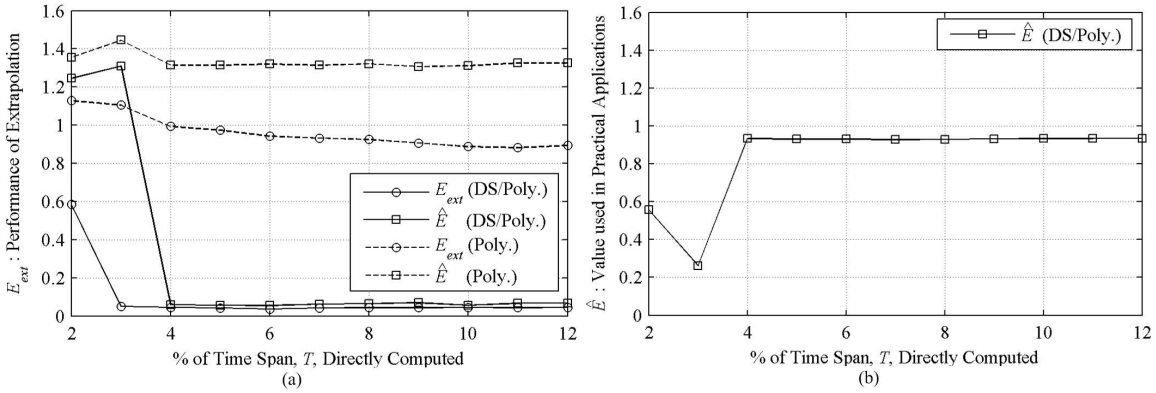

Figure 1.9**:** Extrapolation of driving-point current of the E-shaped patch antenna plotted versus the percentage of time span T directly computed (25% of frequency band W directly computed): (a) E_{ext} obtained by minimizing quantities in the legend, (b) $\hat{E}$ for DS/Poly.

Example 3: Cavity-Backed Slot Antenna with Monopole

The final example is a rectangular cavity-backed slot antenna with an interior monopole described in [27] and illustrated in Fig. 1.10. The antenna is designed to operate at $2.45\,\text{GHz}$ where the length of the slot is approximately $\lambda/2$ and the monopole height is approximately $\lambda/4$. The walls of the cavity and surface of the cylindrical monopole are assumed to be perfectly conducting. The antenna is driven by a DGP voltage source ($f_{\text{max}} = 15\,\text{GHz}$) applied at the base of the monopole and the desired response is the driving-point current. The excitation excites numerous cavity modes and many monopole and slot resonances which are observed in the response. To extrapolate the response each resonance must be accurately represented.

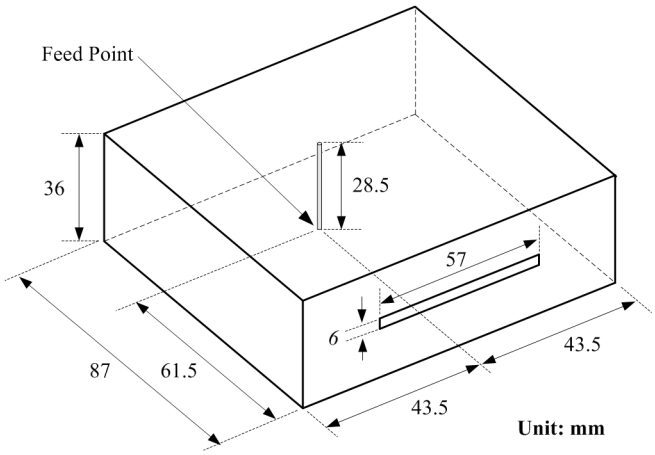

Figure 1.10**:** Geometry of cavity-backed slot antenna with monopole.

A TLM model is again used to determine numerical values of the time-domain current. This response provides early-time data and is used to check the accuracy of the extrapolation. The frequency-domain data is obtained by taking the discrete Fourier transform (DFT) of computed time-domain response. This response provides the low-frequency data used in the extrapolation. While this approach would not be used in practice, it allows the technique to be tested and removes any effects of discretization differences between the

time and frequency responses. The same approach is utilized in [19].

The time response is sampled at $\Delta t = 30\,\text{ps}$ intervals up to $T = 1.45\,\mu\text{s}$, and the frequency response is sampled at $\Delta f = 1\,\text{MHz}$ up to $W = 15\,\text{GHz}$. Using damped sinusoids and polynomials, the response was accurately extrapolated from $0.025T$ and $0.25W$ of the response (Fig. 1.11). The response was represented using $N = 484$ polynomials and $M = 44$ damped sinusoids. Conversely, the response is not well represented using only polynomials (Fig. 1.12).

Determining the wideband current response of the cavity-backed slot antenna using traditional CEM techniques is very computationally demanding. The transient current response decays very slowly because energy must bounce around inside the cavity and eventually propagate through slot to be radiated outside the structure. Consequently, tens of thousands of time steps are required to determine the complete time response. Characterizing the response of the structure in the frequency domain requires hundreds or thousands of separate frequency evaluations to sufficiently cover the wide frequency range of interest. Therefore, extrapolation offers substantial computational benefits. With the procedure in the work an accurate representation of the complete response is obtained without time-stepping the transient response to a steady state or evaluating the response over the entire frequency range of interest.

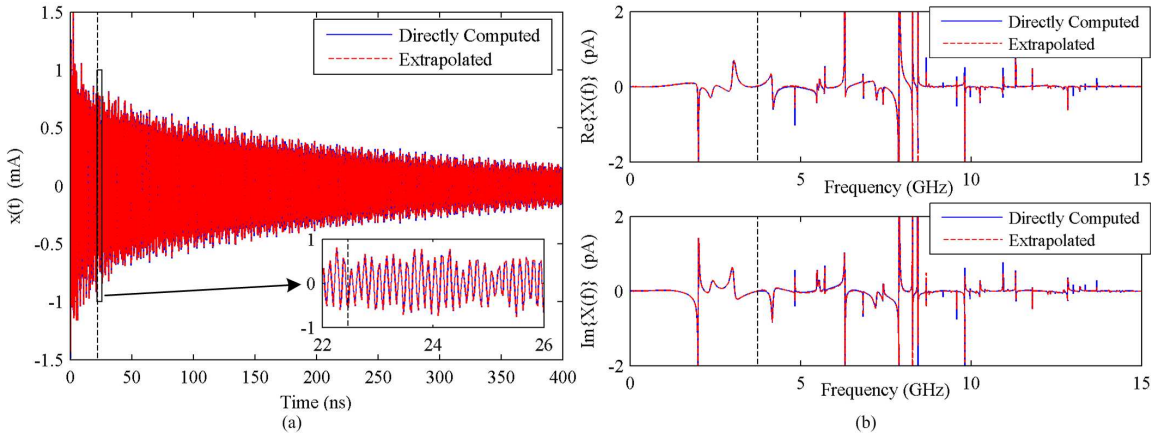

Figure 1.11**:** Extrapolation of driving-point current of cavity-backed slot antenna with monopole using damped sinusoids and polynomials: (a) time domain, inset: $22\,\text{ns} - 26\,\text{ns}$, (b) frequency domain. The directly-computed and extrapolated responses are nearly indistinguishable, indicating an accurate extrapolation.

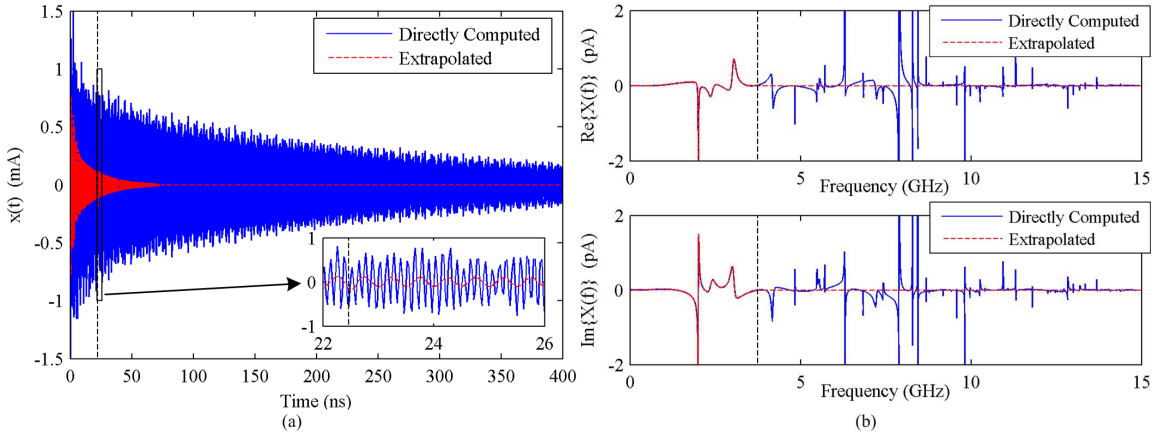

Figure 1.12**:** Extrapolation of driving-point current of the cavity-backed slot antenna with monopole using only polynomials: (a) time domain, inset: $22\,\text{ns} - 26\,\text{ns}$, (b) frequency domain. The directly-computed and extrapolated responses do not agree, thus the extrapolation is inaccurate.

1.6 Conclusions

A procedure is presented to simultaneously extrapolate a time- and frequency-domain response due to wideband excitation of a resonant antenna using only early-time and low-frequency data. The response is accurately and efficiently represented by a sum of N orthogonal polynomials and M damped sinusoids. The use of damped sinusoids allows multiple resonances to be effectively modeled. The resulting representation of the response can be evaluated at time and/or frequency points of interest and provides a single set of parameters which characterizes the response in both time and frequency.

A method of incorporating damped sinusoids with orthogonal polynomials to represent a response and determining parameters defining each function is presented. A GA-based procedure is described to select all parameters needed to reliably extrapolate a response. This procedure can also be used to determine when enough data is available to yield an accurate extrapolation.

The extrapolation technique is shown to operate successfully even when applied to time and frequency responses computed from CEM methods using fundamentally different discretizations of the modeled structure, such as TLM and MoM. Thus, the procedure can be applied independently of the CEM methods used. Therefore, the choice may be made based on the user's familiarity with a particular method, selected based on the method best suited for the given application, or based on what is available to the user.

1.7 Appendix A: Associate Hermite Functions

Properties of associate Hermite (AH) functions, which are used in the extrapolation procedure to represent a response, are now presented. Hermite polynomials are discussed first, and then this background is used to describe some important characteristics of AH functions. The representation of a signal as a sum of weighted AH functions, as discussed in [28], is then presented to provide a mathematical basis for the extrapolation procedure in this work.

A. Hermite Polynomials

Let $H_n(x)$ for $n = 0, 1, \ldots, \infty$ denote the set of Hermite polynomials [29, Ch. 22]. The polynomials are orthogonal on the interval $(-\infty, \infty)$, with respect to the weight function $w(x) = e^{-x^2}$, and satisfy the relationship:

$$\int_{-\infty}^{\infty} H_n(x) H_k(x) e^{-x^2} dt = \begin{cases} n! 2^n \sqrt{\pi} & \text{if } n = k \\ 0 & \text{if } n \neq k \end{cases}. \tag{1.18}$$

The nth-order Hermite polynomial can be directly determined from

$$H_n(x) = (-1)^n e^{x^2} \frac{d}{dx^n} e^{-x^2} \tag{1.19}$$

or found recursively from the relationship

$$H_n(x) = 2x H_{n-1}(x) - 2(n-1) H_{n-2}(x). \tag{1.20}$$

The first five Hermite polynomials can be written as

$$\begin{cases} H_0(x) = 1 \\ H_1(x) = 2x \\ H_2(x) = 4x^2 - 2 \\ H_3(x) = 8x^3 - 12x \\ H_4(x) = 16x^4 - 44x^2 + 12 \end{cases} . \tag{1.21}$$

Hermite polynomials are centered about zero and satisfy the symmetry condition

$$H_n(-x) = (-1)^n H_n(x) . \tag{1.22}$$

From (1.22) it is clear that Hermite polynomials of even order are even functions whereas Hermite polynomials of odd order are odd functions. Fig. 1.13 illustrates $H_1(x)$, $H_2(x)$, $H_3(x)$, $H_4(x)$.

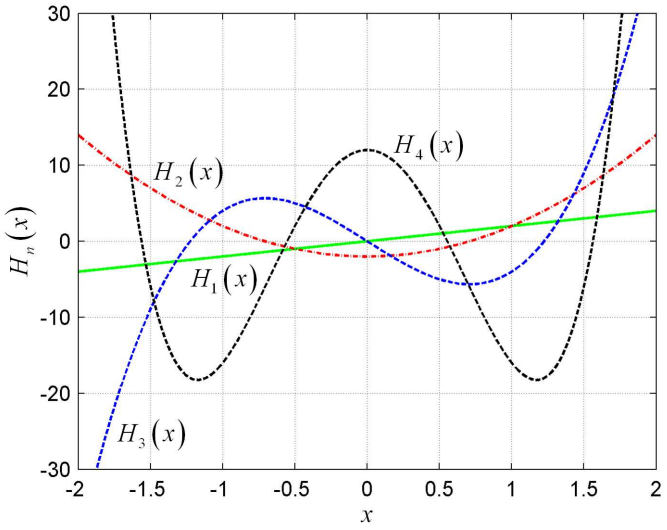

Figure 1.13**:** Hermite polynomials $H_n(x)$ for orders one to four.

B. Associate Hermite (AH) Functions

A set of associate Hermite (AH) functions (also referred to as Gaussian weighted Hermite polynomials) can be defined in terms of Hermite polynomials as

$$\phi_n\left(t/\ell_1\right) = \frac{1}{\sqrt{2^n n! \sqrt{\pi}\ell_1}} H_n\left(t/\ell_1\right) e^{\frac{-(t/\ell_1)^2}{2}} \tag{1.23}$$

where n is the function order, ℓ_1 is a time scaling factor, and $H_n\left(x\right)$ is the nth order Hermite polynomial [28]. An AH function is obtained by scaling the argument of a Hermite polynomial by a time scaling factor ℓ_1 and multiplying by a Gaussian function whose standard deviation is ℓ_1. The set of AH functions in (1.23) are orthonormal for $n = 0, 1, \ldots, \infty$ and satisfy the relationship

$$\int_{-\infty}^{\infty} \phi_n\left(t/\ell_1\right) \phi_k\left(t/\ell_1\right) dt \;=\; \begin{cases} 1 & \text{if } n = k \\ 0 & \text{if } n \neq k \end{cases}. \tag{1.24}$$

The first five AH functions with $\ell_1 = 1$ are shown in Fig. 1.14.

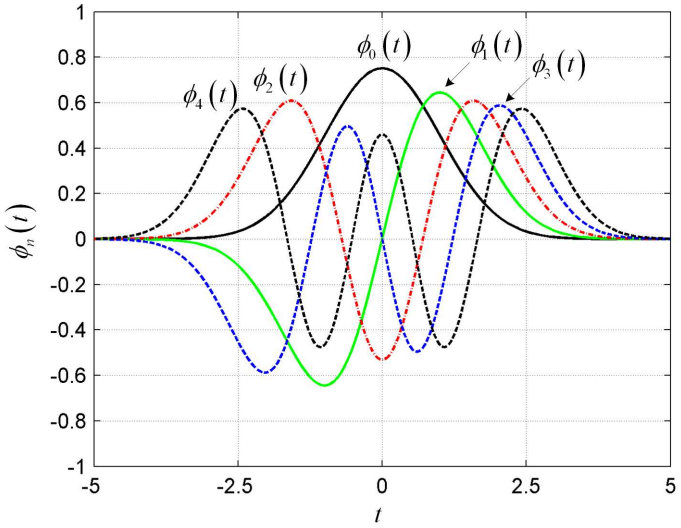

Figure 1.14**:** Associate Hermite (AH) functions $\phi_n\left(t/\ell_1\right)$ of order zero to four with time scaling factor $\ell_1 = 1$.

Each AH function is symmetric about $t = 0$ and the *width*, also referred to as the *support*, of the AH functions is compact and increases with order n. Fig. 1.15 illustrates the increased width of higher-order AH functions. For instance, note that the support of $\phi_0(t)$ is approximately $t \in (-2, 2)$, whereas the higher-order function $\phi_{30}(t)$ has support over a wider range of approximately $t \in (-9, 9)$.

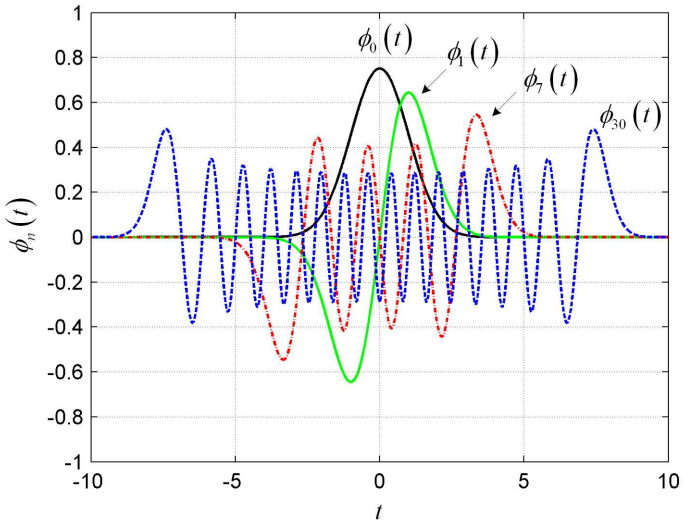

Figure 1.15**:** Associate Hermite (AH) functions $\phi_n(t/\ell_1)$ of orders $n = 0, 1, 7, 30$ with time scaling factor $\ell_1 = 1$. Illustrates the support of the AH functions increase with order n.

In Fig. 1.16, the first-order AH function $\phi_1(t/\ell_1)$ is plotted for several values of ℓ_1 to illustrate the effect of the time scaling parameter. The width of $\phi_1(t/\ell_1)$ is increased for $\ell_1 > 1$ and is decreased for $\ell_1 < 1$. This allows the support of AH functions to be expanded or contracted.

A time center t_0 can be specified to shift the center of the AH functions from $t = 0$ to $t = \tau$. Fig. 1.17 illustrates the effect of the time center t_0 on the first order AH function $\phi_1((t-\tau)/\ell_1)$.

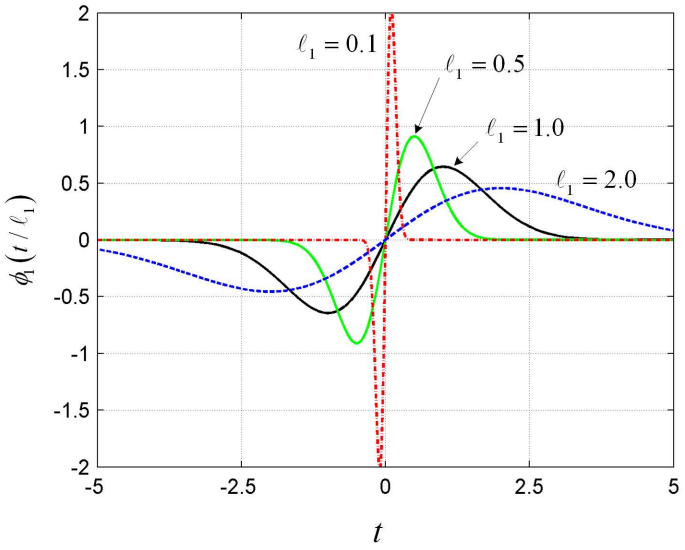

Figure 1.16**:** First order AH function $\phi_1\left(t/\ell_1\right)$ plotted for several values of the time scaling factor ℓ_1.

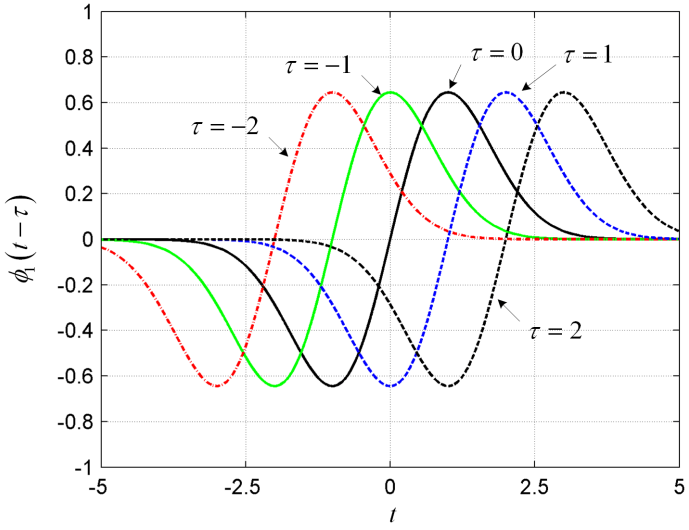

Figure 1.17**:** First-order AH function $\phi_1\left(\left(t-\tau\right)/\ell_1\right)$ plotted for several values of the time center τ with time scaling factor $\ell_1 = 1$.

C. Representation of a Signal as a Sum of AH Functions

A procedure to represent a signal as a weighted sum of AH functions is presented in [28]. It provides the basis of the polynomial extrapolation in [2]-[4] and the procedure in this chapter. The representation of the response is that same in both [28] and [2]-[4]; however, in [28] it is assumed that the complete signal is known, whereas the procedure of [2]-[4] relies on only early-time and low-frequency data to obtain a representation of the complete response.

The set of AH functions scaled by ℓ_1 constitute an orthonormal basis [28]. Consequently, a time-domain response $x(t)$ can be represented by a weighted sum of AH functions as

$$x(t) = \sum_{n=0}^{\infty} a_n \phi_n (t/\ell_1). \tag{1.25}$$

The series of (1.25) converges if $x(t)$ has finite energy, i.e.,

$$\int_{-\infty}^{\infty} (x(t))^2 \, dt < \infty. \tag{1.26}$$

If the complete response is known, the coefficients a_n in (1.25) can be determined based on the orthogonality of the AH functions as

$$\begin{aligned} a_n &= \int_{-\infty}^{\infty} x(t) \, \phi_n (t/\ell_1) \, dt \\ &= \frac{1}{\sqrt{2^n n! \sqrt{\pi} \ell_1}} \int_{-\infty}^{\infty} x(t) \, H_n \left(\frac{t}{\ell_1} \right) e^{\frac{-(t/\ell_1)^2}{2}} dt. \end{aligned} \tag{1.27}$$

The coefficients a_n determined with (1.27) minimize the normalized mean square error (NMSE) E_N between an N term representation from (1.25), denoted $\hat{x}(t)$, and the original response $x(t)$:

$$E_N = \frac{\int_{-\infty}^{\infty} \left[\hat{x}(t) - x(t)\right]^2 dt}{\int_{-\infty}^{\infty} x^2(t)\, dt}. \tag{1.28}$$

The value of E_N in (1.28) is monotonically decreasing from one to zero for increasing N [28].

A frequency-domain response can also be represented as a weighted sum of AH functions [28]. Consider the Fourier transform of the time-domain AH functions:

$$\begin{aligned} \mathcal{F}\left\{\phi_n(t/\ell_1)\right\} &= (-j)^n \sqrt{\frac{2\ell_1\sqrt{\pi}}{2^n n!}} H_n(2\pi\ell_1 f)\, e^{\frac{-(2\pi\ell_1 f)^2}{2}} \\ &= (-j)^n \frac{1}{\sqrt{2^n n!\sqrt{\pi}\ell_2}} H_n(f/\ell_2)\, e^{\frac{-(f/\ell_2)^2}{2}} \\ &= \Phi_n(f/\ell_2). \end{aligned} \tag{1.29}$$

In (1.29), the frequency scaling factor ℓ_2 is related to the time scaling factor ℓ_1 by $\ell_2 = 1/(2\pi\ell_1)$. The Fourier transform of a time-domain AH function of order n scaled by ℓ_1 is a frequency-domain AH function of order n scaled by ℓ_2. Thus, there is an isomorphism between AH functions and their transforms.

The set of AH functions scaled by ℓ_2 for $n = 0, 1, \ldots, \infty$ form an orthonormal basis in the frequency domain and satisfy the relationship

$$\int_{-\infty}^{\infty} \Phi_n(f/\ell_2)\, \Phi_k(f/\ell_2)\, df = \begin{cases} 1 & \text{if } n = k \\ 0 & \text{if } n \neq k \end{cases}. \tag{1.30}$$

Therefore, a frequency-domain response $X(f)$, where $\mathcal{F}\{x(t)\} = X(f)$, can be represented by a weighted sum of AH functions scaled by ℓ_2 as

$$X(f) = \mathcal{F}\{x(t)\} = \sum_{n=0}^{\infty} a_n \Phi_n(f/\ell_2). \tag{1.31}$$

The series of (1.31) converges if $X(f)$ has finite energy,

$$\int_{-\infty}^{\infty} (X(f))^2 \, df < \infty. \tag{1.32}$$

Similar to (1.27), if the complete frequency-domain response is known the coefficients a_n in (1.31) can be determined based on orthogonality as

$$\begin{aligned} a_n &= \int_{-\infty}^{\infty} X(f) \, \Phi_n(f/\ell_2) \, df \\ &= (-j)^n \frac{1}{\sqrt{2^n n! \sqrt{\pi} \ell_2}} \int_{-\infty}^{\infty} X(f) \, H_n\left(\frac{f}{\ell_2}\right) e^{\frac{-(f/\ell_2)^2}{2}} df. \end{aligned} \tag{1.33}$$

If $x(t)$ and $X(f)$ are related by the Fourier transform, then the responses can be represented by (1.25) and (1.31), respectively, as a sum of AH functions weighted by a set of N coefficients a_n. The set of coefficients is the same for both time and frequency representations. The frequency-domain response is simply a scaled version of the time response, with the time and frequency scaling factors related by $\ell_2 = 1/(2\pi\ell_1)$. The number of terms N, time scaling factor ℓ_1, and time center τ provide flexibility to shape the AH functions and fit $x(t)$ and $X(f)$. Because the scaling factors are inversely related, an increase in the width of a time-domain AH function results in a decrease of the width of the corresponding AH function in the frequency domain and vice versa. Also, if the time-domain AH functions are centered around $t = \tau$, then the time shift results in a phase shift in the frequency

domain of $e^{j2\pi\tau f}$, i.e., $\mathcal{F}\left\{\phi\left(\left(t-\tau\right)/\ell_1\right)\right\} = e^{j2\pi\tau f}\Phi\left(f/\ell_2\right)$.

Eqs. (1.27) and (1.33) can only be applied to solve for the coefficients a_n if the *complete* response known, which is not the case for extrapolation. Thus, to extrapolate the response a_n must be determined by a different means. A least-squares solution for a_n can be found by equating the AH representation with discrete values of the response at early-time and low-frequency points, and solving the resulting system of equations (Eq. (1.3)). The success of this approach, however, is found to depend on the proper selection of N, ℓ_1, and τ. Relatively few choices of these parameters lead to a system which can be solved for coefficients which yield an accurate representation of the response. The complete responses are unknown, and thus cannot be used to aid in the parameter selection. In this chapter, an automated means to select the parameters needed to reliably extrapolate a response is provided by the GA-based selection procedure.

CHAPTER 2
TIME AND FREQUENCY BIAS IN EXTRAPOLATING WIDEBAND RESPONSES OF RESONANT STRUCTURES

Abstract

An improved procedure to extrapolate a wideband electromagnetic response of a resonant structure using only early-time and low-frequency numerical data is presented. The response is represented as a sum of weighted polynomials and pole terms. In Chapter 1, a procedure is described to estimate poles from early-time data, and in this chapter it is demonstrated that poles can also be estimated from low-frequency data and used to accurately extrapolate a response. A time or frequency bias is observed when estimating poles from either early-time or low-frequency data, respectively. A new method is also presented to combine poles estimated from early-time and low-frequency data and reduce the amount of directly-computed data needed to extrapolate a response. An optimization routine is described which automates the selection of all parameters needed to reliably apply the extrapolation procedure. Several numerical examples are presented to illustrate the proposed technique and study the performance of the three pole-estimation methods presented.

2.1 Introduction

For many applications it is necessary to numerically compute an electromagnetic (EM) response of a structure due to a wideband excitation source. Such a response can be most any EM quantity of interest located at a point in space and defined as a function of both time and frequency. Examples include the electric field at a point in space or the current at a point on the surface of an antenna. The driving-point current can be used to compute return loss

and characterize antenna performance. The electric field outside a metallic enclosure due to interior excitation can be used to quantify radiated electromagnetic interference (EMI) levels, or interior fields due to exterior excitation can be used to study penetration into an enclosure.

Typically, a response is determined with a computational electromagnetic (CEM) method by numerically solving Maxwell's equations in either the time or frequency domain; however, determining a response of a strongly resonant structure can be challenging in either domain. A response is obtained in the time domain by exciting the structure and time stepping until transient energy dies out or is radiated away. For a resonant structure the response can be exceedingly long and require many time steps and long computation times. Numerical dispersion can also limit the accuracy of late-time computations. Conversely, frequency-domain formulations require a separate evaluation for each frequency and fine sampling near strong resonances. Also, high-frequency evaluations require increased spatial discretization of the model to maintain accuracy.

In Chapter 1 and in [1, 5, 6, 7, 8] procedures are described to extrapolate, in both time and frequency, a response of a resonant structure by processing only early-time and low-frequency numerical data. The response is approximated by a representation that can be evaluated for time and/or frequency points of interest. Extrapolating the response can require significantly less time than directly computing it with CEM methods. A complete response can be extrapolated from early-time and low-frequency data because the two data sets contain mutually complementary information which together contain the behavior of the complete response [2]. Early-time data contain high-frequency information whereas low-frequency data contain late-time information. In [2], a response is represented as a sum of orthogonal polynomials; however, extrapolating the responses typical of resonant structures with only polynomials, which provide compact support, proves numerically dif-

ficult and inefficient in practice. With the procedure in Chapter 1, damped sinusoids are used with orthogonal polynomials to accurately extrapolate responses from resonant structures. Damped sinusoids efficiently represent the effects of strong resonances whereas polynomials characterize the remaining behavior.

A procedure is presented which improves upon the approach in Chapter 1 and reduces the amount of directly-computed data needed to extrapolate a response. Pole terms are used in place of damped sinusoids, and both polynomial coefficients and pole residues are determined as the solution to a single matrix equation, as opposed to the two-step process in Chapter 1. With the procedure of Chapter 1, one estimates the poles from early-time data by applying the matrix pencil method (MPM) [9]. A wider approach is considered here and poles are also estimated from low-frequency data by applying the vector fitting method (VFM) [30]. VFM is an efficient method for determining a rational representation of a frequency domain response. VFM has been used in a variety of applications including electromagnetic compatibility (EMC) shielding analysis [31], microwave signal integrity [32], and Green's function representation [33].

With the procedure presented in this chapter, responses of resonant structures are accurately extrapolated by estimating poles from *either* early-time or low-frequency CEM data. A time or frequency bias is observed by examining extrapolation accuracy as a function of the amount of CEM data. A new method is also presented to combine poles estimated from early-time and low-frequency data and reduce the amount of directly-computed data needed to extrapolate a response. The effect of differences in CEM data sets due to discretization or modeling is also examined. A genetic algorithm (GA) [34] is used to automate the selection of all parameters required for extrapolation.

This chapter is organized as follows. Section 2.2 discusses the extrapolation technique and determination of coefficients and residues. Section 2.3 presents methods for estimating

poles from early-time data, low-frequency data, and a combined approach. The GA-based selection of the set of extrapolation parameters is discussed in Section 2.4. Section 2.5 presents several numerical examples and conclusions are presented.

2.2 Formulation of Extrapolation Technique

Let $x(t)$ and $X(f)$ denote the time and frequency representations, respectively, of an EM response due to a wideband source. The early-time and low-frequency portions of $x(t)$ and $X(f)$ contain high-frequency and late-time information, respectively, and can be processed to determine an accurate representation of the complete response as a sum of weighted analytic functions. To develop an appropriate form for the representation, the response is viewed as a superposition of two functions with specific characteristics:

$$\begin{aligned} x(t) &= x^T(t) + x^R(t) \\ X(f) &= X^T(f) + X^R(f). \end{aligned} \tag{2.1}$$

In (2.1), $x^R(t)$ and $X^R(f)$ contain the effects of strong *resonances* in the response. Oscillation and exponential decay characterize $x^R(t)$, whereas peaks around resonant frequencies dominate the behavior of $X^R(f)$. To efficiently characterize this behavior, these functions are represented by *pole terms*. Conversely, $x^T(t)$ and $X^T(f)$ correspond to the remaining *transient* behavior which decays rapidly in time and is relatively smooth in frequency. Orthogonal polynomials provide compact support and are therefore used to represent $x^T(t)$ and $X^T(f)$. With this approach $x(t)$ and $X(f)$ are approximated by $\hat{x}(t)$ and $\hat{X}(f)$ which are sums of N orthogonal polynomials and M pole terms:

$$x(t) \approx \hat{x}(t) = \sum_{n=0}^{N-1} a_n \phi_n(t/\ell_1) + \sum_{m=0}^{M-1} R_m g_m(t)$$
$$X(f) \approx \hat{X}(f) = \sum_{n=0}^{N-1} a_n \Phi_n(f/\ell_2) + \sum_{m=0}^{M-1} R_m G_m(f) \tag{2.2}$$

where N and M are integers. In (2.2), $\phi_n\left(t/\ell_1\right)$ and $\Phi_n\left(f/\ell_2\right)$ represent nth-order polynomials which are related by the Fourier transform and scaled by factors ℓ_1 and ℓ_2, where $\ell_1 = 1/\left(2\pi\ell_2\right)$ [1]. The polynomials are weighted by N real-valued coefficients $\mathbf{a}_N = \left[a_0, a_1, \ldots, a_{N-1}\right]^{\mathrm{T}}$ where $[\cdot]^{\mathrm{T}}$ denotes the transpose. In (2.2), $g_m\left(t\right)$ and $G_m\left(f\right)$ represent the mth complex exponential and pole term expressed in time and frequency as

$$g_m(t) = \exp\left(s_m t\right) \tag{2.3}$$
$$G_m(f) = 1/(j2\pi f - s_m). \tag{2.4}$$

The poles terms are weighted by M complex-valued residues $\mathbf{R}_M = \left[R_0, R_1, \ldots, R_{M-1}\right]^{\mathrm{T}}$, and the vector $\mathbf{s}_M = \left[s_0, s_1, \ldots, s_{M-1}\right]^{\mathrm{T}}$ contains the values of the M poles. The mth pole is defined as $s_m = \alpha_m + j2\pi f_m$ where α_m and f_m are the damping factor and resonant frequency, respectively. To yield a real-valued time response poles occur in conjugate pairs or are real.

Different types of pole terms can be incorporated in the representation of (2.2). For example, in Chapter 1 complex conjugate pairs of pole terms are combined into a single damped sinusoid, and in this chapter the pole terms have the form of (2.3) and (2.4). The terms of (2.3) and (2.4) effectively represent the resonant portion of a response and their form allows one to determine polynomial coefficients and pole residues as the solution to a single matrix equation.

For a particular response, $\hat{x}(t)$ and $\hat{X}(f)$ in (2.2) are completely specified by the values of $\mathbf{a}_N$, $\mathbf{R}_M$, and $\mathbf{s}_M$. Thus, to extrapolate a response one must determine these values from only early-time and low-frequency data, such that $\hat{x}(t)$ and $\hat{X}(f)$ accurately represent $x(t)$ and $X(f)$.

Data are determined at discrete points with CEM methods. Let the discrete time-response $\mathbf{x}$ contain P data points uniformly sampled at Δt and be partitioned into early-time and late-time data, $\mathbf{x}_{\mathrm{ET}}$ and $\mathbf{x}_{\mathrm{LT}}$, where $\mathbf{x}_{\mathrm{ET}}$ contains the first p time samples of $\mathbf{x}$. Let the discrete frequency-response $\mathbf{X}$ contain Q data points uniformly sampled at Δf and be partitioned into low-frequency and high-frequency data, $\mathbf{X}_{\mathrm{LF}}$ and $\mathbf{X}_{\mathrm{HF}}$, where $\mathbf{X}_{\mathrm{LF}}$ contains the first q frequency samples of $\mathbf{X}$. These data vectors can be written as

$$\begin{aligned}
\mathbf{x}_{\mathrm{ET}} &= \left[x\left(t_1\right), x\left(t_2\right), \ldots, x\left(t_p\right)\right]^{\mathrm{T}} \\
\mathbf{x}_{\mathrm{LT}} &= \left[x\left(t_{p+1}\right), x\left(t_{p+2}\right), \ldots, x\left(t_P\right)\right]^{\mathrm{T}} \\
\mathbf{X}_{\mathrm{LF}} &= \left[X\left(f_1\right), X\left(f_2\right), \ldots, X\left(f_q\right)\right]^{\mathrm{T}} \\
\mathbf{X}_{\mathrm{HF}} &= \left[X\left(f_{q+1}\right), X\left(f_{q+2}\right), \ldots, X\left(f_Q\right)\right]^{\mathrm{T}}
\end{aligned} \tag{2.5}$$

where $t_k = (k-1)\,\Delta t$ and $f_k = (k-1)\,\Delta f$. Using (2.5), $\mathbf{x}$ and $\mathbf{X}$ can be expressed as $\mathbf{x} = [\mathbf{x}_{\mathrm{ET}}; \mathbf{x}_{\mathrm{LT}}]$ and $\mathbf{X} = [\mathbf{X}_{\mathrm{LF}}; \mathbf{X}_{\mathrm{HF}}]$. A time-domain and a frequency-domain CEM method are used to compute $\mathbf{x}_{\mathrm{ET}}$ and $\mathbf{X}_{\mathrm{LF}}$, respectively.

Although a function cannot be band-limited in both time and frequency, it is assumed here the responses considered are effectively time-limited to T and frequency-limited to W, such that $x(t) \approx 0$ for $t > T$ and $X(f) \approx 0$ for $f > W$. The directly-computed portions of the time and frequency response are denoted as T' and W', respectively.

For a fixed Δt and Δf, the values of T' and W' specify the early-time and low-frequency data points determined with CEM methods and hence available to use to extrap-

olate the response. Larger values of T' and W' indicate that more data have been computed. One can deduce the following relationships from (2.5): $T = (P-1)\Delta t$, $W = (Q-1)\Delta f$, $T' = (p-1)\Delta t$, and $W' = (q-1)\Delta f$.

Determining $\mathbf{a}_N$, $\mathbf{R}_M$, and $\mathbf{s}_M$ from $\mathbf{x}_{\mathrm{ET}}$ and $\mathbf{X}_{\mathrm{LF}}$ is presented here as a two-step process. First the set of poles $\mathbf{s}_M$ is obtained, then the coefficients and residues $\mathbf{a}_N$ and $\mathbf{R}_M$ are computed together. In general, there are three approaches to determining $\mathbf{s}_M$: using $\mathbf{x}_{\mathrm{ET}}$, using $\mathbf{X}_{\mathrm{LF}}$, or using both $\mathbf{x}_{\mathrm{ET}}$ and $\mathbf{X}_{\mathrm{LF}}$. In Chapter 1 poles are only estimated from early-time data. This chapter demonstrates that each of the three approaches can be used to accurately extrapolate a response; however, the amounts of early-time and low-frequency data required by each approach may differ.

After determining the poles, $\mathbf{a}_N$ and $\mathbf{R}_M$ can be computed as a least-squares solution to a system of $(p+2q)$ linear equations:

$$\begin{bmatrix} \boldsymbol{\phi}_N[t_{\mathrm{ET}}] & \mathbf{g}_M[t_{\mathrm{ET}}] \\ \mathrm{Re}\left\{\boldsymbol{\Phi}_N[f_{\mathrm{LF}}]\right. & \left.\mathbf{G}_M[f_{\mathrm{LF}}]\right\} \\ \mathrm{Im}\left\{\boldsymbol{\Phi}_N[f_{\mathrm{LF}}]\right. & \left.\mathbf{G}_M[f_{\mathrm{LF}}]\right\} \end{bmatrix} \begin{bmatrix} \mathbf{a}_N \\ \mathbf{R}_M \end{bmatrix} = \begin{bmatrix} \mathbf{x}_{\mathrm{ET}} \\ \mathrm{Re}\left\{\mathbf{X}_{\mathrm{LF}}\right\} \\ \mathrm{Im}\left\{\mathbf{X}_{\mathrm{LF}}\right\} \end{bmatrix} \tag{2.6}$$

where $\mathrm{Re}\{\cdot\}$ and $\mathrm{Im}\{\cdot\}$ denote the real and imaginary parts of the complex argument, respectively. In (2.6), $\boldsymbol{\phi}_N[t_{\mathrm{ET}}]$ and $\mathbf{g}_M[t_{\mathrm{ET}}]$ denote matrices obtained by evaluating the time-domain form of each of the N polynomials and M pole terms, respectively, at the p early-time points. Similarly, $\boldsymbol{\Phi}_N[f_{\mathrm{LF}}]$ and $\mathbf{G}_M[f_{\mathrm{LF}}]$ denote matrices obtained by evaluating the frequency-domain form of each of the N polynomials and M pole terms, respectively, at the q low-frequency points. These matrices can be explicitly written as

$$
\begin{aligned}
\boldsymbol{\phi}_N[t_{\mathrm{ET}}] &= \begin{bmatrix} \phi_0\left(t_0/\ell_1\right) & \cdots & \phi_{N-1}\left(t_0/\ell_1\right) \\ \vdots & \ddots & \vdots \\ \phi_0\left(t_{p-1}/\ell_1\right) & \cdots & \phi_{N-1}\left(t_{p-1}/\ell_1\right) \end{bmatrix} \\
\mathbf{g}_M[t_{\mathrm{ET}}] &= \begin{bmatrix} g_0\left(t_0\right) & \cdots & g_{M-1}\left(t_0\right) \\ \vdots & \ddots & \vdots \\ g_0\left(t_{p-1}\right) & \cdots & g_{M-1}\left(t_{p-1}\right) \end{bmatrix} \\
\boldsymbol{\Phi}_N[f_{\mathrm{LF}}] &= \begin{bmatrix} \Phi_0\left(f_0/\ell_2\right) & \cdots & \Phi_{N-1}\left(f_0/\ell_2\right) \\ \vdots & \ddots & \vdots \\ \Phi_0\left(f_{q-1}/\ell_2\right) & \cdots & \Phi_{N-1}\left(f_{q-1}/\ell_2\right) \end{bmatrix} \\
\mathbf{G}_M[f_{\mathrm{LF}}] &= \begin{bmatrix} G_0\left(f_0\right) & \cdots & G_{M-1}\left(f_0\right) \\ \vdots & \ddots & \vdots \\ G_0\left(f_{p-1}\right) & \cdots & \phi_{M-1}\left(f_{q-1}\right) \end{bmatrix}. \qquad (2.7)
\end{aligned}
$$

The rectangular matrix on the left-hand side of (2.6) has dimensions $(p+2q)\times(N+M)$ and the column vector contains the $(N+M)$ unknowns. In practical cases, $(p+2q) > (N+M)$, and (2.6) is an overdetermined system for which a least-squares solution can be determined using one of several techniques [16].

Both $\mathbf{a}_N$ and $\mathbf{R}_M$ are determined by solving the system of equations in (2.6). This differs from the approach in Chapter 1 which can be summarized as follows. First, MPM is used to determine $\mathbf{s}_M$ and then $\mathbf{R}_M$ is computed as a least-squares solution using $\mathbf{x}_{\mathrm{ET}}$. Next, damped sinusoids are formed with $\mathbf{s}_M$ and $\mathbf{R}_M$, and then each term is subtracted from $\mathbf{x}_{\mathrm{ET}}$ and $\mathbf{X}_{\mathrm{LF}}$ to isolate the portion of the response represented by polynomials alone. Lastly, $\mathbf{a}_N$ is determined from a system of equations similar to (2.6), but with $\mathbf{a}_N$ as the only unknown (Eq. 1.3). Ramping envelops are added to each damped sinusoid to enforce causality and improve the accuracy of the procedure [1].

The procedure described here is preferable to the approach in Chapter 1 for several reasons. The single systems of equation in (2.6) can be solved to determine both $\mathbf{a}_N$ and $\mathbf{R}_M$, and there is no longer a need for a ramping envelop. The least-squares solution for $\mathbf{R}_M$ in (2.6) now involves both $\mathbf{x}_{\mathrm{ET}}$ and $\mathbf{X}_{\mathrm{LF}}$, whereas only early-time data is used in Chapter 1. The approach in this chapter also outperforms the previous procedure in terms of the accuracy and convergence of the extrapolation. Additionally, the determination of $\mathbf{s}_M$ is completely independent of the computation of $\mathbf{a}_N$ and $\mathbf{R}_M$. This provides flexibility in the choice of pole-estimation method because regardless of how $\mathbf{s}_M$ is obtained, the computation of $\mathbf{a}_N$ and $\mathbf{R}_M$ remains unchanged.

2.3 Methods for Estimating Poles of the Response

To extrapolate a response, $\mathbf{s}_M$ must contain estimates of the poles of the structure which correspond to the dominant resonances. The set of poles $\mathbf{s}_M$ is determined by processing the directly-computed CEM data $\mathbf{x}_{\mathrm{ET}}$ and $\mathbf{X}_{\mathrm{LF}}$. Three procedures to estimate the poles are now presented.

A. Estimating Poles with Early-time Data

The first approach considered is to determine $\mathbf{s}_M$ from early-time data $\mathbf{x}_{\mathrm{ET}}$. Several techniques have been presented in the literature to approximate a time response as a sum of complex exponentials of the form in (2.3). In this work, total least-squares MPM is employed [9]. Other techniques such as Prony's method [10] could also be used; however, MPM was selected for its computational efficiency and numerical stability. Residues for each pole term can also be computed with MPM, however, in the procedure described here the residues are computed with (2.6) and MPM is used only to estimate poles.

A subset of the numerical time samples in $\mathbf{x}_{\mathrm{ET}}$, denoted $\mathbf{y}$, is specified and processed with the MPM algorithm. The subset is defined by the beginning and ending time samples p_1 and p_2, and a decimation factor d. The vector $\mathbf{y}$ contains $p' = \lfloor (p_2 - p_1)/d \rfloor$ time samples uniformly spaced at $d\Delta t$ intervals, where $\lfloor \cdot \rfloor$ is the greatest integer less than or equal to the argument. The accuracy of the pole estimation depends on the selection of p_1, p_2, and d, which in this work is automated using a GA. Decimation is required because Δt is typically selected based on stability requirements of the time-domain CEM method and is not optimal for MPM [9].

To determine $\mathbf{s}_M$ with MPM a matrix $\boldsymbol{Y}$, whose eigenvalues are related to the desired poles, is formed with the time samples in $\mathbf{x}_{\mathrm{ET}}$. The number of poles M is selected from the singular value decomposition (SVD) of $\boldsymbol{Y}$, computed as $\boldsymbol{Y} = \boldsymbol{U}\boldsymbol{\Sigma}\boldsymbol{V}$ where $\boldsymbol{\Sigma}$ contains the singular values of $\boldsymbol{Y}$ on its diagonal. The value of M is taken to be the number of singular values in the range $\sigma_{\text{max}} > \sigma > 10^{-3}\sigma_{\text{max}}$ [9]. After the value of M is selected, an $(M \times M)$ matrix V' is constructed from the M rows of V associated with the M largest singular values. The set of poles $\mathbf{s}_M$ is then determined directly from the M eigenvalues of V', denoted λ_m, which are related to $\mathbf{s}_M$ as $\lambda_m = \exp\{s_m d\Delta t\}$ for $m = 0, \ldots, M-1$.

B. Estimating Poles with Low-frequency Data

The next approach considered is to determine $\mathbf{s}_M$ from low-frequency data $\mathbf{X}_{\mathrm{LF}}$. Several techniques, such as the Padé approximation [35], have been used to approximate a frequency response as rational function. In this work VFM is utilized [30]. One can use VFM to approximate a frequency response as a sum of pole terms in the form of (2.4), and it has been shown to be numerically efficient and capable of resolving a large number of resonances [30]. VFM can also be used to determine residues; however, it is only used to estimate poles in this work.

The VFM algorithm determines a set of poles by first specifying initial values for the M poles in $\mathbf{s}_M$ and then iteratively improving them by determining a least-squares solution for a system of q linear equations

$$\left(\sum_{m=1}^{M}\frac{\tilde{r}_m}{j2\pi f_k - s_m} + 1\right) X_{\mathrm{LF}}\left(f_k\right) = \sum_{m=1}^{M}\frac{r_m}{j2\pi f_k - s_m} \tag{2.8}$$

for $k=0,\ldots,q-1$. An improved set of poles is obtained by solving the eigenvalue problem $\mathbf{s}_M = eig(\mathbf{A} - \mathbf{bc}^{\mathrm{T}})$ where $\mathbf{A}$ is a diagonal matrix containing the initial set of poles, $\mathbf{b}$ is a column vector of ones, and $\mathbf{c}$ contains $\tilde{r}_m$ found by solving (2.8). The improved set of poles obtained replaces the previous set used in (2.8), and then the process is repeated. Typically, the pole locations converge after only a few iterations [30] and $\mathbf{s}_M$ accurately represents the poles of the response. The accuracy of the poles determined with VFM depends on the selection of M as well as the choice of starting and ending frequency points of the data processed, denoted q_1 and q_2. In this work these parameters are selected with an automated GA-based procedure.

While the number of poles obtained with VFM and MPM has both been denoted by M, the number of poles determined by each technique will generally not be equal. MPM and VFM both aim to estimate the poles of a response, but VFM *interpolates* over the range of frequency data processed whereas MPM *extrapolates* and can provide an approximation outside the range of data processed, i.e., for times greater than the last data point in $\mathbf{x}_{\mathrm{ET}}$. Because VFM interpolates data, $\mathbf{s}_M$ computed with VFM does not necessarily contain estimates of poles with resonant frequencies higher than the last data point in $\mathbf{X}_{\mathrm{LF}}$. Conversely, estimates of high-frequency resonances may be readily obtained from early-time data with MPM. To accurately extrapolate a response, $\mathbf{s}_M$ should contain estimates of the dominate poles of a response because highly resonant behavior is numerically difficult to represent

with polynomials as demonstrated in Chapter 1 and in [1]. Dominant resonances typically occur at low frequencies. Therefore, a response can be extrapolated by applying VFM to estimate poles from $\mathbf{X}_{\mathrm{LF}}$ if $\mathbf{s}_M$ contains accurate estimates of the dominant low-frequency resonances. The high-frequency resonances not estimated by VFM are represented by polynomials instead of pole terms.

C. Combined Early-time and Low-frequency Method

The complementary nature of early-time and low-frequency data can be exploited with an approach that combines poles estimated from both data sets. Poles with lower resonant frequencies may be more accurately estimated by processing low-frequency data, whereas poles with higher resonant frequencies may be better estimated by processing early-time data. High-frequency resonances appear earlier in time compared to lower frequency resonances which take longer to set up.

If sets of poles estimated with MPM and VFM are properly combined into a single set, a response can be extrapolated with less directly-computed data than is required if one applied either MPM or VFM alone. A procedure to combine the two pole sets is as follows. First, MPM is applied to $\mathbf{x}_{\mathrm{ET}}$ and VFM is applied to $\mathbf{X}_{\mathrm{LF}}$. The resulting sets of poles, denoted $\mathbf{s}_M^{\mathrm{MP}}$ and $\mathbf{s}_M^{\mathrm{VF}}$, are then combined into a single set $\mathbf{s}_M$ by specifying a parameter γ in the range $0 < \gamma < 1$.

For each pole in $\mathbf{s}_M^{\mathrm{MP}}$, if

$$\begin{cases} f_m^{\mathrm{MP}} > \gamma W\ ; & \text{include } \mathbf{s}_M^{\mathrm{MP}} \text{ in } \mathbf{s}_M \\ f_m^{\mathrm{MP}} < \gamma W\ ; & \text{use VFM estimate of pole} \end{cases} \tag{2.9}$$

Similarly, for each pole in $\mathbf{s}_M^{\mathrm{VF}}$, if

$$\begin{cases} f_m^{\mathrm{VF}} > \gamma W\ ; & \text{use MPM estimate of pole} \\ f_m^{\mathrm{VF}} < \gamma W\ ; & \text{include } \mathbf{s}_M^{\mathrm{VF}} \text{ in } \mathbf{s}_M \end{cases} \tag{2.10}$$

Therefore, $\mathbf{s}_M$ contains MPM estimates of high-frequency resonances and VFM estimates of low-frequency resonances as illustrated in Fig. 2.1.

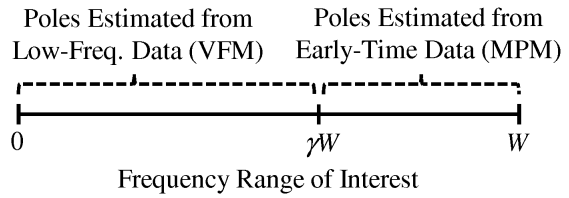

Figure 2.1**:** Illustration of combined pole-estimation method ($0 < \gamma < 1$).

Poles with resonant frequencies spanning the entire frequency range of interest are included in $\mathbf{s}_M$, so no important poles are discarded in the combining process. Additionally, MPM and VFM estimates of the same pole are not both included in $\mathbf{s}_M$, but rather either one or the other is included based on (2.9) and (2.10). Extrapolation accuracy is a function of γ, and the optimal choice of γ depends on the amount of directly-computed data as well as the resonant frequencies of the response. The selection of γ is automated with the GA-based procedure in Section 2.4.

The combined approach is essentially a generalization of the early-time and low-frequency

pole-estimation methods. If $\gamma = 0$, $\mathbf{s}_M = \mathbf{s}_M^{\mathrm{MP}}$ and only poles estimated with MPM are used. If $\gamma = 1$, $\mathbf{s}_M = \mathbf{s}_M^{\mathrm{VF}}$ and only poles estimated with VFM are used. Selecting $0 < \gamma < 1$ allows a combination of poles estimated by MPM and VFM to be included in $\mathbf{s}_M$. It will be shown in Section 2.5 that by combining poles as described, a response can be accurately extrapolated with less directly computed data than by using either early-time or low-frequency pole-estimation methods alone.

2.4 GA-Based Extrapolation Parameter Selection

The accuracy and stability of an extrapolation depends on the non-trivial selection of several parameters. These parameters must be *selected* whereas $\mathbf{a}_N$, $\mathbf{R}_M$, and $\mathbf{s}_M$ are *determined.* The GA-based optimization procedure described in Chapter 1 is extended here and used to select the parameters required for the three pole-estimation methods presented in Section 2.3. GA optimization is used because it is robust and requires no assumptions about the characteristics of the function optimized. The optimization procedure serves two purposes. First, it automates the parameter selection so that an arbitrary response can be reliably and accurately extrapolated. It also indicates when enough directly-computed data is available to accurately extrapolate the response, as described in Chapter 1.

Extrapolation accuracy is a function of each parameter and the optimal set of parameters is defined to minimize the difference between the computed responses and their representations in (2.2). This difference, E, can be quantified as

$$E = \frac{1}{2}\left\{ \frac{\|\mathbf{x} - \hat{\mathbf{x}}\|}{\|\mathbf{x}\|} + \frac{\left\|\mathbf{X} - \hat{\mathbf{X}}\right\|}{\|\mathbf{X}\|} \right\} \tag{2.11}$$

where $\|\cdot\|$ denotes the l^2-norm [16]. The value of E is small for an accurate extrapolation, so ideally parameters should be selected to minimize E; however, computing E requires

complete knowledge of the response which will not be known in practice.

An approximation of E using only $\mathbf{x}_{\mathrm{ET}}$ and $\mathbf{X}_{\mathrm{LF}}$, denoted as $\hat{E}$, is presented in Chapter 1 (Eq. 2.8). A response can be accurately extrapolated with an optimization routine by selecting parameters that minimize $\hat{E}$. This approach also provides an automated means to decide when enough directly-computed data are available. The response can be extrapolated with increasing amounts of data and when $\hat{E}$ converges, so has the extrapolation [1]. Thus, the partitioning of early/late-time and low/high-frequency need not be selected by the user.

Regardless of the method one uses to obtain a set of poles, the system of equations in (2.6) is solved to determine $\mathbf{a}_N$ and $\mathbf{R}_M$. Therefore, the polynomial parameters which must be selected are the same for each pole-estimation method: the number of terms N, the scaling factor ℓ_1, and the time center of the expansion τ. These parameters are described in Appendix A of Chapter 1. Associate Hermite functions are used in the representation in (2.2) and the set of parameters $\{N, \ell_1, \tau\}$ is selected by the GA to minimize $\hat{E}$.

Parameters associated with pole estimation must also be selected. When applying MPM to estimate poles from early-time data, the beginning and ending time point, p_1 and p_2, and the decimation factor d must be selected. When using VFM to estimate poles, the beginning and ending frequency point, q_1 and q_2, and number of pole terms M must be selected. For the combined method, $\hat{E}$ is minimized by the GA as a function of $\{p_1, p_2, d, q_1, q_2, M, \gamma\}$. The range of γ is defined to be 0.25 to 0.75.

A Matlab implementation of a real-valued GA is used in this work [36]. Each GA generation contains a population of 50 individuals and the optimization is terminated after 50 generations. In the examples presented here and others considered by the authors, GA optimization reliably determines parameters yielding accurate extrapolations, within reasonable computation times.

2.5 Numerical Results

Example 1: E-Shaped Patch Antenna

First, the driving-point current of a dual-band E-shaped patch antenna (Fig. 2.2) designed for wireless communications [26] is considered. The antenna has resonances at $0.5\,$GHz, $1.9\,$GHz, and $2.4\,$GHz, with the dominant resonance at $0.5\,$GHz. A differentiated Gaussian pulse (DGP) voltage source with effective spectral content up to $f_{\max} = 4\,$GHz was applied at the base of the probe feed. The resulting current at the driving point was determined using a time-domain CEM method at $\Delta t = 10\,$ps intervals until the response effectively decayed to zero at $T = 380\,$ns. The frequency response was obtained as the discrete Fourier transform (DFT) of the time response and evaluated at $\Delta f = 2\,$MHz intervals up to $W = 4\,$GHz. A frequency-domain CEM method could have been used to compute the response; however, the approach taken here removes any discretization or modeling differences between the directly-computed time and frequency responses. In Chapter 1 accurate extrapolations are obtained using data sets generated by CEM methods with different discretizations. The effect of discretization differences is examined in *Example 4*.

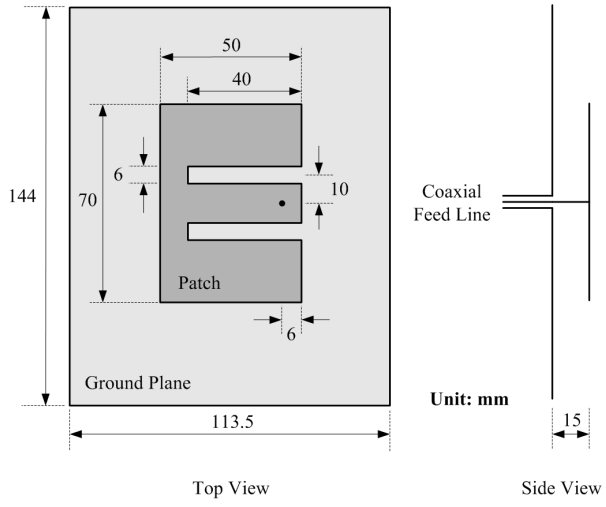

Figure 2.2**:** Geometry of E-shaped patch antenna (dimensions in mm).

The time and frequency driving-point current of the E-shaped patch antenna extrapolated using the three pole-estimation methods in Section 2.3 is illustrated in Fig. 2.3. The complete response is extrapolated by each method using only early-time and low-frequency data. All necessary parameters are selected by minimizing $\hat{E}$ with a GA as described in Section 2.4. The three extrapolated responses in Fig. 2.3 are nearly indistinguishable from the directly-computed response. Thus, a response can be extrapolated by estimating poles from *either* early-time or low-frequency data.

The results in Fig. 2.3 are obtained using different amounts of directly-computed time and frequency data, denoted T' and W'. By applying MPM to estimate poles from early-time data, the response is extrapolated from $T' = 6\,\text{ns}$ of the time-response ($p = 601$) and $W' = 0.6\,\text{GHz}$ of the frequency response ($q = 176$). By applying VFM to estimate poles from low-frequency data, the response is extrapolated from $T' = 10.5\,\text{ns}$ ($p = 1051$) and $W' = 0.35\,\text{GHz}$ ($q = 301$). With the combined method, the response is extrapolated from $T' = 6\,\text{ns}$ ($p = 601$) and $W' = 0.35\,\text{GHz}$ ($q = 176$). Therefore, the combined approach extrapolates the response with fewer directly-computed data points than by estimating poles from early-time or low-frequency data alone.

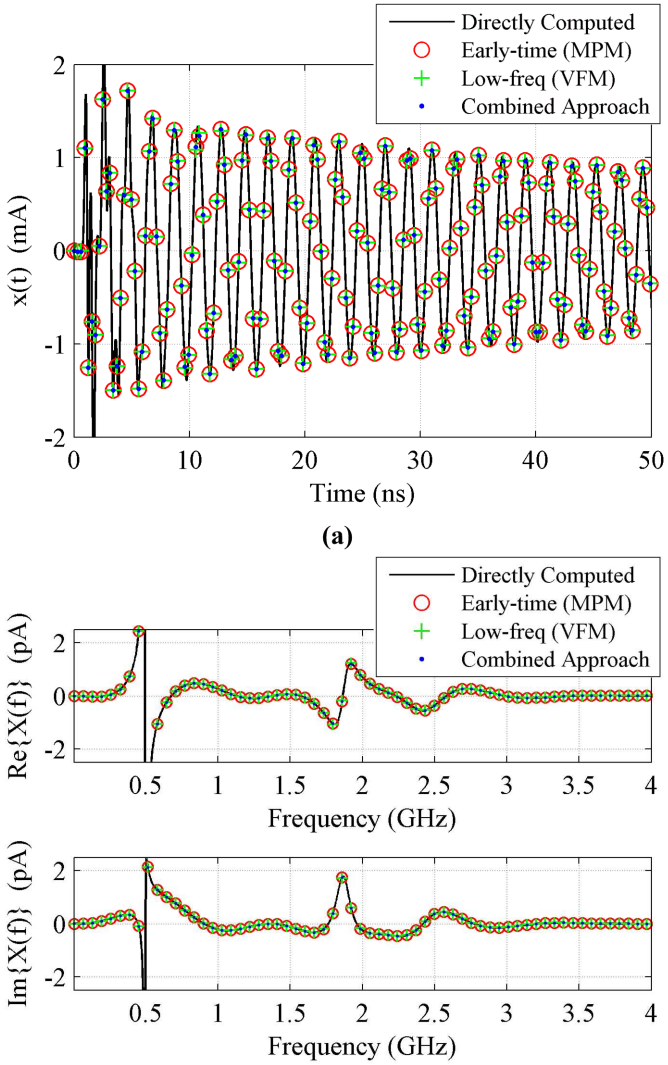

Figure 2.3**:** Extrapolation of (a) time-domain and (b) frequency-domain driving-point current of E-shaped patch antenna. Estimating poles ($\mathbf{s}_M$) from early-time data with MPM, low-frequency data with VFM, and with the combined method yields accurate and nearly indistinguishable results.

Next, extrapolation accuracy is examined as a function of T' and W', the amounts of early-time and low-frequency directly-computed data. This approach provides a more complete evaluation of each pole-estimation technique as opposed to extrapolating the response at a single value of T' and W' as in Fig. 2.3. In Fig. 2.4, the response is extrapolated at

discrete values of T' and W' for a selected range, and for each T', W' pair the extrapolation accuracy E is determined. For a given value of T' and W', the extrapolation is said to be accurate if $E < 10^{-2}$.

In Fig. 2.4(a)-(c), the value of E obtained using each pole-estimation method to extrapolate the response is plotted with T' along the horizontal axis and W' along the vertical axis. The value of T' ranges from 0.75 ns to 15 ns at 0.75 ns intervals and W' ranges from 0.05 GHz to 1 GHz at 0.05 GHz intervals. Each square in the graphs corresponds to extrapolating the response using the amount of early-time and low-frequency data specified by the values of T' and W' on the axes. The shading of each square represents the value of E obtained for the T', W' pair. Lighter shading corresponds to small values of E and indicates good agreement between extrapolated and directly-computed responses, whereas darker shading indicates poor agreement and thus an inaccurate extrapolation.

In Fig. 2.4(a), a *time bias* is seen when using early-time data to estimate poles. The vertical black band represents T', W' pairs for which the extrapolated response does not accurately represent the directly-computed response. It is seen that the response is not accurately extrapolated with $T' < 4.5$ ns. Conversely, a *frequency bias* is seen in Fig. 2.4(b) where poles are estimated from low-frequency data. In this case, the horizontal black band indicates the response is not accurately extrapolated for $W' < 0.35$ GHz. Fig. 2.4(c) shows that the combined method averages out the time and frequency bias and reduces the amount of directly-computed data required to accurately extrapolate the response. The percentage of T', W' pairs in Fig. 2.4 which yield an accurate extrapolation is 41% when estimating poles with early-time, 34% when estimating poles with low-frequency data, and 56% when using the combined method. Thus, using the combined pole-estimation method to extrapolate the response is preferred.

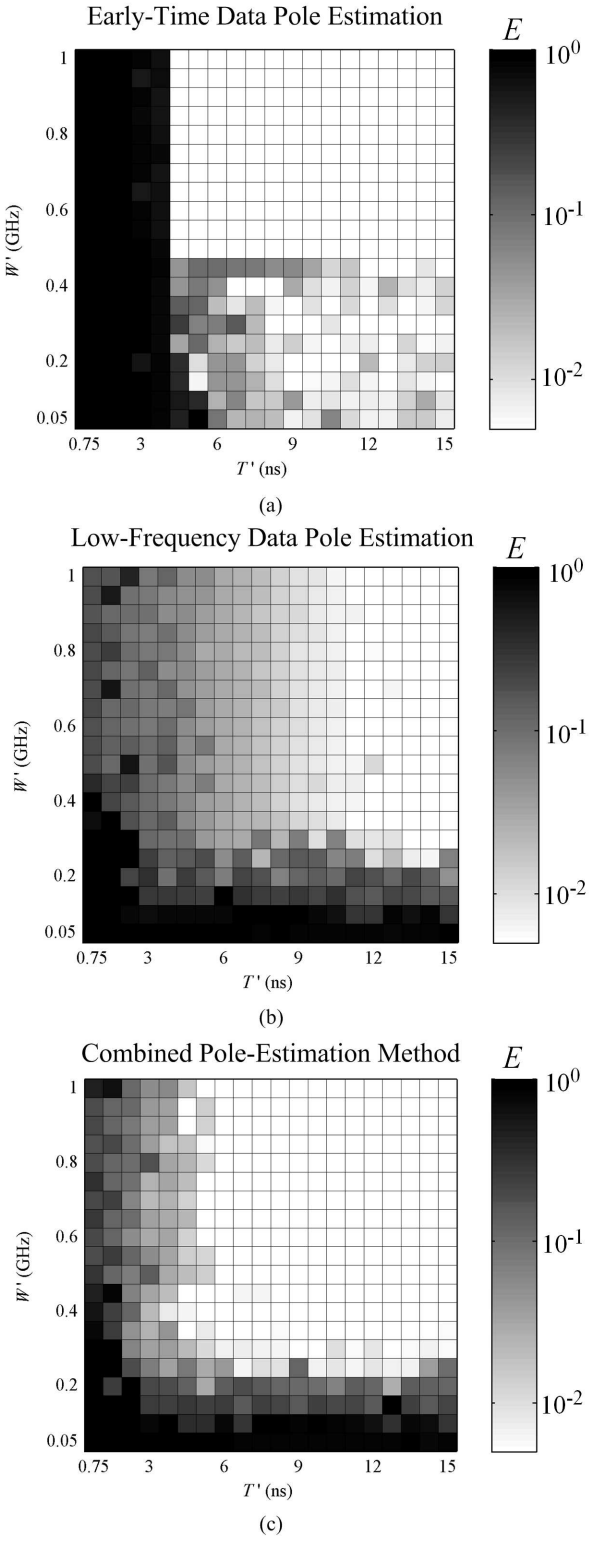

Figure 2.4**:** Accuracy of extrapolation (E) for driving-point current of E-shaped patch antenna as a function of the amount of directly-computed data, T' and W'. Poles ($\mathbf{s}_M$) estimated using (a) early-time data with MPM, (b) low-frequency data with VFM, and (c) the combined method.

Example 2: Fractal Antenna

Next, a Sierpinski gasket fractal antenna described in [23] is considered (Fig. 2.5, inset: (a)). This multi-band antenna has resonances at $0.39\,\text{GHz}$, $1.48\,\text{GHz}$, and $3.35\,\text{GHz}$. The driving-point current due to a DGP voltage source with $f_{\text{max}} = 4\,\text{GHz}$ is computed with a frequency-domain CEM method at $\Delta f = 8\,\text{MHz}$ intervals up to $W = 8\,\text{GHz}$. The time response is obtained from the inverse DFT and evaluated at $\Delta t = 5\,\text{ps}$ intervals up to $T = 20.28\,\text{ns}$. Fig. 2.5 illustrates the combined pole-estimation method used to accurately extrapolate the response with $T' = 4\,\text{ns}$ ($p = 801$) and $W' = 1.8\,\text{GHz}$ ($q = 220$). The vertical dashed lines in Fig. 2.5 indicate the partition between directly-computed data to the left and extrapolated data to the right. This structure is not as resonant as the other examples, but the same extrapolation procedure is applied successfully.

The effectiveness of the GA-based parameter selection procedure was considered by applying the optimization for 20 separate trials. An accurate extrapolation ($E < 10^{-2}$) was obtained for each trial. The average computation time required to complete the optimization was $7.6\,\text{minutes}$ using a $3.0\,\text{GHz}$ Intel CPU and $4\,\text{GB}$ of RAM running Windows XP. The CPU time required to complete the optimization is significantly less than the total time required to compute the response.

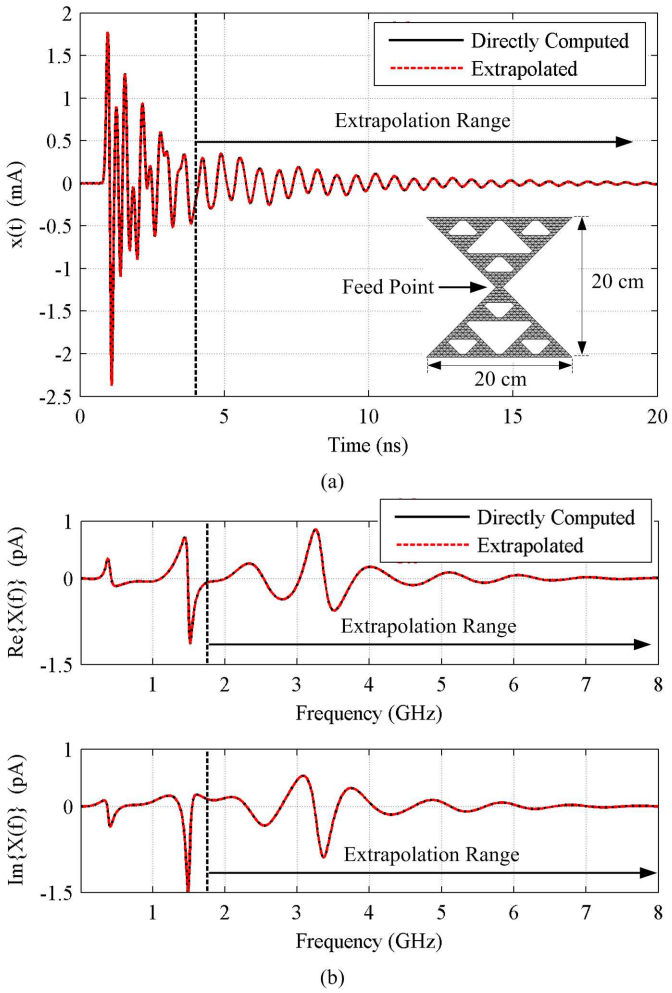

Figure 2.5**:** Extrapolation of (a) time-domain and (b) frequency-domain driving-point current of fractal antenna (inset: (a)). Poles ($\mathbf{s}_M$) estimated using the combined method. Directly-computed and extrapolated responses are nearly indistinguishable indicating an accurate extrapolation.

Example 3: Cavity with an Aperture and Slot

The next structure considered is a metallic cavity with an aperture and slot (Fig. 2.6). This structure is used as a test enclosure to evaluate radiated EMI levels ([37]). The response considered is the $\hat{z}-$ directed component of the electric field at a point centered along the $\hat{x}$ direction of the enclosure, $5\,$cm outside of the front face, and $1.6\,$cm above the bottom. This position is affected by radiation from both the slot and aperture. A DGP voltage source with $f_{\max} = 2\,$GHz is applied in the coaxial feed line. The response is determined with a time-domain CEM method at $\Delta t = 38.2\,$ps intervals up to $T = 763\,$ns. The frequency response is obtained from the DFT of the time response and evaluated at $\Delta f = 10\,$MHz intervals up to $W = 2\,$GHz.

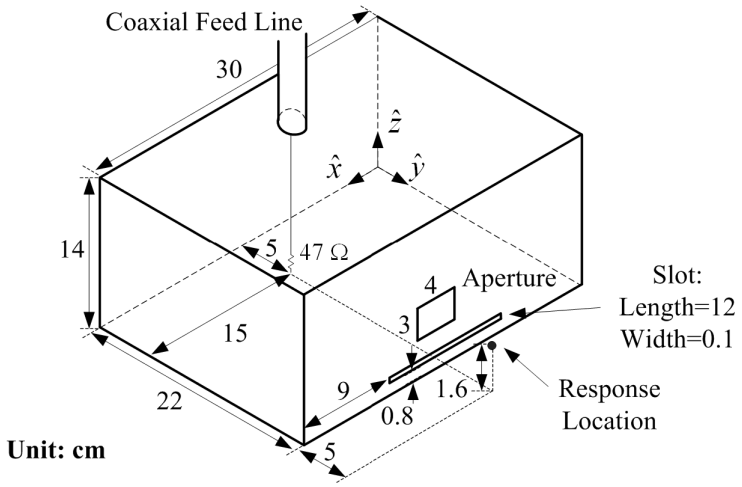

Figure 2.6**:** Geometry of cavity with aperture and slot (dimensions in cm).

In Fig. 2.7, the response is accurately extrapolated using the combined pole-estimation method with $T' = 30.1\,\text{ns}$ ($p = 789$) and $W' = 1\,\text{GHz}$ ($q = 101$). Determining the complete cavity response with CEM methods is very burdensome due to strong resonances and the small dimensions of the slot. Typically, structures of interest in EMI/EMC applications, such as this cavity, are both highly resonant and require wideband characterization. Thus, significant time savings can be gained by extrapolating a response of interest.

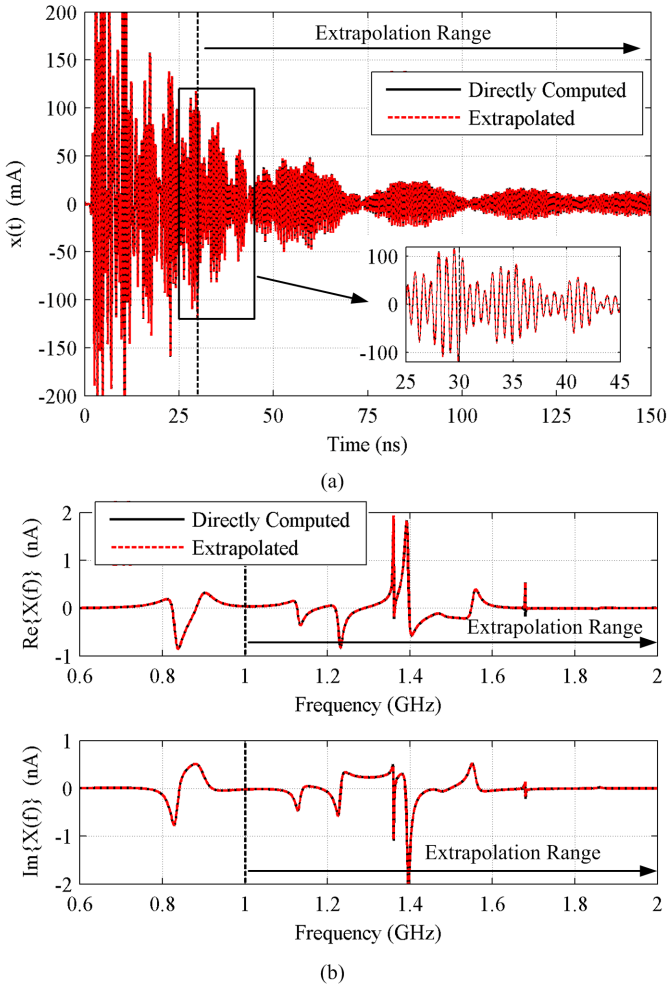

Figure 2.7**:** Extrapolation of (a) time-domain (inset: $25\,\text{ns}$-$45\,\text{ns}$) and (b) frequency-domain electric field response of cavity. Poles ($\mathbf{s}_M$) are estimated using the combined method. Directly-computed and extrapolated responses are nearly indistinguishable indicating an accurate extrapolation.

Example 4: E-Shaped Patch Antenna (with Modeling/Discretization Differences)

The driving-point current of the E-shaped patch antenna is again extrapolated; however, for this case the directly-computed CEM data sets contain differences due to modeling and discretization. The time-domain response is determined with the transmission-line matrix (TLM) method [14] and a volume surrounding the structure is spatially discretized as cubic cells. In the frequency-domain, the surface of the structure is discretized with triangular patches and the response is computed using MoM to solve the electric field integral equation (EFIE) [23]. Thus, the spatial discretizations of the CEM models used to determine the early-time and low-frequency data are fundamentally different. The frequency of the dominant resonance is determined to be 501 MHz by the time-domain model and 496 MHz by the frequency-domain model. In principle, differences between computed responses can be reduced through judicious modeling and discretization of the structure. The driving-point current is particularly challenging because the response is located at the feed point and attention must be paid to the excitation models used. Reducing modeling differences is generally easier if the response is located at point away from the structure/feed. Another effective approach to reduce modeling differences is to use the same discretization for both CEM models. For instance in [2], the EFIE is solved in both the time and frequency domain using an identical triangular surface patch discretization.

Insight into the effect of modeling differences is provided by the results in Fig. 2.8. The response is extrapolated using both early-time (MPM) and low-frequency (VFM) pole-estimation methods. For comparison, the DFT of the MoM frequency-domain data is plotted with the TLM time-domain data. Similarly, the DFT of TLM time-domain data is plotted with the MoM frequency-domain data. In Fig. 2.8, when poles are estimated from early-time data (MPM), the corresponding extrapolation close agrees with the TLM time data; conversely, when poles are estimated from low-frequency data (VFM), the extrapo-

lation closely agrees the MoM frequency data. This is a form of time and frequency bias which is unavoidably introduced when extrapolating the response from early-time and low-frequency data which contain some differences; however, the robustness of the procedure and the GA-based selection of parameters is demonstrated by Fig. 2.8. Despite noticeable differences between time and frequency data, the procedure remains numerically stable and accurately represents the complete response from which the poles are estimated.

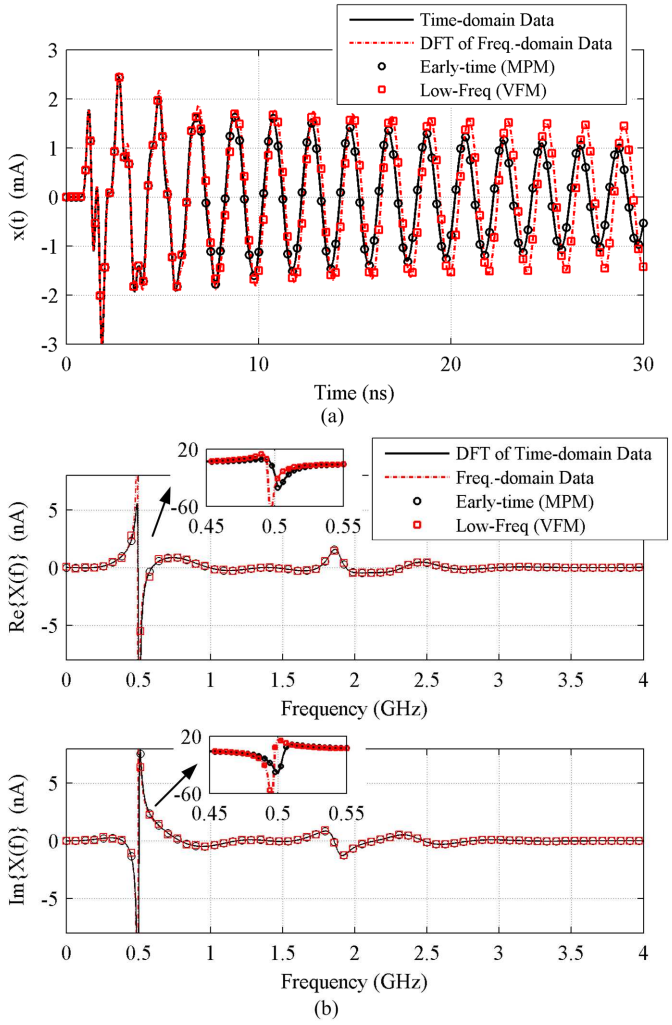

Figure 2.8**:** Extrapolation of (a) time-domain and (b) frequency-domain driving-point current of E-shaped patch antenna with early-time (MPM) and low-frequency (VFM) methods. Directly-computed data contains differences due to modeling and discretization.

2.6 Conclusions

An improved technique to extrapolate a wideband response of a resonant structure using early-time and low-frequency data is presented in this chapter. It is demonstrated that a response may be extrapolated using poles estimated from either early-time or low-frequency data. A procedure is presented to determine polynomial coefficients and pole residues together as the solution to a single matrix equation. The pole estimation process is independent from this process, which allows various pole-estimation techniques to be utilized. Three pole estimation methods are presented and their performance studied as a function of the amounts of CEM data used to extrapolate the response. It is also shown that by properly combining sets of poles determined from early-time and low-frequency data, the amount of CEM data needed to accurately extrapolate a response can be reduced. A GA-based procedure is applied to select all necessary parameters and automate the decision of when enough data has been computed. Numerical examples are presented to demonstrate the applicability of the extrapolation procedure to antenna analysis and EMI/EMC applications.

CHAPTER 3
WIDEBAND EXTRAPOLATION OF SPATIAL RESPONSES OF RESONANT STRUCTURES USING EARLY-TIME AND LOW-FREQUENCY DATA

Abstract

A new procedure is presented to reliably and efficiently extrapolate an electromagnetic response defined in an arbitrary spatial region. In Chapters 1 and 2, responses defined at a single spatial point are simultaneously extrapolated in time and frequency from early-time and low-frequency numerical data. An automated and computationally-efficient approach to extrapolate a spatial response defined in an arbitrary region is described in this chapter. The time and frequency behavior of the response is fitted by polynomials and pole terms, while the spatial variation is accurately represented with sets of spatially-dependent polynomial coefficients and pole residues. It is shown that a single set of poles, common to each discrete spatial location, is sufficient to describe the resonant behavior of response over the entire spatial region. Numerical examples are presented to illustrate the approach. Additionally, a new procedure to reliably distinguish physical poles, which correspond to structural resonances, from fitting poles, which can improve fit accuracy, is described and demonstrated. The spatially-dependent residues of physical pole terms, referred to here as modal residues, are shown to provide important insight into a structure's resonant behavior.

3.1 Introduction

In Chapters 1 and 2, responses defined at a single spatial location, such as the driving-point current of an antenna, are simultaneously extrapolated in time and frequency by fitting early-time and low-frequency numerical data [1, 5]. Early-time and low-frequency

data are mutually complementary and together can provide all the information needed to characterize the complete response [2, 3, 4]. Determining a wideband response of a resonant structure with computational electromagnetic methods (CEM) is often burdensome; however, extrapolation can significantly reduce the computational expense, as the complete response need not be determined exclusively in either domain [1, 5].

An efficient and reliable procedure is presented in this chapter to extrapolate a response defined, not at a single location, but over an arbitrary spatial region, such as a contour, surface, or volume. As with the procedure described in Chapter 2, the time and frequency behavior of a spatial response is fitted here by sums of polynomials and pole terms. It is shown that the spatial variation of a response can be accurately represented with sets of spatially-dependent coefficients for the polynomials and spatially-dependent residues for the pole terms. Additionally, it is demonstrated a *single* set of poles, shared by each spatial location, is sufficient to describe the resonant behavior of response over the *entire* spatial region.

To reliably apply the extrapolation procedure one must select several polynomial and pole-estimation parameters. An automated genetic algorithm (GA)-based procedure is presented in Chapter 2 to select the parameters needed to extrapolate a point response. To extrapolate a spatial response one could apply the procedure of Chapter 2 at each discrete location in the spatial region of interest. This approach is highly inefficient, however, as a separate GA optimization run is required for each discrete point, and there could be hundreds or thousands of points in the spatial region. Alternatively, a spatial response may be extrapolated with a *single* GA optimization run using the computationally-efficient procedure presented in this chapter. All necessary parameters are selected by simultaneously fitting the response, in early time and low frequency, at a small subset of the total number of positions in the spatial region. Using the parameters selected, a single set of poles is

determined with a multi-signal formulation of the matrix pencil method (MPM) [38]. Then coefficients and residues are easily calculated for each spatial location by fitting the early-time and low-frequency data at that location. The response is accurately extrapolated over the entire spatial region despite selecting parameters based on data at only a few locations. In addition to the computational savings, this procedure is preferred because the spatial response is represented with a single set of poles and polynomials, which would not be the case if the procedure of Chapter 2 were applied at each discrete location [5].

A new procedure is also presented to reliably distinguish between *physical poles*, which correspond to structural resonances, and *fitting poles*, which are not related to resonances but can improve the fit of the response. Estimating poles from numerical data with techniques such as MPM typically yields fitting poles along with physical poles. Distinguishing between physical and fitting poles is generally difficult [39, 40, 41], but the procedure in this work automates the process. Identifying physical poles is of great interest because they provide valuable information about the resonances of a structure or system. Additionally, it is shown that the spatial residues of physical pole terms, referred to here as *modal residues*, correspond to natural modal behavior.

3.2 Extrapolation of a Spatial Response

Let $x(\mathbf{r}, t)$ and $X(\mathbf{r}, f)$ denote the time- and frequency-domain representations, respectively, of an EM response at a spatial position $\mathbf{r}$ due to a wideband excitation source. The response corresponds to an EM quantity defined in a spatial region $\mathcal{R}$ which could be, for instance, a contour, surface, or volume (Fig. 3.1). Although a function cannot be strictly band-limited in both time and frequency, it is assumed the response is effectively time-limited to T and frequency-limited to W, such that $x(\mathbf{r}, t) \approx 0$ for $t > T$ and $X(\mathbf{r}, f) \approx 0$ for $f > W$.

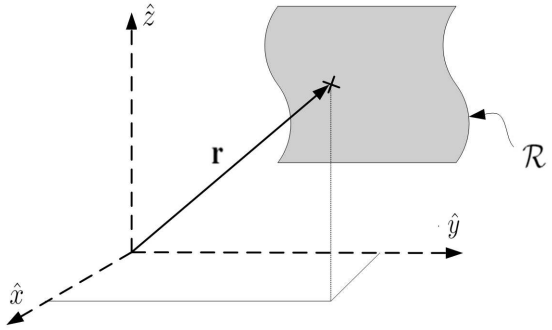

Figure 3.1**:** Illustration of (a) position vector $\mathbf{r}$ and spatial region of interest $\mathcal{R}$.

The early-time and low-frequency ranges of $x(\mathbf{r}, t)$ and $X(\mathbf{r}, f)$ contain high-frequency and late-time information, respectively, and can be processed to determine an accurate representation of the complete response in time and frequency as a sum of weighted polynomials and pole terms. Pole terms can efficiently represent resonant behavior whereas polynomials provide compact support well-suited to characterize the remaining non-resonant behavior [5]. This approach is similar to that of Chapter 2; however, the spatial variation of the response is now also considered.

The responses $x(\mathbf{r},t)$ and $X(\mathbf{r},f)$ are represented by $\hat{x}(\mathbf{r},t)$ and $\hat{X}(\mathbf{r},f)$, which are defined for $\mathbf{r}\in\mathcal{R}$ to be

$$\begin{aligned} x(\mathbf{r},t)\approx\hat{x}(\mathbf{r},t)&=\sum_{n=0}^{N-1}a_n(\mathbf{r})\phi_n(t/\ell_1)+\sum_{m=0}^{M-1}R_m(\mathbf{r})g_m(t) \\ X(\mathbf{r},f)\approx\hat{X}(\mathbf{r},f)&=\sum_{n=0}^{N-1}a_n(\mathbf{r})\Phi_n(f/\ell_2)+\sum_{m=0}^{M-1}R_m(\mathbf{r})G_m(f)\ . \end{aligned} \tag{3.1}$$

In (3.1), $\phi_n\left(t/\ell_1\right)$ and $\Phi_n\left(f/\ell_2\right)$ denote nth $-$ order polynomials which are scaled by factors ℓ_1 and ℓ_2 $\left(\ell_2=1/\left(2\pi\ell_1\right)\right)$ [28], related by the Fourier transform, and each weighted by a spatially-dependent, real-valued coefficient $a_n(\mathbf{r})$ (see Chapter 1, Appendix A). The mth pole term is defined as $g_m\left(t\right)=\exp\left(s_mt\right)$ in the time domain and as $G_m\left(f\right)=1/\left(j2\pi f-s_m\right)$ in the frequency domain. Each pole term is weighted by a spatially-dependent, complex residue $R_m(\mathbf{r})$. The mth complex pole is $s_m=\alpha_m+j2\pi f_m$, where α_m and f_m are the damping factor and resonant frequency, respectively. The set of M poles is $\mathbf{s}_M=\left[s_0,s_1,\ldots,s_{M-1}\right]^{\mathrm{T}}$, where $[\cdot]^{\mathrm{T}}$ denotes the transpose. Each α_m is negative and pole terms occur in complex conjugate pairs to yield a real-valued time response.

In (3.1), the time and frequency behavior is represented by N polynomials and M pole terms, whereas the spatial variation is described by $a_n(\mathbf{r})$ and $R_m(\mathbf{r})$. In general, N and M could be a function of **r**, however, (3.1) is a more compact representation that uses a *single* set of N polynomials and M pole terms.

To successfully extrapolate a response by representing it as (3.1), one must determine $a_n(\mathbf{r})$, $R_m(\mathbf{r})$, and a set of poles $\mathbf{s}_M$, such that $\hat{x}(\mathbf{r},t)$ and $\hat{X}(\mathbf{r},f)$ accurately represent $x(\mathbf{r},t)$ and $X(\mathbf{r},f)$, respectively, for time and frequency points of interest. To do so, one first uses CEM methods to determine numerical values of $x(\mathbf{r},t)$ and $X(\mathbf{r},f)$ at discrete spatial positions in $\mathcal{R}$ for each early-time and low-frequency point, respectively.

Let $\mathbf{r}_i$ denote the ith discrete spatial position in $\mathcal{R}$ (Fig. 3.2). The total number of positions in $\mathcal{R}$ is denoted by I, and the corresponding set of position vectors is $\mathcal{I} = \{\mathbf{r}_1, \mathbf{r}_2, \ldots, \mathbf{r}_i, \ldots, \mathbf{r}_I\}$.

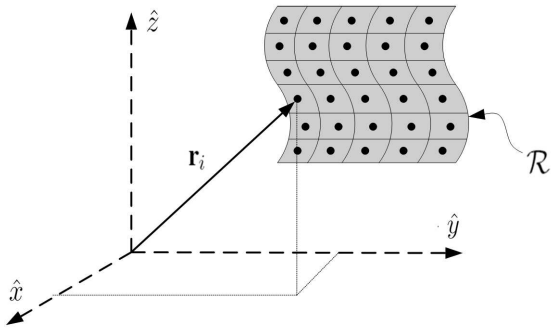

Figure 3.2**:** Illustration of discretized $\mathcal{R}$ and discrete spatial location $\mathbf{r}_i$.

The discrete time-domain response at $\mathbf{r}_i$ is denoted as $\mathbf{x}^i$ and contains P time samples of $x(\mathbf{r}_i, t)$ at Δt intervals. It can be partitioned into early-time and late-time data as $\mathbf{x}^i = [\mathbf{x}^i_{\mathrm{ET}}; \mathbf{x}^i_{\mathrm{LT}}]$, where $\mathbf{x}^i_{\mathrm{ET}}$ contains p early-time samples of $\mathbf{x}^i$. Similarly, let $\mathbf{X}^i$ denote the discrete frequency-domain response at $\mathbf{r}_i$ which contains Q samples of $X(\mathbf{r}_i, f)$ at Δf intervals. It can be partitioned into low-frequency and high-frequency data as $\mathbf{X}^i = \left[\mathbf{X}^i_{\mathrm{LF}}; \mathbf{X}^i_{\mathrm{HF}}\right]$, where $\mathbf{X}^i_{\mathrm{LF}}$ contains q low-frequency samples of $\mathbf{X}^i$. The early-time and low-frequency data vectors at $\mathbf{r}_i$ are written as

$$\begin{aligned} \mathbf{x}^i_{\mathrm{ET}} &= \left[x(\mathbf{r}_i, t_1), x(\mathbf{r}_i, t_2), \ldots, x(\mathbf{r}_i, t_p)\right]^{\mathrm{T}} \\ \mathbf{X}^i_{\mathrm{LF}} &= \left[X(\mathbf{r}_i, f_1), X(\mathbf{r}_i, f_2), \ldots, X(\mathbf{r}_i, f_q)\right]^{\mathrm{T}} \end{aligned} \tag{3.2}$$

where $t_k = (k-1)\Delta t$ and $f_k = (k-1)\Delta f$. To apply the procedure, $\mathbf{x}^i_{\mathrm{ET}}$ and $\mathbf{X}^i_{\mathrm{LF}}$ in (3.2) for the I positions in $\mathcal{R}$ are first determined with CEM methods. The spatial response is extrapolated by obtaining $\mathbf{s}_M$ and then solving for $\mathbf{a}_N(\mathbf{r}_i)$ and $\mathbf{R}_M(\mathbf{r}_i)$ for each $\mathbf{r}_i$. In this work, a $\mathbf{s}_M$ is determined from early-time data by applying a multi-signal formulation of

MPM (see Section 3.3).

After determining the poles, $\mathbf{a}_N(\mathbf{r}_i)$ and $\mathbf{R}_M(\mathbf{r}_i)$ are found by fitting $\mathbf{x}^i_{\mathrm{ET}}$ and $\mathbf{X}^i_{\mathrm{LF}}$ and solving a system of $(p+q)$ linear equations, for each $\mathbf{r}_i$, written as

$$\begin{bmatrix} \boldsymbol{\phi}_N[t_{\mathrm{ET}}] & \mathbf{g}_M[t_{\mathrm{ET}}] \\ \boldsymbol{\Phi}_N[f_{\mathrm{LF}}] & \mathbf{G}_M[f_{\mathrm{LF}}] \end{bmatrix} \begin{bmatrix} \mathbf{a}_N(\mathbf{r}_i) \\ \mathbf{R}_M(\mathbf{r}_i) \end{bmatrix} = \begin{bmatrix} \mathbf{x}^i_{\mathrm{ET}} \\ \mathbf{X}^i_{\mathrm{LF}} \end{bmatrix} . \tag{3.3}$$

In (3.3), the polynomial coefficient and pole residue vectors for $\mathbf{r}_i$ are

$$\begin{aligned} \mathbf{a}_N(\mathbf{r}_i) &= \left[a_0\left(\mathbf{r}_i\right), a_1\left(\mathbf{r}_i\right), \ldots, a_{N-1}\left(\mathbf{r}_i\right)\right]^{\mathrm{T}} \\ \mathbf{R}_M(\mathbf{r}_i) &= \left[R_0\left(\mathbf{r}_i\right), R_1\left(\mathbf{r}_i\right), \ldots, R_{M-1}\left(\mathbf{r}_i\right)\right]^{\mathrm{T}} . \end{aligned} \tag{3.4}$$

The matrices obtained by evaluating the polynomials and poles at early-time and low-frequency points are written as

$$
\begin{aligned}
\boldsymbol{\phi}_N[t_{\mathrm{ET}}] &= \begin{bmatrix} \phi_0\left(t_1/\ell_1\right) & \cdots & \phi_{N-1}\left(t_1/\ell_1\right) \\ \vdots & \ddots & \vdots \\ \phi_0\left(t_p/\ell_1\right) & \cdots & \phi_{N-1}\left(t_p/\ell_1\right) \end{bmatrix} \\
\mathbf{g}_M[t_{\mathrm{ET}}] &= \begin{bmatrix} g_0\left(t_1\right) & \cdots & g_{M-1}\left(t_1\right) \\ \vdots & \ddots & \vdots \\ g_0\left(t_p\right) & \cdots & g_{M-1}\left(t_p\right) \end{bmatrix} \\
\boldsymbol{\Phi}_N[f_{\mathrm{LF}}] &= \begin{bmatrix} \Phi_0\left(f_1/\ell_2\right) & \cdots & \Phi_{N-1}\left(f_1/\ell_2\right) \\ \vdots & \ddots & \vdots \\ \Phi_0\left(f_q/\ell_2\right) & \cdots & \Phi_{N-1}\left(f_q/\ell_2\right) \end{bmatrix} \\
\mathbf{G}_M[f_{\mathrm{LF}}] &= \begin{bmatrix} G_0\left(f_1\right) & \cdots & G_{M-1}\left(f_1\right) \\ \vdots & \ddots & \vdots \\ G_0\left(f_q\right) & \cdots & G_{M-1}\left(f_q\right) \end{bmatrix}.
\end{aligned} \tag{3.5}
$$

For practical cases $(p+q) > (N+M)$ and (3.3) is an overdetermined system for which a least-squares solution can be determined [16]. As a consequence of (3.1) the matrices in (3.5) are not a function of $\mathbf{r}_i$ and therefore need only be filled once when solving (3.3) for each of the I spatial positions. The extrapolation is successful if $\hat{x}(\mathbf{r},t)$ and $\hat{X}(\mathbf{r},f)$ in (3.1) accurately represent the response, at each $\mathbf{r}_i$, in the directly-computed early-time and low-frequency ranges, as well as in the extrapolated late-time and high-frequency ranges.

3.3 Reliable Selection of Parameters

A successful extrapolation depends on the choice of three *pole-estimation parameters* and three *polynomial parameters* needed to determine the pole set $\mathbf{s}_M$, and coefficients $\mathbf{a}_N(\mathbf{r}_i)$ and residues $\mathbf{R}_M(\mathbf{r}_i)$ in (3.1), respectively. In this work all parameters are efficiently and reliably selected by fitting the response, in early time and low frequency, at a small number of locations in $\mathcal{R}$. The procedure is automated with a GA.

A. Extrapolation Parameters

Three polynomial parameters must be selected: the time scaling factor ℓ_1, number of terms N, and time center τ [1, 2]. These are the same parameters which must be selected to extrapolate a point response. The selection of the time scaling factor ℓ_1 defines the support of the polynomials, which in this work are associate Hermite (AH) functions (see Chapter 1, Appendix A and [28]). The value of N specifies the number of polynomials in (3.1), whereas time center τ denotes the time shift of the origin of the polynomials. To reliably extrapolate the spatial response $\{N, \ell_1, \tau\}$ must be properly selected.

Parameters associated with the pole-estimation method must also be selected. While MPM is numerically efficient and robust [9], its accuracy depends on the subset of early-time samples processed. This subset can be specified by the beginning and ending time samples p_1 and p_2, and a decimation factor d [1, 9] (see Chapter 1). The success of the extrapolation depends on the proper selection of $\{p_1, p_2, d\}$, which allows one to determine $\mathbf{s}_M$ with MPM. Because MPM estimates poles from early-time data, a time-domain bias is consequently introduced as discussed in Chapter 2 [5]. It should be noted that poles could have been estimated from frequency-domain data instead using a technique such as the vector fitting method [30].

B. Parameter Selection

A response at a point in space can be reliably extrapolated by applying the GA-based procedure in Chapter 2. A spatial response in $\mathcal{R}$ may be thought of as I point responses at positions $\mathbf{r}_i$ for $i = 1, 2, \ldots, I$. Each of the I point responses could be extrapolated by applying a separate GA optimization run to select parameters and fit the response at each $\mathbf{r}_i$. The computational expense of this approach, however, is prohibitive because I optimization runs are required, which even for moderate-size regions can be large. Additionally, by selecting parameters at each $\mathbf{r}_i$, N and M of (3.1) are not necessarily constant over $\mathcal{R}$. For efficiency it is desired to represent the response with a *single* set of N polynomials and M pole terms.

Instead of selecting parameters by fitting the response at *each* $\mathbf{r}_i$, a second approach is to select parameters by fitting the response at a *single* position $\mathbf{r}'_i$ selected from $\mathcal{I} = \{\mathbf{r}_1, \mathbf{r}_2, \ldots, \mathbf{r}_I\}$. The set of poles and polynomial parameters determined by fitting the response at $\mathbf{r}'_i$ may then be used in (3.3) to determine $\mathbf{a}_N(\mathbf{r}_i)$ and $\mathbf{R}_M(\mathbf{r}_i)$ for the other $I - 1$ positions. While this approach gives constant values for M and N, the parameters selected by fitting at only $\mathbf{r}'_i$ may not (and do not in practice) provide a good fit at all other spatial positions, and $\mathbf{s}_M$ may not contain accurate estimates of all the poles.

A more efficient and reliable procedure to extrapolate a spatial response than the two described above is to select extrapolation parameters based on *simultaneously* fitting the response at a small subset of the I positions in $\mathcal{R}$. This subset of positions is denoted by $\mathcal{K} = \{\mathbf{r}'_1, \mathbf{r}'_2, \ldots, \mathbf{r}'_K\}$, which contains K positions randomly selected from $\mathcal{I}$ and one hopes that $K \ll I$. With this approach one uses MPM to estimate a single set of poles by simultaneously processing early-time data at the K positions in $\mathcal{K}$. To determine the coefficients and residues, the system of equations in (3.3), which fits the response at a single position, is modified to fit the response at K positions (see Section 3.3, *D*). A GA is

used to select parameters which yield an accurate representation of the response at each of the K locations (see Section 3.3, *C*). After $\{p_1, p_2, d\}$ and $\{N, \ell_1, \tau\}$ are selected, MPM is used to determine $\mathbf{s}_M$, and $\mathbf{a}_N(\mathbf{r}_i)$ and $\mathbf{R}_M(\mathbf{r}_i)$ are found by solving (3.3) at each $\mathbf{r}_i$. The computational expense of solving (3.3) is minimal after the polynomial and pole parameters have been selected.

Instead of selecting the K fitting locations in a geometrically-regular arrangement, in this work the positions are randomly distributed in $\mathcal{R}$. The exact locations of the positions are not critical, but rather simultaneously fitting at multiple locations should provide the diversity needed to accurately extrapolate the entire response. Selecting the K positions in a random arrangement attempts to avoid fitting at positions corresponding to nulls of the response at each resonance. Thus, the random arrangement increases the likelihood that an accurate set of poles will be determined.

C. GA Minimization

Extrapolation agreement is a function of each parameter described in Section 3.3, *A*. The optimal set of parameters minimize the difference between the directly-computed response and extrapolated representation in (3.1). The extrapolation agreement at $\mathbf{r}_i$, denoted E_i, can be quantified with a normalized mean square difference, averaged in time and frequency (Eq. 1.8). The goal is to select parameters which minimize E_i at each $\mathbf{r}_i$ and thus successfully extrapolate the spatial response by obtaining $\hat{x}(\mathbf{r}, t)$ and $\hat{X}(\mathbf{r}, f)$ in (3.1) that accurately represent the responses for all time and frequency. Computing E_i, however, requires the complete responses, which will not be known in practice. An approximation of E_i, denoted $\hat{E}_i$, requires only $\mathbf{x}^i_{\mathrm{ET}}$ and $\mathbf{X}^i_{\mathrm{LF}}$ and can be minimized instead (Eq. 1.9). The definition of $\hat{E}_i$ utilizes the fast Fourier transform (FFT) to estimate agreement in the unknown late-time and high-frequency regions [4].

In Chapters 1 and 2 it shown a point response can be reliably extrapolated by using parameters found with GA optimization to minimize $\hat{E}_i$. For the procedure in this work, extrapolation agreement must be considered at K spatial positions. Thus, parameters are selected using a GA to minimize $\hat{E}_{\mathcal{K}}$, which is the mean of $\hat{E}_i$ over the K locations of $\mathcal{K}$, written as

$$\hat{E}_{\mathcal{K}} = \frac{1}{K} \sum_{i=1}^{K} \hat{E}_i. \tag{3.6}$$

After using a GA to select parameters that minimize $\hat{E}_{\mathcal{K}}$ in (3.6), one solves the system of equations in (3.3) for each $\mathbf{r}_i$ to determine $\mathbf{a}_N(\mathbf{r}_i)$ and $\mathbf{R}_M(\mathbf{r}_i)$. In this way, the CEM data at each discrete location is fit and a representation for the complete spatial response obtained.

D. Fitting with a Small Subset of Spatial Positions

Extrapolating a spatial response with the procedure described above requires that a single set of poles be determined by simultaneously processing early-time data at K spatial locations. The standard MPM algorithm, however, determines the poles of a single signal [9]. In this work a multi-signal variation of MPM, described in [38], is utilized to process data from K positions and determine a single set of poles. In [38] the data processed corresponds to transient signals scattered by a structure and observed at different look angles. It is assumed the same set of poles is present in each signal, but with the weighting of each pole term variable based on the angle of observation. These assumptions are applied here to a spatial response. The poles are intrinsic to the structure whereas the weighting of each pole term has spatial dependence as in (3.1).

The system of equations in (3.3) fits the response at a single location $\mathbf{r}_i$ but can be

modified to fit the response at K spatial locations, defined by $\mathcal{K} = \{\mathbf{r}'_1, \mathbf{r}'_2, \ldots, \mathbf{r}'_K\}$, as

$$\begin{bmatrix} \boldsymbol{\phi}_N[t_{\mathrm{ET}}] & \boldsymbol{g}_M[t_{\mathrm{ET}}] \\ \Phi_N[f_{\mathrm{LF}}] & \boldsymbol{G}_M[f_{\mathrm{LF}}] \end{bmatrix} \begin{bmatrix} \mathbf{a}_N[\mathcal{K}] \\ \mathbf{R}_M[\mathcal{K}] \end{bmatrix} = \begin{bmatrix} \mathbf{x}^{\mathcal{K}}_{\mathrm{ET}} \\ \mathbf{X}^{\mathcal{K}}_{\mathrm{LF}} \end{bmatrix}. \tag{3.7}$$

In (3.7), $\mathbf{a}_N[\mathcal{K}]$ is a $(N \times K)$ matrix containing polynomials coefficients

$$\mathbf{a}_N[\mathcal{K}] = \begin{bmatrix} a_0(\mathbf{r}'_1) & \cdots & a_0(\mathbf{r}'_K) \\ \vdots & \ddots & \vdots \\ a_{N-1}(\mathbf{r}'_1) & \cdots & a_{N-1}(\mathbf{r}'_K) \end{bmatrix} \tag{3.8}$$

and $\mathbf{R}_M[\mathcal{K}]$ is a $(M \times K)$ matrix containing pole residues

$$\mathbf{R}_M[\mathcal{K}] = \begin{bmatrix} R_0(\mathbf{r}'_1) & \cdots & R_0(\mathbf{r}'_K) \\ \vdots & \ddots & \vdots \\ R_{M-1}(\mathbf{r}'_1) & \cdots & R_{M-1}(\mathbf{r}'_K) \end{bmatrix}. \tag{3.9}$$

The data vectors in (3.7) containing early-time and low-frequency CEM data are

$$\mathbf{x}^{\mathcal{K}}_{\mathrm{ET}} = \begin{bmatrix} x(\mathbf{r}'_1, t_1) & \cdots & x(\mathbf{r}'_K, t_1) \\ \vdots & \ddots & \vdots \\ x(\mathbf{r}'_1, t_p) & \cdots & x(\mathbf{r}'_K, t_p) \end{bmatrix} \tag{3.10}$$

$$\mathbf{X}^{\mathcal{K}}_{\mathrm{LF}} = \begin{bmatrix} X(\mathbf{r}'_1, f_1) & \cdots & X(\mathbf{r}'_K, f_1) \\ \vdots & \ddots & \vdots \\ X(\mathbf{r}'_1, f_q) & \cdots & X(\mathbf{r}'_K, f_q) \end{bmatrix}. \tag{3.11}$$

The matrices in (3.5) appear in (3.7) and are unchanged by the extension of (3.3) to fit at K positions. It is preferable to select a small K because the computational expense of

solving (3.7) is proportional to K, as (3.8)-(3.11) each have K columns. The system in (3.7), combined with MPM applied to multiple data sets, allows one to select the necessary parameters with a GA by fitting the response at K positions and minimizing $\hat{E}_{\mathcal{K}}$ in (3.6). The selection of $\{p_1, p_2, d\}$ allows $\mathbf{s}_M$ to be determined with MPM, and $\{N, \ell_1, \tau\}$ are used when solving (3.3) at each $\mathbf{r}_i$ in $\mathcal{R}$.

3.4 Determining Physical Poles

Poles estimated from numerical data using techniques such as MPM can be classified as *physical poles*, corresponding to structural resonances, and *fitting poles*, which are not associated with resonances but can improve the fit of the response. It is desirable to identify physical poles when representing a response as in (3.1), but distinguishing them from fitting poles is often difficult when the resonant frequencies are unknown.

A few procedures have been presented in the literature to distinguish between physical and fitting poles. In [39], MPM and Prony's method [42] are each applied to estimate the poles of a response. The poles coincident in the sets of poles determined by the two techniques are taken to be the physical poles whereas non-coincident poles are assumed to be the fitting poles. In [41], MPM is applied to estimate the poles of a response by processing subsets of time samples with each extending later in time. The sets of poles are compared and those coincident in each set are assumed to be physical poles.

A new automated procedure is presented to distinguish between physical and fitting poles is as follows. First, one uses MPM to estimate poles at K spatial locations randomly distributed in $\mathcal{R}$ as described in Section 3.3. Three sets of poles are determined by fitting the response at different sets of K position vectors denoted $\mathcal{K}_1$, $\mathcal{K}_2$, and $\mathcal{K}_3$, respectively. The resulting sets of poles are compared, and the poles coincident in all three sets are taken to

be the physical poles, whereas non-coincident poles are the fitting poles. After identifying the physical poles a response can be represented, as in (3.1), with each of the M pole terms corresponding to a physical pole. To determine a representation with polynomials and physical poles only, fitting poles are removed from $\mathbf{s}_M$, then coefficients and residues are determined by solving (3.3) for each $\mathbf{r}_i$.

The procedure described is motivated by the fact that physical poles are intrinsic to the structure, and therefore only a single set of poles is needed to represent a spatial response. The locations of fitting poles, on the other hand, are not unique. When the K fitting locations are varied, the fitting poles are also found to vary whereas the physical poles do not. This observation is used to distinguish between physical and fitting poles.

The spatial residues of physical poles, referred to here as *modal residues*, can provide insight into the resonant behavior of a structure, whereas the spatial residues of fitting poles do not. Modal residues are found to have spatial behavior similar to the natural modes determined by the singularity expansion method (SEM) [43]. The set of modal residues can be viewed as a decomposition of a response into the characteristic spatial behavior of each resonance. This perspective can be useful in applications where the effects of certain resonances must be suppressed or enhanced, for example, by excitation selection or changing physical dimensions.

Modal residues depend on the EM quantity of the response, as well as the spatial region where the response is defined. Additionally, to determine a physical pole from response data, the corresponding resonance must be excited by the excitation/feed arrangement. The excitation bandwidth determines the highest resonant frequency which can be resolved.

3.5 Numerical Results

Numerical examples are now presented to demonstrate the extrapolation procedure described. Two wideband spatial responses are extrapolated from early-time and low-frequency data.

Example 1: Dipole Antenna

The first spatial response considered is the axial current of a thin-wire cylindrical dipole antenna, aligned along the z axis, with length $L = 0.5$ m and radius $a = 2.5$ cm. The spatial region $\mathcal{R}$ is specified by $z \in [0, L]$, and it contains $I = 99$ discrete, equally-spaced locations along the length of the dipole. The dipole is driven at its center with a differentiated Gaussian pulse (DGP) voltage excitation, with effective frequency content up to $f_{max} = 3$ GHz (see Chapter 1). The electric field integral equation is solved with MoM [23] to determine the frequency-domain current at each of the 99 locations. The response is sampled at $\Delta f = 3$ MHz intervals up to 3 GHz. The time-domain response, which is sampled at $\Delta t = 8$ ps up to 35 ns, is obtained by taking the discrete Fourier transform (DFT) of the IE/MoM data. A time-domain CEM method could be used, but this approach removes discretization or modeling differences, which is convenient for the present purpose.

The current is successfully extrapolated using 15 ns of early-time data and 1.5 GHz of low-frequency data. A GA is used to select parameters that minimize $\hat{E}_{\mathcal{K}}$ by fitting the response at $K = 5$ positions randomly selected from the total of 99. The exact locations of the 5 fitting positions are found not to be critical to the success of the extrapolation, but rather by simultaneously fitting at K locations, the diversity needed to select the necessary parameters is provided.

The current determined with IE/MoM (Directly Computed) and two extrapolated representations of the spatial responses ($\hat{x}(\mathbf{r}, t)$ and $\hat{X}(\mathbf{r}, f)$ in (3.1)) are compared for several

values of time (Fig. 3.3) and frequency (Fig. 3.4). The close agreement among the three curves for the points shown is typical of all time and frequencies of interest. The first extrapolated response (Physical & Fitting Poles) is represented as in (3.1) with polynomials and *both* physical and fitting pole terms, while the second includes polynomials and *only* physical pole terms. Agreement among the three curves is excellent, indicating polynomials can provide the support for response behavior otherwise represented by fitting poles.

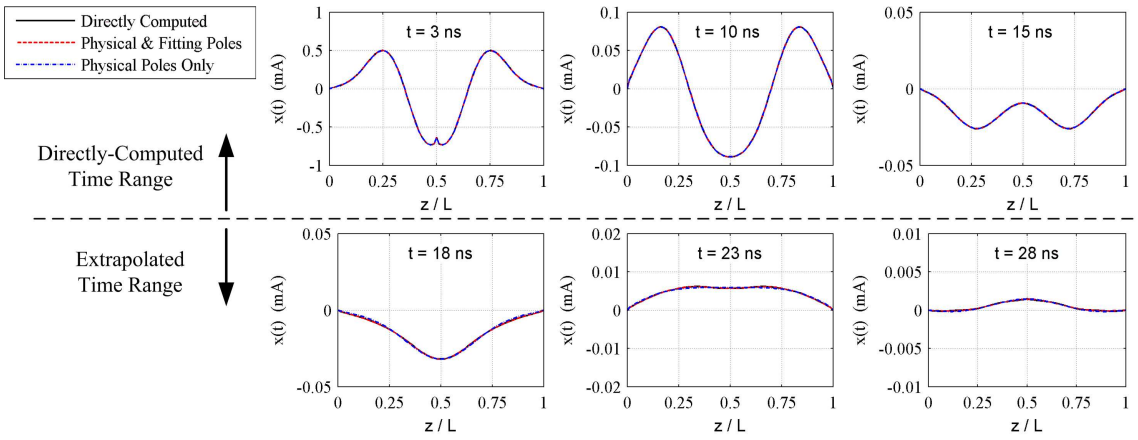

Figure 3.3**:** Axial current of center-fed dipole for several values of time. Directly-computed response, representation with polynomials, physical, and fitting pole terms, and representation with polynomials and physical pole terms only are nearly indistinguishable, indicating a successful extrapolation ($K = 5$).

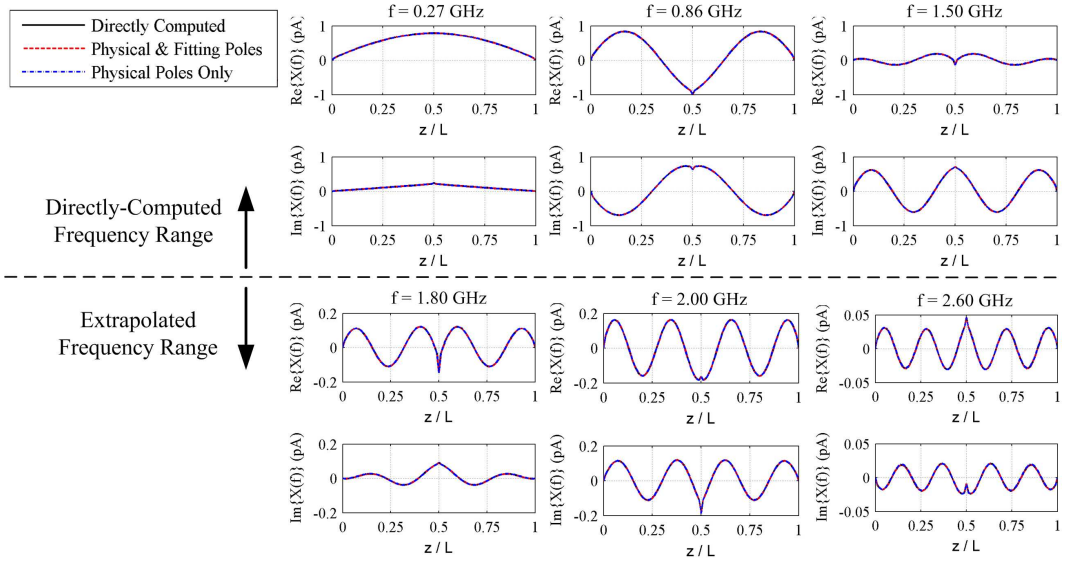

Figure 3.4**:** Axial current of center-fed dipole for several values of frequency. Directly-computed response, representation with polynomials, physical, and fitting pole terms, and representation with polynomials and physical pole terms only are nearly indistinguishable, indicating a successful extrapolation ($K = 5$).

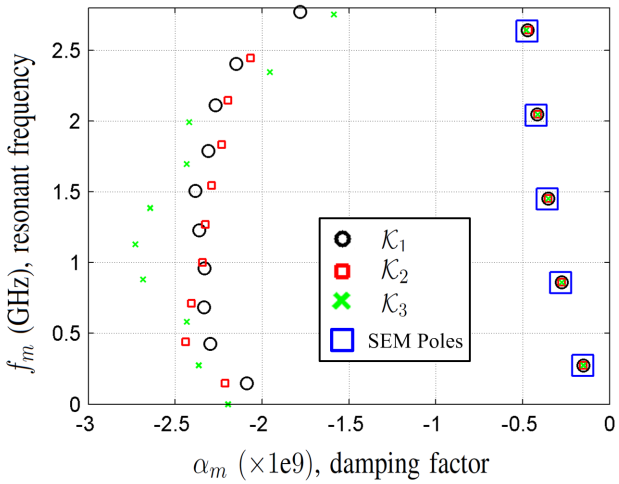

Figure 3.5**:** Poles of the dipole determined by fitting the response at $K = 5$ spatial locations using three different sets of K position vectors denoted $\mathcal{K}_1$, $\mathcal{K}_2$, and $\mathcal{K}_3$. Physical poles are coincident in the three sets of poles whereas fitting poles are not. SEM poles of the dipole are shown for comparison.

The poles $(s_m = \alpha_m + j2\pi f_m)$ of the response for three successful extrapolations are shown in Fig. 3.5. Parameters are selected by fitting the response at three different sets of 5 randomly selected locations, denoted $\mathcal{K}_1$, $\mathcal{K}_2$, and $\mathcal{K}_3$. In Fig. 3.5 the five poles coincident in the three pole sets are the physical poles, whereas the non-coincident poles are the fitting poles.

The SEM poles of the dipole, which correspond to the complex natural resonances [43], provide a reference. In Fig. 3.5 the physical poles determined by extrapolating IE/MoM data are shown to closely agree with the SEM poles in [43]. The average relative difference for the resonant frequencies is 0.23% and is 1.15% for the damping factors. The disagreement can be attributed in part to differences between the spatial discretization used in [43] and that in this work.

The physical poles correspond to dipole resonances excited by the excitation and feeding arrangement. Higher-order resonances may be determined by increasing f_{max}. The resonances occur when the electrical length of the dipole is approximately equal to an odd

multiple of a half-wavelength, i.e., $L \approx [(2m-1)\,\lambda]/2$ for $m = 1, 2, 3, 4, 5$. The five physical poles are used with polynomials to represent the response (Physical Poles Only) in Figs. 3.3 and 3.4.

The modal residues of the dipole $R_m(z)$ determined by extrapolating the CEM data are shown in Fig. 3.6. The natural resonant behavior is apparent as the lowest-order residue ($m = 1$) resembles a half-wavelength sinusoid and high-order modal residues contain $[(2m-1)\,\lambda]/2$ wavelengths. The results in Fig. 3.6 can be interpreted as a decomposition of the current into modal functions, each associated with a structural resonance. Thus, the dipole current can be thought of as a superposition of the set of physical pole terms weighted by modal residues.

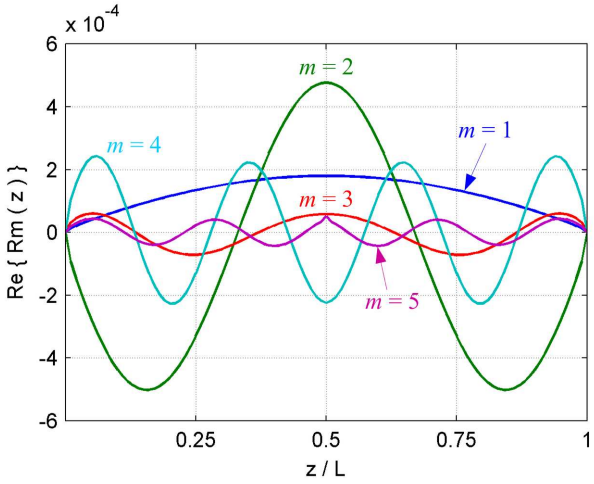

(a)

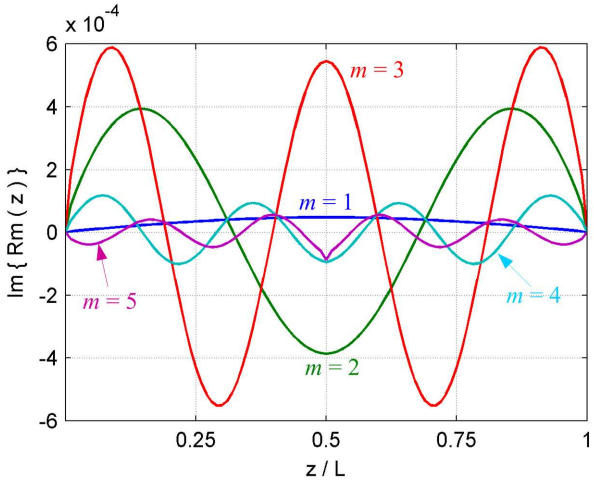

(b)

Figure 3.6**:** The modal residues $R_m(z)$ associated with the physical poles of a center-fed dipole: (a) real part, (b) imaginary part. Residues are determined by extrapolating CEM early-time and low-frequency data and representing the dipole current as in (3.1).

The value of extrapolation agreement E_i determined at each of the $I = 99$ positions on the dipole is illustrated in Fig. 3.7. The value of E_i quantifies the agreement between the directly-computed response and an extrapolated representation, where $E_i < 10^{-2}$ is desired [5]. The two dashed/red curves in Fig. 3.7 correspond to the two extrapolated responses shown in Figs. 3.3 and 3.4, which are determined with a single GA optimization run to select parameters by fitting simultaneously at 5 locations. Conversely, for the two solid/black curves in Fig. 3.7, the response is extrapolated with the procedure of Chapter 2 with MPM [5] by applying a separate GA optimization run at each of the 99 spatial locations. This approach provides a lower bound on the value of E_i. Fig. 3.7 shows only small gains in extrapolation agreement can be obtained with $K > 5$, because $K = 5$ closely approaches the lower bound. Thus, the response is accurately extrapolated with $K \ll I$ as desired.

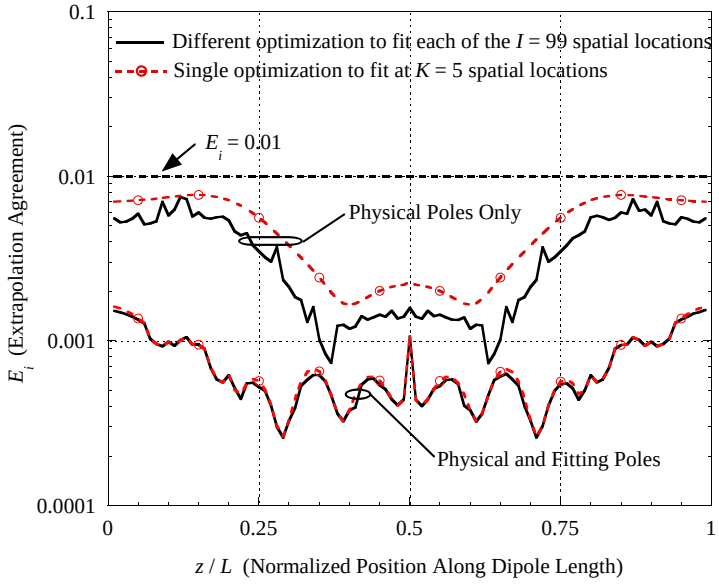

Figure 3.7**:** Comparison of the extrapolation agreement E_i for the axial current of a center-fed dipole.

Extrapolating the response using the approach in this work requires a *single* optimization run, whereas applying the procedure of Chapter 2 requires 99 optimization runs. Reducing the number of optimizations required yields significant computational savings. To illustrate the computational differences, the procedure of Chapter 2 was applied to extrapolate the response at each of the 99 positions in $\mathcal{R}$. Using the palmetto cluster at Clemson University [44], the 99 GA optimization runs needed to extrapolate the complete response required a total of 900 min. of CPU time, with the average time required to extrapolate the response at a single spatial location requiring 9.1 min. Extrapolating the spatial response with the procedure in this work required only 15.1 min.

The results in Fig. 3.7 also compare agreement between representations with polynomials and *both* physical and fitting poles and representations with polynomials and *only* physical poles. The value of E_i for the representations with polynomials and both physical and fitting poles is the lowest; however, the extrapolation agreement of the representation with polynomials and only physical poles is still $E_i < 10^{-2}$. Figs. 3.3 and 3.4 show that the representation with polynomials and only physical poles is nearly indistinguishable from the directly-computed response and therefore, the response of the dipole is still accurately represented as polynomials and physical poles only. A representation of a response with only physical poles can be valuable in providing insight into the resonant behavior, but for best accuracy one may chose to use fitting poles in any extrapolation even with full knowledge of the physical poles.

To consider the effects of CEM modeling differences, the dipole response was determined in early time using a FDTD simulation and in low frequency using IE/MoM. The response was successfully extrapolated, despite discretization differences, using FDTD data up to 15 ns and IE/MoM data up to 1.5 GHz. The agreement between SEM poles and those determined via extrapolation is very good with an average relative difference of 1.54% for

resonant frequencies and 1.51% for damping factors. The agreement is limited as expected by discretization differences between the FDTD and IE/MoM models [1, 5].

Example 2: Patch Antenna

The second resonant structure considered is a $4\,\text{cm} \times 6\,\text{cm}$ rectangular patch antenna (Fig. 3.8). A DGP voltage excitation with $f_{max} = 7\,\text{GHz}$ is applied at the base of a probe feed connecting the ground plane and patch. The spatial response considered is the electric field E_z in a $6\,\text{cm} \times 8\,\text{cm}$ region in the $xy-$ plane between the patch and ground plane defined by $z = h/2$, $x \in [-3\,\text{cm}, 3\,\text{cm}]$, and $y \in [-4\,\text{cm}, 4\,\text{cm}]$ (Fig. 3.8). The region $\mathcal{R}$ is discretized into cells with $\Delta x = \Delta y = 2\,\text{mm}$, resulting in 30 and 40 locations along the x and y directions, respectively, for a total of $I = 1,200$.

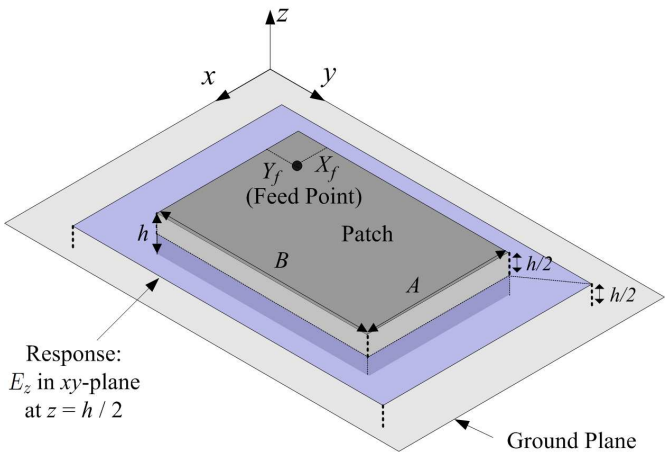

Figure 3.8**:** Geometry of rectangular patch antenna ($A = 4\,\text{cm}$, $B = 6\,\text{cm}$, $h = 0.5\,\text{cm}$, $X_f = 1\,\text{cm}$, $Y_f = 0.8\,\text{cm}$). The ground plane is $8\,\text{cm} \times 12\,\text{cm}$ and the E_z response region is $6\,\text{cm} \times 8\,\text{cm}$.

The patch antenna is modeled with commercial FDTD software [45] and the time-domain response is determined at each of the $1,200$ spatial positions. The electric field is sampled at $\Delta t = 54.2\,\text{ps}$ intervals up to $73.8\,\text{ns}$. The frequency-domain response, which is sampled at $\Delta f = 7\,\text{MHz}$ intervals up to $7\,\text{GHz}$, is determined as the DFT of the time

response.

The spatial response of the patch antenna is successfully extrapolated using 10 ns of early-time data and 2.5 GHz of low-frequency data. All parameters are selected with a GA to minimize $\hat{E}_K$ by fitting at 10 spatial locations randomly selected from the $1,200$ positions in $\mathcal{R}$. Figs. 3.9 and 3.10 illustrate the accuracy of the extrapolation. For several points in time (3.9) and frequency (3.10), the directly-computed response is compared with an extrapolated representation using polynomials and physical pole terms only as in (3.1). The excellent agreement seen in Figs. 3.9 and 3.10 is typical of all time and frequency points of interest. The value of I for this example is significantly higher than the dipole response, and thus 10 fitting locations are used instead of 5. Selecting parameters by fitting at $K > 10$ positions does not yield a more accurate extrapolation, and thus $K \ll I$ provides the diversity needed. It was again found that the specific locations of the 10 fitting locations is not critical to the success of the extrapolation.

To illustrate the efficiency of the procedure in this work, the patch response was also extrapolated by applying the procedure of Chapter 2 with MPM [5] at each of the $1,200$ positions in $\mathcal{R}$. The average CPU time required to extrapolate the response at *each* location was 8.6 min, with a total of 172 hours needed to extrapolate response at all of the $1,200$ positions in $\mathcal{R}$. Alternatively, extrapolating the spatial response with the procedure in this work required only 17 min. The dramatic time savings is due to the fact that despite the large number of positions in $\mathcal{R}$, the new procedure in this work still only requires a single GA optimization to extrapolate the response.

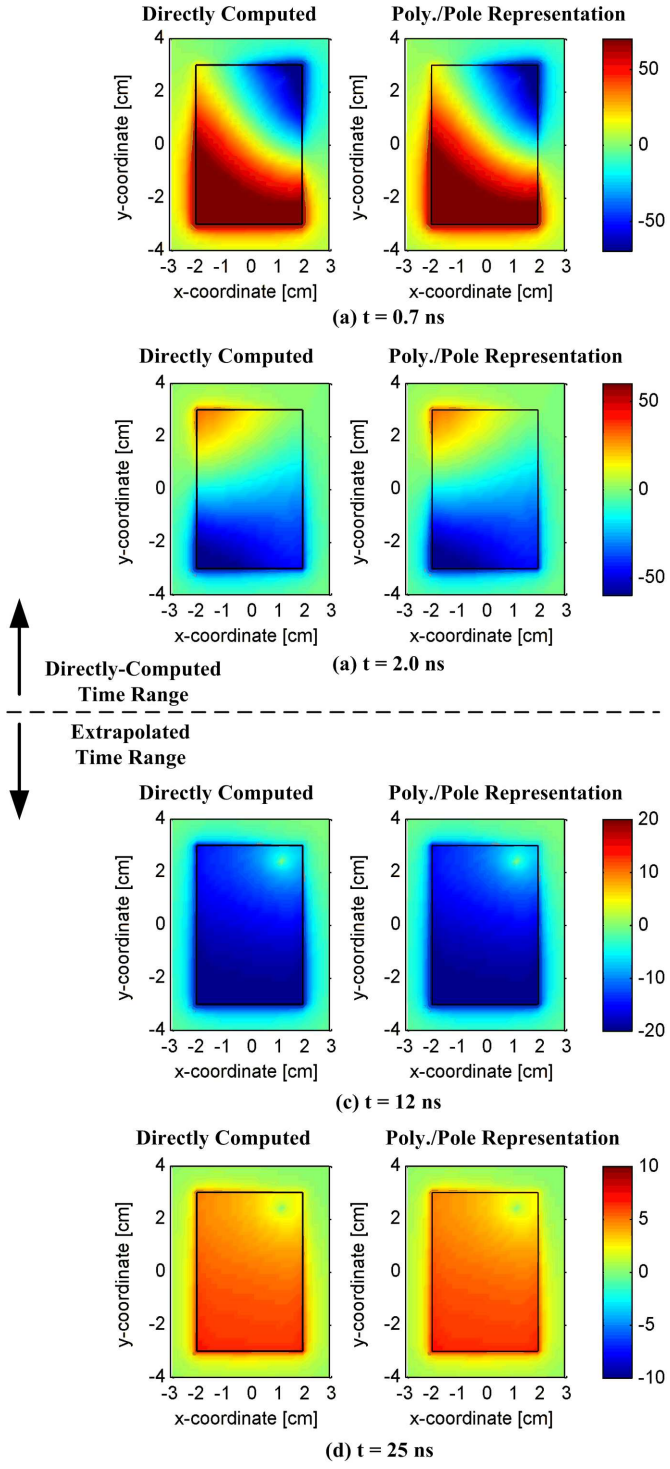

Figure 3.9**:** The $\hat{z}-$ directed electric field response of the patch antenna for (a) $t = 0.7\,\text{ns}$, (b) $t = 2.0\,\text{ns}$, (c) $t = 12\,\text{ns}$, (d) $t = 25\,\text{ns}$. The directly-computed response and a representation with polynomials and physical poles only are nearly indistinguishable indicating a successful extrapolation ($K = 10$).

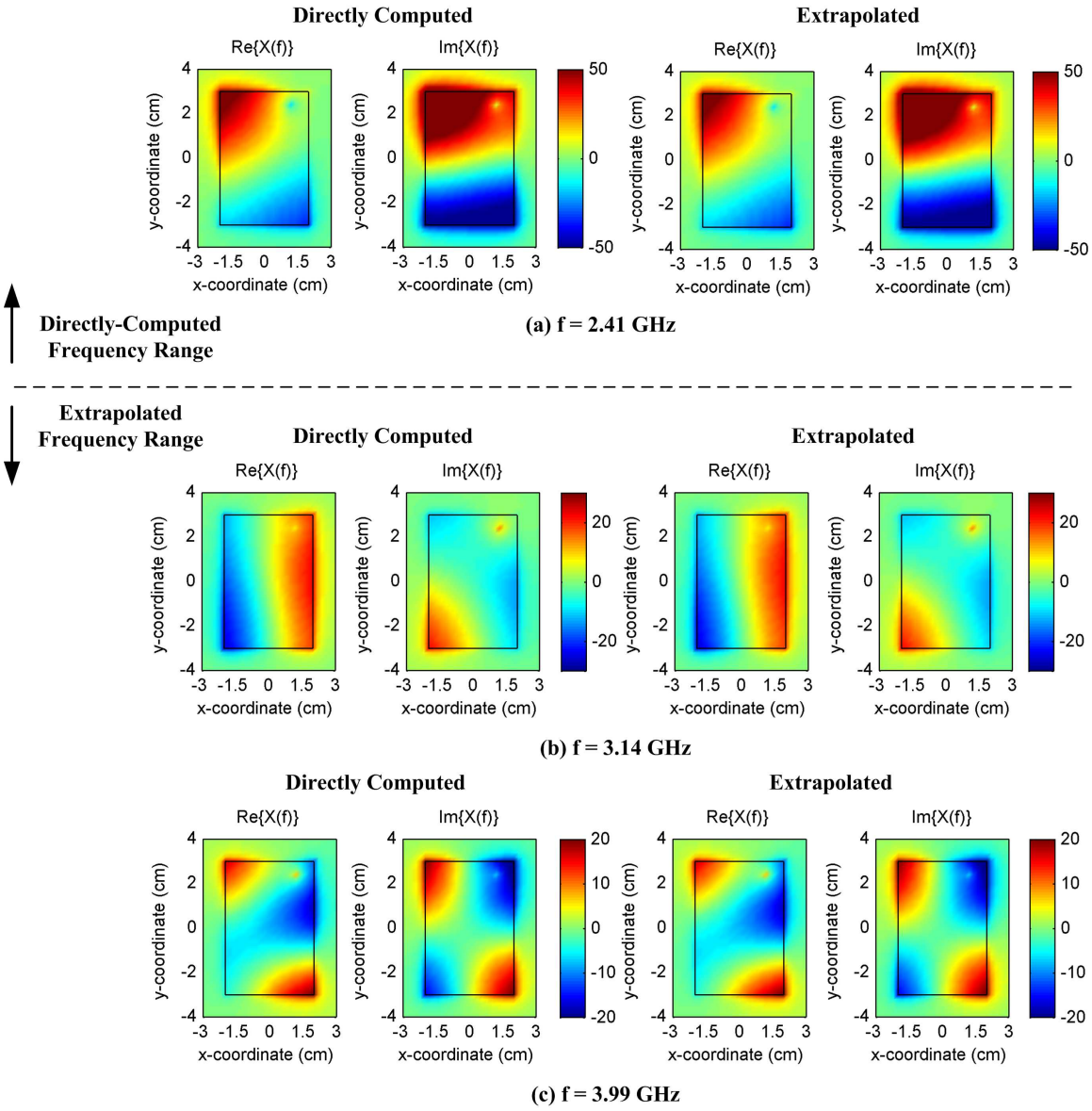

Figure 3.10**:** The $\hat{z}-$directed electric field response of the patch antenna for (a) $f = 2.41\,\text{GHz}$, (b) $f = 3.14\,\text{GHz}$, (c) $f = 3.99\,\text{GHz}$. The directly-computed response and a representation with polynomials and physical poles only are nearly indistinguishable indicating a successful extrapolation ($K = 10$).

Two representations of the reflection coefficient relative to $50\,\Omega$ at the driving point of the patch antenna are shown in Fig. 3.11. One representation is calculated directly from the DFT of the driving-point current determined with an FDTD simulation. The other representation is determined by extrapolating the driving-point current with the procedure of Chapter 2 ($10\,$ns early-time data and $2.5\,$GHz low-frequency data), and calculating the reflection coefficient from the frequency-domain representation of the extrapolated response. The agreement between the two representations is seen to be excellent.

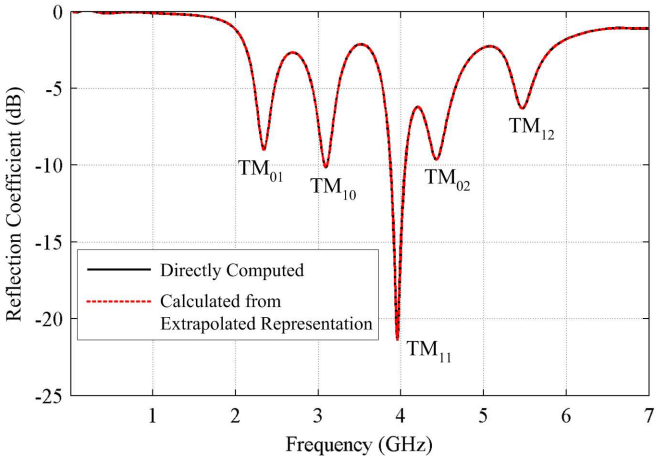

Figure 3.11: Reflection coefficient relative to $50\,\Omega$ at the driving point of the patch antenna. Each resonance is associated with the corresponding cavity mode.

For the frequency range shown in Fig. 3.11, the patch antenna radiates effectively near the five dips in the return loss. Each of these five resonances is associated with a mode of a cavity formed by the patch and ground plane. The cavity model is often used to understand the radiation of a rectangular patch antenna [46]. The dominant modes of the patch antenna, as predicted by the cavity model, are transverse magnetic to z with the resonant frequency of the TM$_{ab}$ mode

$$f_m^{(ab)} = \frac{1}{2\pi\sqrt{\mu\epsilon}}\sqrt{\left(\frac{a\pi}{A}\right)^2 + \left(\frac{b\pi}{B}\right)^2}, \tag{3.12}$$

where A and B are the dimensions of the patch in the x and y directions, respectively.

Because of the simplifying assumptions of the cavity model, the resonant frequencies of the patch antenna are not accurately predicted by (3.12); however, these frequencies can be accurately determined using the extrapolation procedure in this work. Because the antenna radiates effectively near these frequencies, their determination is valuable.

The sets of poles determined by extrapolating the response of the patch antenna by selecting parameters based on fitting at three different sets of 10 randomly-distributed positions, denoted $\mathcal{K}_1$, $\mathcal{K}_2$, and $\mathcal{K}_3$, are illustrated in Fig. 3.12. Physical poles are coincident in the three sets of poles, whereas the fitting poles are not. Each physical pole corresponds to a resonance due to a cavity mode [46].

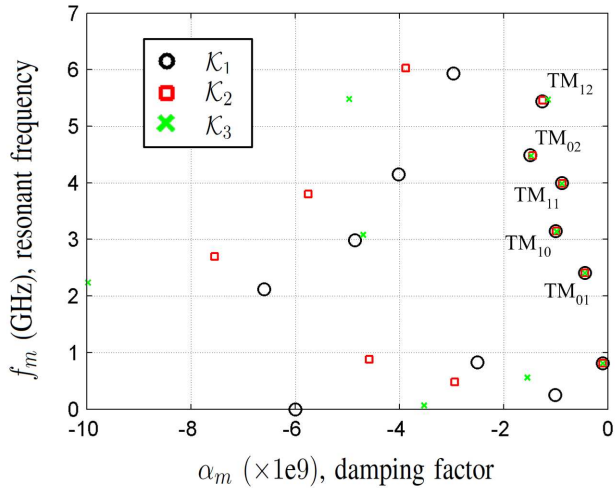

Figure 3.12**:** Poles of the patch antenna determined by fitting the response at $K = 10$ spatial locations using three different sets of K position vectors denoted $\mathcal{K}_1$, $\mathcal{K}_2$, and $\mathcal{K}_3$. Physical poles are coincident in the three sets of poles whereas the fitting pole are not.

Fig. 3.13 shows the modal residues $R_m(x, y)$ which correspond to cavity modes TM_{01}, TM_{10}, and TM_{11}. The spatial variation of the modal residues is very similar to the frequency-domain response at these resonant frequencies (compare with Fig. 3.10). The variation is also similar to the spatial variation of the corresponding cavity mode, but the modal residue is perturbed by the probe feed as expected. A response can be viewed as a superposition of physical pole terms weighted by modal residue functions. With plots like Fig. 3.13 the fundamental spatial behavior of each resonance can be examined individually to gain insight. While the rectangular patch is relatively well-understood, the procedure in this work can also be used to study other antennas and/or complex systems with unknown resonant behavior.

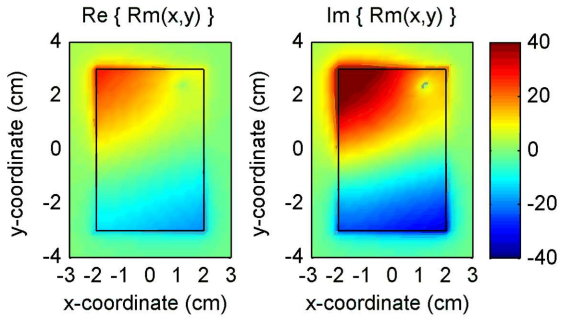

(a) TM_{01} ($f_{\mathrm{m}} = 2.41$ GHz)

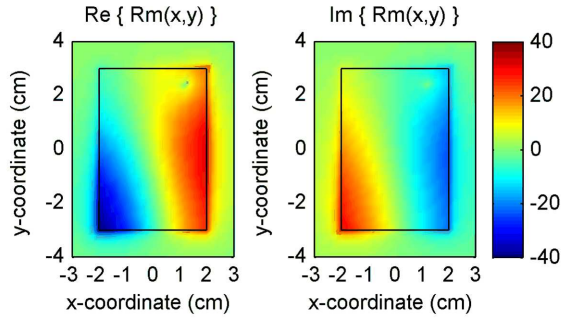

(b) TM_{10} ($f_{\mathrm{m}} = 3.14$ GHz)

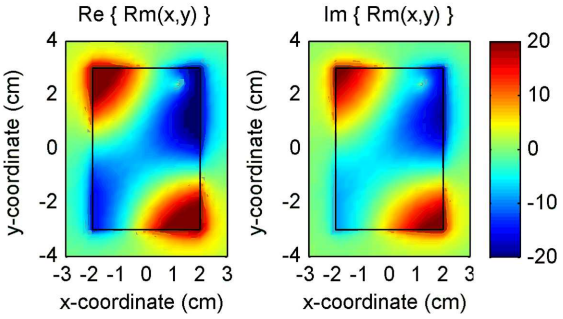

(c) TM_{11} ($f_{\mathrm{m}} = 3.99$ GHz)

Figure 3.13**:** Modal residues $R_m\,(x, y)$ of physical poles of the patch antenna associated with TM_{01}, TM_{10}, and TM_{11} cavity modes. Compare to (a), (b), and (c), respectively, of Fig. 3.10. Residues are determined by extrapolating CEM early-time and low-frequency data and representing the electric field response of the patch antenna as in (3.1).

3.6 Conclusions

A reliable and computationally-efficient procedure to extrapolate a wideband EM response defined in an arbitrary spatial region is presented in this chapter. Previously, only responses defined at a single spatial location have been considered. An automated procedure is presented which can be used to select the parameters needed to extrapolate the spatial response with a single GA optimization run. It is shown that the spatial variation of the response can be represented with spatially-dependent polynomial coefficients and pole residues, and that a single set of poles is sufficient to describe the resonant behavior of the spatial response. A new automated procedure is also presented to distinguish the physical poles of a response from the fitting poles. The physical poles of a dipole are shown to agree well with SEM poles and the physical poles of a patch antenna are shown to correspond to cavity modes. It is observed that the modal residues of physical poles can provide insight into the spatial behavior of the response at structural resonances.

CHAPTER 4
ON THE USE OF MODAL RESIDUES FOR ANTENNA ANALYSIS

Abstract

In the polynomial and pole term representation used to extrapolate a wideband spatial response, the spatially-dependent coefficients of physical pole terms, referred to as modal residues, are shown to provide valuable physical insight into the resonant behavior of a structure. While applicable in general to many different types of resonant structures, the use of modal residues to analyze arbitrarily-shaped patch antennas is described in this chapter. In chapter 3, the modal residues of a rectangular patch antenna driven by probe feed were seen to be perturbed by the location of the excitation. In this chapter, an excitation is used that excites the resonances of the patch and allows the unperturbed modal residues, which exhibit natural and perhaps symmetric modal behavior, to be determined. Unperturbed modal residues can be used to identify the influential parameters for each resonance and provide the information needed to locate a probe feed position which will excite desired resonances. It is shown that if the probe feed is located in a null of an unperturbed modal residue, the corresponding resonance will not be excited. Additionally, the spatial variation of unperturbed modal residue is similar to the input resistance at the resonant frequency as the position of the probe feed is moved. The unperturbed modal residues of several patch antenna shapes are determined to demonstrate the value of the approach.

4.1 Introduction

The use of modal residues is proposed as a tool to aid in the analysis of antennas and other resonant structures. Modal residues are spatial functions, determined by extrapolat-

ing a spatial response as described in Chapter 3, which are similar to the natural modes of the singularity expansion method (SEM) and provide valuable physical insight into resonant behavior of the structure. While analysis with modal residues is applicable to many different types of resonant structures, the analysis of patch antennas is considered here to illustrate the procedure.

A response is extrapolated by fitting early-time and low-frequency data determined with computational electromagnetic (CEM) methods to determine an accurate representation of the response as a weighted sum of polynomials and pole terms [1, 5]. Some of the poles terms in the representation, referred to as physical poles, are associated with the natural resonances of the structure. Each physical pole term is weighted by a *modal residue* which describes the spatial variation of the response at the associated resonant frequency. The set of modal residues can be viewed as a decomposition of the response into the characteristic spatial behavior of each resonance. This allows one to identify and study the resonant behavior of an arbitrarily-shaped structure, which provides physical insight that may not be readily apparent from the response in either the time or frequency domain.

By providing physical insight into complex radiation phenomenon, it is hoped that modal residues can help address the need for efficient numerical tools for the systematic and intuitive design of antennas and other resonant structures. The typical design process begins by using CEM methods to numerically model an antenna and determine its radiation properties. Often many iterations are required to obtain a satisfactory design, which may be difficult if the computational expense of the CEM simulations is great. Once a satisfactory design is found, a physical prototype is built and its performance is measured. Generally, while CEM simulations have proven to be highly accurate, the numerical data alone does not directly provide physical insight into the radiation phenomenon taking place. Optimization techniques such as the genetic algorithm (GA) [34] or particle swarm opti-

mization (PSO) [47] are often used to automate the design process and search for a set of parameters, such as the shape and dimensions of an antenna, which meet defined performance goals. While this approach has proven to be effective, no physical insight is directly gained into the operation of the antenna. Thus, the standard design process is not as conducive as possible to developing new designs or for providing a basic understanding of why a particular antenna geometry radiates effectively.

Despite the need for numerical tools to provide physical insight into an antenna and aid in the design process, relatively few techniques have been presented in the literature. One such technique is the Theory of Characteristic Modes which has been used to provide insight into the radiating phenomenon of arbitrarily-shaped wire and patch antennas by expanding the surface current of a conducting body into real-valued modes [48, 49]. An impedance matrix is determined for each frequency of interest and the modes are found by solving an eigenvalue equation. The eigenvalue associated with each mode (or eigenvector) provides information about the resonant frequency and characteristics of the mode. The insight provided by the modes has been used to select the size/shape of antennas and select an appropriate feeding point [50, 51].

The use of modal residues to analyze resonant structures is demonstrated with several patch antenna shapes: rectangle, ellipse, bowtie, triangle, and E-shaped. In Chapter 3, the spatial variation of the modal residues determined for a rectangular patch antenna are perturbed by the location of the probe feed. In this chapter, an excitation is used to generate a response without a probe feed, and the resulting *unperturbed modal residues* are seen to exhibit the appropriate symmetry.

For the analysis of patch antennas, the unperturbed modal residues of the electric field between the patch and ground plane is shown to have several valuable properties. One can quickly determine the influential parameters of each resonance, which is helpful in design

and analysis. It is shown that if the probe feed is positioned in a null of an unperturbed modal residue the corresponding resonance will not be excited, and the antenna will not radiate effectively near this resonant frequency. Thus, the nulls in the modal residues provide an easy way to determine the set of resonances that will be excited for a give probe feed location. Additionally, the variation of the input resistance at a resonant frequency as the position of the probe feed is moved is similar to the spatial variation of the unperturbed modal residue associated with that resonance. This provides valuable information as to where to search for a probe feed location that is matched to the characteristic impedance of the feed line. The procedure presented in this chapter is very general and can be applied to simple structures with well-understood resonant behavior, as well as more complex structures or systems with unknown resonant behavior.

4.2 Determining the Modal Residues of a Response

Modal residues are determined by extrapolating a spatial response with the procedure described in Chapter 3, which is briefly summarized here. Let $x(\mathbf{r},t)$ and $X(\mathbf{r},f)$ denote the time- and frequency-domain representations of a response at a spatial position $\mathbf{r}$. The response represents an EM quantity of interest defined in a spatial region $\mathcal{R}$. To extrapolate the response $x(\mathbf{r},t)$ and $X(\mathbf{r},f)$ are represented by $\hat{x}(\mathbf{r},t)$ and $\hat{X}(\mathbf{r},f)$ as

$$\begin{aligned} x(\mathbf{r},t) \approx \hat{x}(\mathbf{r},t) &= \sum_{n=0}^{N-1} a_n(\mathbf{r})\phi_n(\tfrac{t}{\ell_1}) + \sum_{m=0}^{M-1} R_m(\mathbf{r}) g_m(t) \\ X(\mathbf{r},f) \approx \hat{X}(\mathbf{r},f) &= \sum_{n=0}^{N-1} a_n(\mathbf{r})\Phi_n(\tfrac{f}{\ell_2}) + \sum_{m=0}^{M-1} R_m(\mathbf{r}) G_m(f) \end{aligned} \quad . \tag{4.1}$$

In (4.1), N and M are constants, $\phi_n(t/\ell_1)$ and $\Phi_n(f/\ell_2)$ are $n\text{th}-\text{order}$ polynomials, and the pole terms are defined as $g_m(t) = \exp(s_m t)$ and $G_m(f) = 1/(j2\pi f - s_m)$. The mth complex pole is $s_m = \alpha_m + j2\pi f_m$ where f_m is the resonant frequency and α_m is the damping factor. CEM methods are used to determine early-time and low-frequency values of $x(\mathbf{r},t)$ and $X(\mathbf{r},f)$ at discrete locations in $\mathcal{R}$, and the data are processed to determine the representation in (4.1). The set of poles $\mathbf{s}_M$ is obtained with a multi-signal variation of the matrix pencil method [38], and for each spatial location the polynomial coefficients $a_n(\mathbf{r})$ and pole residues $R_m(\mathbf{r})$ are determined by solving a system of equations that fits CEM data (equation 3.3).

The set of poles $\mathbf{s}_M$ contains both physical poles, which correspond to structural resonances, and fitting poles, which are not related to resonances but can improve the fit of the response in (4.1). The physical poles of the response can be distinguished from the fitting poles with the procedure presented in Chapter 3. If s_m is a physical pole, then it corresponds to a structural resonance with a complex frequency of $\alpha_m + j2\pi f_m$. The spatial

variation associated with this resonance is described by $R_m(\mathbf{r})$, which is referred to here as a *modal residue*. Each modal residue is defined in $\mathcal{R}$ and is not a function of time or frequency, which is evident in (4.1) as $R_m(\mathbf{r})$ appears in both the time- and frequency-domain representation of the response. The set of modal residues provides a description of the spatial variation of the response at structural resonances. Modal residues are defined for any response that can be represented as in (4.1), so the procedure is very general; however, one must be aware that the modal residues depend on the characteristics of the response from which they are determined.

For modal residues to provide physical insight and aid in analysis, one must choose a response which is appropriate for the structure of interest and carefully select the excitation and feeding arrangement. The EM quantity and the location and dimensions of $\mathcal{R}$ define the modal residues, and a response must be selected which represents the resonant behavior of the structure at a location where knowledge of this behavior will prove useful. The choice of response should be made based on the geometry of the structure and the nature of its resonances, while also keeping in mind the goal of the analysis. The electric field or surface current in a region of interest are examples of possible choices. A response is described in Section 4.4 which is useful for the analysis of patch antennas.

The choice of excitation also influences the modal residues. If a resonance is not driven by the excitation its effects will not be in the response, and the pole and modal residue corresponding to that resonance cannot be determined by extrapolating the response. It is important to understand the reasons why resonances are not driven by certain excitations. First, the bandwidth of the excitation source f_{max} limits the highest resonant frequency that can be determined by extrapolating a response, as resonances with $f_m > f_{\text{max}}$ will not be excited. Therefore, modal residues are always a bandlimited set of the resonances of the structure. Every resonance within the excitation bandwidth may not be excited by

a given excitation source or feeding arrangement. The selection of a general excitation which drives all the resonances of interest is a key component of using modal residues to analyze resonant structures, and in Section 4.4 an excitation is described which can be used to effectively analyze patch antennas.

Because modal residues depend on the response from which they are determined, the procedure presented here is fundamentally different from a typical modal technique. For example, characteristic modes and natural modes determined with SEM are independent of excitation and represent the surface current of a conducting object [50, 51, 52, 43]. Therefore, the selection of a response and excitation is not required; however, the procedure in this work offers the generality needed to consider a wide range of responses and structures. For instance, any CEM method can be used to generate the necessary data, whereas for the formulations presented in the literature both characteristic modes and SEM require one to determine the impedance matrix of the structure. The applicability of the procedure in this work is not limited by the characteristics or complexity of the structure modeled. Additionally, the representation of (4.1) can accurately approximate many different types of responses, including the effects of excitation, because it includes both pole terms and polynomials. Accurately representing the effects of excitation and early-time behavior with other modal techniques can prove to be problematic [53].

4.3 Applications of Modal Residues for the Analysis of Resonant Structures

The modal residues and physical poles of a response can provide valuable physical insight into the resonances of a structure. The set of modal residues can be viewed as a decomposition of a response into modal functions which illustrate spatial variation at each resonant frequency. The modal residues and physical poles are found to be similar to the natural modes and poles determined with SEM [43, 52]. The process to determine modal residues differs significantly from the procedures typically used with SEM; however, due to the similarity, modal residues can potentially provide the same value as natural modes.

Determining the modal residues of a response can be useful in applications where it is desired to enhance or suppress the effects of one or more resonances. In many EM applications, resonant behavior is an essential component of the radiation characteristics of structure, and thus insight into resonances is important for design and analysis. For example, designing an antenna that radiates efficiently in several frequency bands is a common objective, and in most cases multi-band behavior is attributable to the excitation of multiple structural resonances. With knowledge of the nature and influential parameters of each resonance, a designer is in a better position to interpret observed behavior and successfully modify the dimensions or feed point of a structure to best utilize the resonances to meet design goals. In EMI/EMC applications, the resonances of cavities, slots, and wires can produce strong EM coupling and field penetration into enclosures. It is critical to identify the resonances which, if properly excited, can lead to strong EM fields in sensitive areas, such as near digital circuits. Determining the salient features of a complex system often proves to be challenging; however, the modal residues of a carefully selected response may provide a valuable tool for this process. Insight into the characteristics and important parameters of each resonance may also help to determine ways to mitigate undesirable

behavior.

The insight provided by modal residues can also supplement the use of automated optimization techniques, such as the GA. In many EM applications, the GA has been applied to search for a set of parameters, such as the dimensions of an antenna, location of feed point, etc., to meet design criteria; however, decisions must be made when applying a GA which directly affect whether or not a good design will be found. Analyzing modal residues can potentially provide the insight needed to help guide the selection of which parameters should be optimized and the range of their values. Additionally, one can study modal residues to help build the intuition needed to recognize if certain geometries are capable of supporting the radiation properties required to meet a design goal. Even if a satisfactory design is found through optimization techniques, one is not directly provided with an explanation of the EM phenomenon responsible for the observed behavior. Modal residues can be used in a post-design analysis to better understand the behavior of an antenna or structure which in turn could uncover ways to improve upon a design, inspire new ideas, or to prevent unintended degraded performance caused by modifications to the structure.

4.4 Using Modal Residues to Analyze Patch Antennas

While applicable to a wide range of resonant structures, the use of modal residues for the analysis of patch antennas is considered here. The basic geometry of interest is an arbitrarily-shaped patch separated from a rectangular ground plane by a height h, which is much smaller than the dimensions of the patch. The antenna is driven by a probe feed, or via, that connects the ground plane and patch. The region between the patch and ground plane could be a dielectric material with relative permittivity ϵ_r, however, $\epsilon_r = 1$ for the examples considered here.

A response must be selected such that the modal residues provide insight into the resonances of the antenna, and to aid in this selection a general notion of the characteristics of the resonances is helpful. As discussed in Chapter 3, the resonances of a rectangular patch antenna (Fig. 4.1) can be associated with the modes of a cavity formed by the patch and ground plane [46]. Because h is small relative to the dimensions of the patch the modes of the antenna in Fig. 4.1 are TM$_z$, and the dominant field components between the patch and ground plane are E_z and the transverse magnetic fields H_x and H_y. Based on the nature of the resonances and because the probe feed is aligned in the z direction, a useful response to consider is E_z between the ground plane and patch (Fig. 4.1). The fields are mostly invariant in the z direction, and a two-dimensional region in the $xy-$ plane at $z = h/2$ is sufficient to describe the resonant behavior. This region $\mathcal{R}$ extends past the perimeter of the patch in order to include the effects of fringing fields.

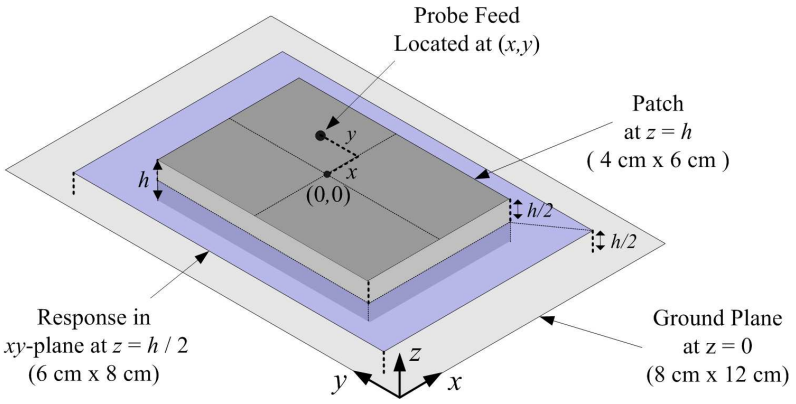

Figure 4.1**:** Geometry of a $4\,\text{cm} \times 6\,\text{cm}$ rectangular patch antenna. The $8\,\text{cm} \times 12\,\text{cm}$ ground plane is separated from the patch by $h = 0.3\,\text{cm}$. The region $\mathcal{R}$ is $6\,\text{cm} \times 8\,\text{cm}$ and centered on the patch in the $xy-$ plane at $z = h/2$. The probe feed is located at (x, y), where the center of the patch is $(0, 0)$.

The surface current evaluated at resonant frequencies is often presented in the literature to explain the behavior of a patch antenna. While the modal residues of the surface current could be determined, the modal residues of E_z are shown here to have several characteristics which are useful for analyzing patch antennas. First, E_z is a scalar quantity whereas surface current is a vector, and thus the analysis and interpretation of E_z is somewhat more straightforward. Also, the modal residues of E_z provide information relevant for positioning the probe feed to excite certain resonances. While E_z is a useful response for analyzing patch antennas, a different response may need to be considered for structures with fundamentally different resonant behavior.

The choice of excitation is important for the analysis of a patch antenna with modal residues. In Chapter 3, a rectangular patch antenna is driven by applying a voltage excitation at the base of a probe feed connecting the ground plane and patch. The spatial variation of the modal residues of E_z are consistent with that of TM_z cavity modes, but the symmetry is perturbed by the location of the probe feed (Fig. 3.13). To gain the most physical insight, it is desirable to determine *unperturbed modal residues* which exhibit the natural symmetry of the modes and are not perturbed by the specific location of the excitation. Additionally, it is important to identify *all* the resonances within the excitation bandwidth; however, a given probe feed location may only excite a subset of the resonances. An alternative excitation is considered here which addresses these limitations of the probe feed. This excitation is used for analysis only, and ultimately a probe location must be found which meets the design goals.

The excitation source must be implemented into the numerical model of the structure, and thus the CEM method dictates the source types that can be considered. In this chapter, patch antennas are modeled with the finite-difference time-domain (FDTD) method using a commercial EM solver [45]. A current source excitation available in this software is used

to drive the antenna without a probe feed by generating surface current on the conducting patch. The time-domain waveform of the excitation is a wideband differentiated Gaussian pulse (DGP). This current source is realized by specifying the values of magnetic fields in the FDTD mesh along a loop perpendicular to the patch. The values and appropriate locations of the magnetic fields are selected to satisfy the relationship $I = \oint \mathbf{H} \cdot d\mathbf{l}$. To excite all the modes of the patch antenna two magnetic field loops are specified: one in the $xz-$plane which induces $y-$directed current, and a second in the $yz-$plane which induces $x-$ directed current. Each loop extends in the z direction a single FDTD cell above and below the patch. This excitation strongly excites all the TM_z modes of the patch antenna within the excitation bandwidth, and it is found that the location of the source does not perturb the spatial distributions of the modal residues determined. Therefore, this source exhibits all the characteristics needed for the present objective. Because the location of the source does not perturb the modal residues, the exact position and length of the magnetic field loops on the patch are not critical for the purposes of this analysis; however, symmetry lines should be avoided so that each resonance is excited. In the examples of Section 4.5, the two magnetic field loops are generally centered near the edges of each patch with the length equal to half the dimension of the edge. It is important to reiterate that the source used in this work is not unique, and a different excitation could be used instead to meet the same goals and determine a complete set of unperturbed modal residues.

The spatial variation of the unperturbed modal residues illustrate the natural, symmetric characteristics of each resonance, which allows one to identify the important features and dimensions of the antenna that influence each structural resonance. If one wishes to change a resonant frequency, for example, then the modal residue associated with that resonance can be used to identify the dimension(s) which must be adjusted, while the remaining modal residues indicate if additional resonances will be affected by the change. In this way, the

"trial-and-error" approach sometimes employed can be reduced, which can decrease the number of iterations required to reach a particular goal.

Important insight into how to position the probe feed to excite a set of resonances can also be obtained from the modal residues of E_z between the patch and ground plane. If the probe feed is at a position which corresponds to a null of an unperturbed modal residue then the corresponding resonance will not be excited, and the antenna with not radiate effectively at this resonance. This allows one to easily identify the areas where the probe feed must be located to excite each of the modes of a given patch shape. Additionally, the variation of the modal residues provides valuable information which can be used to search for a probe position that is matched to the characteristic impedance of the feed line.

4.5 Numerical Examples

Example 1: Rectangular Patch Antenna

The first example considered is the rectangular patch antenna illustrated in Fig. 4.1. The region of interest $\mathcal{R}$ is in the $xy-$ plane and defined by $z = h/2$, $x \in [-3\,\text{cm}, 3\,\text{cm}]$, and $y \in [-4\,\text{cm}, 4\,\text{cm}]$. A uniform grid with $\Delta x = \Delta y = 2\,\text{mm}$ is used to discretize $\mathcal{R}$, which results in a total of 1200 spatial locations. The time-domain response is determined for each location in $\mathcal{R}$ with FDTD [45], and the frequency-domain response is the discrete Fourier transform (DFT) of the FDTD data. A frequency-domain CEM method could be used; however, the approach taken here is convenient for the present purpose. To generate the desired response in $\mathcal{R}$, two current sources are applied on the surface of the patch, as described in Section 4.4. The waveform used with the excitation is a DGP with $f_{\text{max}} = 7\,\text{GHz}$.

The dominant components of the EM fields in $\mathcal{R}$ are E_z, H_x, and H_y. Each of these field components are individually extrapolated by applying the procedure of Chapter 3 with $5\,\text{ns}$ of early-time data and $3\,\text{GHz}$ of low-frequency data. The necessary extrapolation parameters are selected by fitting at $K = 10$ locations in $\mathcal{R}$. The unperturbed modal residues of E_z are illustrated in Fig. 4.2. It is observed that the real and imaginary parts of the residues have the same variation, so only the real part of each is shown here. Additionally, the residues are normalized by setting the maximum value to unity. The appropriate natural symmetry of the TM$_z$ cavity modes is clearly observed in the spatial variation of the unperturbed modal residues. The symmetry lines and locations of nulls for each modal residue of E_z are illustrated in Fig. 4.3. As seen in Chapter 3 a probe feed perturbs the symmetry of the modal residues of E_z; however, the impressed excitation source used here imposes no hard boundary conditions on the quantity sought and generates a response which can

be extrapolated to determine the unperturbed resonant behavior. Another advantage is that this excitation excites each resonance in the band of excitation, whereas a given probe feed location may not. The spatial variation of each modal residue conveys the influential dimension(s) of each resonance. For example, increasing the patch length in y would directly affect the resonance at $2.22\,\text{GHz}$ (TM_{01}), but not the resonance at $3.15\,\text{GHz}$ (TM_{10}). Increasing the patch length in x, on the other hand, would directly affect the (TM_{10}) mode, but not the (TM_{01}) mode.

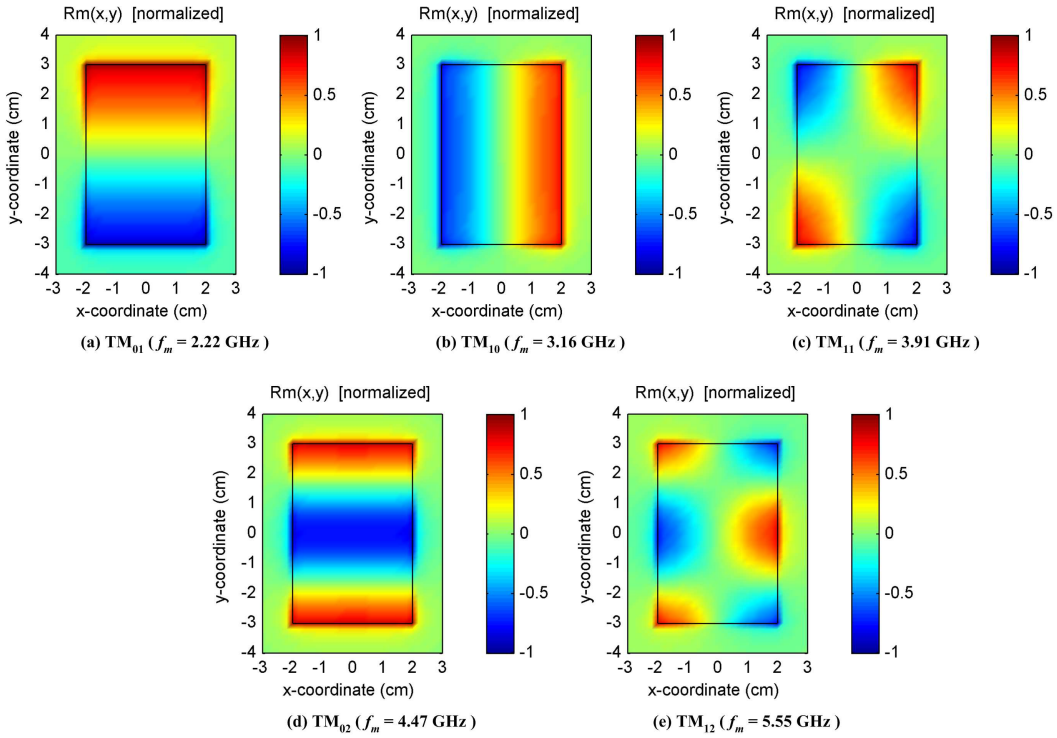

Figure 4.2**:** Unperturbed modal residues of the rectangular patch antenna determined by extrapolating E_z. The residues are associated with cavity modes (a) TM_{01}, (b) TM_{10}, (c) TM_{11}, (d) TM_{02}, and (e) TM_{12}, and clearly show the symmetric modal behavior of the electric field between the patch and ground plane (compare to the perturbed modal residues in Fig. 3.13).

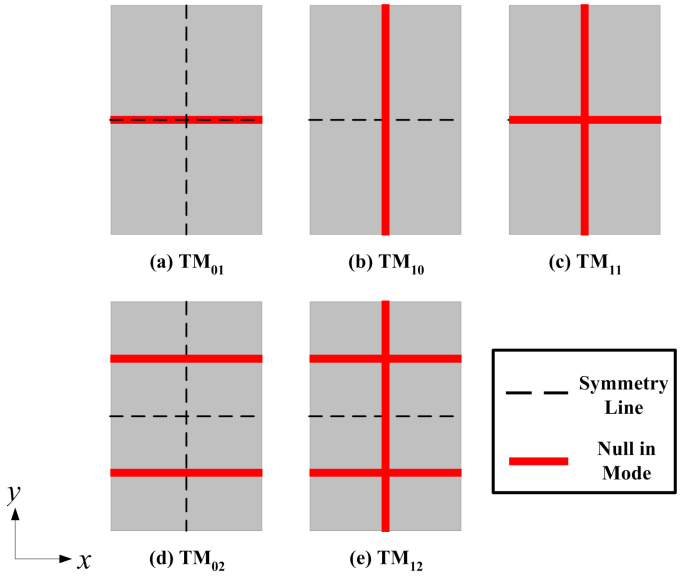

Figure 4.3**:** The locations of the nulls and symmetry lines for the unperturbed modal residues of E_z for the rectangular patch antenna (Fig. 4.2). If the probe feed of the antenna is located in a null of the a modal residue then the corresponding resonance will not be excited.

The magnetic field components H_x and H_y in $\mathcal{R}$ are separately extrapolated by applying the same excitation used for E_z. The unperturbed modal residues of H_x and H_y associated with TM_{01}, TM_{10}, TM_{11}, and TM_{02} are illustrated in Fig. 4.4. The spatial variation of the unperturbed modal residues exhibit the symmetry of the the magnetic fields between the patch and ground plane at the structural resonances of the rectangular patch. These modal residues correspond to the same resonances as the modal residues of E_z in Fig. 4.2 (a)-(d). A comparison between Fig. 4.2 and Fig. 4.4 demonstrates that modal residues are dependent on the EM quantity from which they are determined. The physical poles, on the other hand, are intrinsic to the structure and should be the same regardless of the EM quantity extrapolated. The poles determined by separately extrapolating E_z, H_x, and H_y are illustrated in Fig. 4.5. As expected the physical poles are seen to be the same for each response, whereas the fitting poles are not.

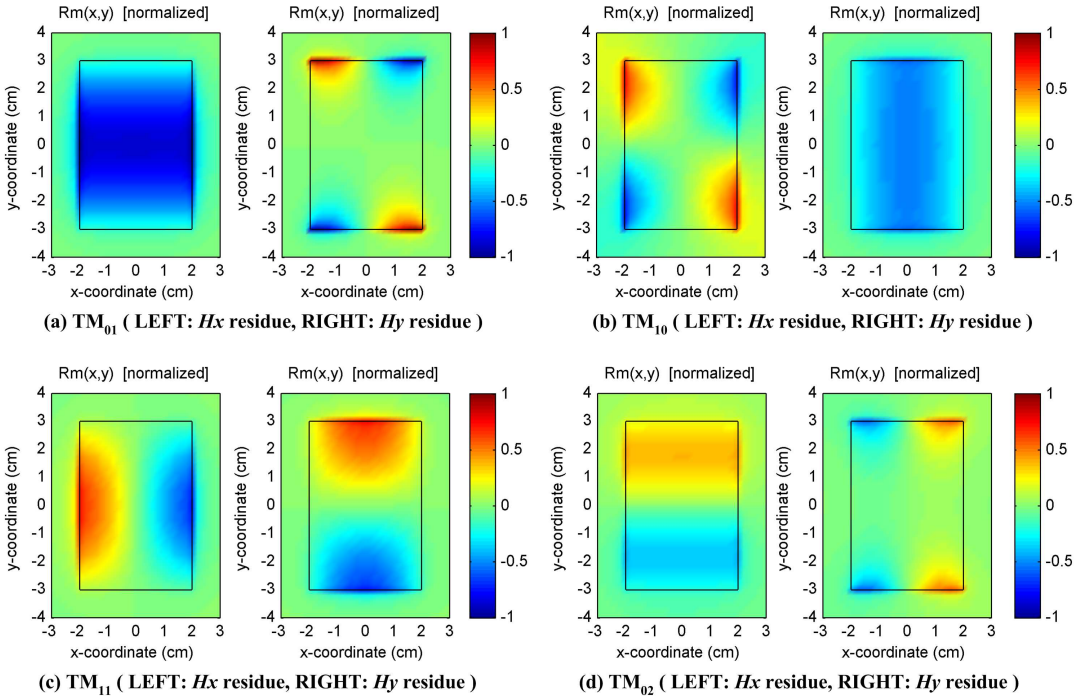

Figure 4.4**:** Unperturbed modal residues of the patch antenna determined by separately extrapolating H_x and H_y. The residues are associated with cavity modes (a) TM_{01}, (b) TM_{10}, (c) TM_{11}, and (d) TM_{02}, and clearly show the symmetric modal behavior of the magnetic fields between the patch and ground plane.

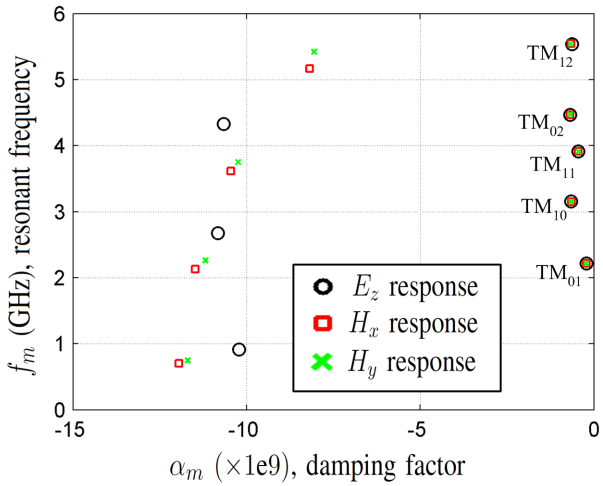

Figure 4.5**:** The sets of poles determined by separately extrapolating E_z, H_x, and H_y. The physical poles are coincident in the three sets of poles whereas the fitting poles are not.

Some valuable properties of the unperturbed modal residues of E_z are now discussed. As previously mentioned, a given location of a probe feed may not excite all the resonances of the antenna. This is illustrated in Fig. 4.6 which shows the reflection coefficient at the driving point (relative to 50Ω) versus frequency for three probe feed locations. Around resonant frequencies the reflection coefficient decreases, indicating the antenna is radiating more effectively; however, a different number of resonances are observed for each probe location. From a design perspective it is important to understand which resonances will be excited by a given probe location, and the unperturbed modal residues of E_z in Fig. 4.2 can provide this information. It is observed that if a probe feed is located in a null of an unperturbed modal residue, then the corresponding resonance is not excited. Consider the probe location at the center of the patch $(0, 0)$. Using Fig. 4.3 as a reference, the only mode without a null at the center is TM_{02}, which has a resonant frequency of 4.47 GHz. In Fig. 4.6, the reflection coefficient for the probe at $(0, 0)$ is seen to have a single resonance near 4.47 GHz. The reflection coefficient for the other two probe positions can be interpreted in a similar manner. The probe at $(0, 0.8\,\text{cm})$ is on the $y-$ axis and drives TM_{01} and TM_{02}, whereas the probe at $(0.8\,\text{cm}, 0)$ is on the $x-$ axis and drives TM_{10}, TM_{02}, and TM_{12}. The reflection coefficient for these probe positions show two and three resonances, respectively. Thus, the modal residues provide valuable insight for selecting a probe location.

The effect of the probe location on the modal residue associated with TM_{02} is illustrated in Fig. 4.7. The modal residues for three locations of the probe feed are considered, and the perturbation caused by the probe feed is apparent for each location. None of the probe positions are in a null of the unperturbed modal residue for TM_{02}, and thus each position excites the mode; however, the natural symmetry of the mode is seen to be perturbed.

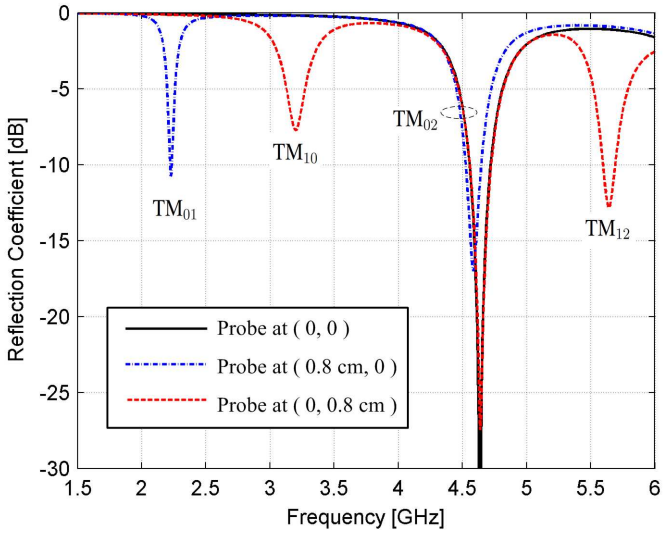

Figure 4.6**:** The reflection coefficient at the driving-point of a rectangular patch antenna for three locations of the probe feed (see Fig. 4.1). The resonances which are excited by a given probe location can be determined from the nulls of the unperturbed modal residues of E_z in Fig. 4.2.

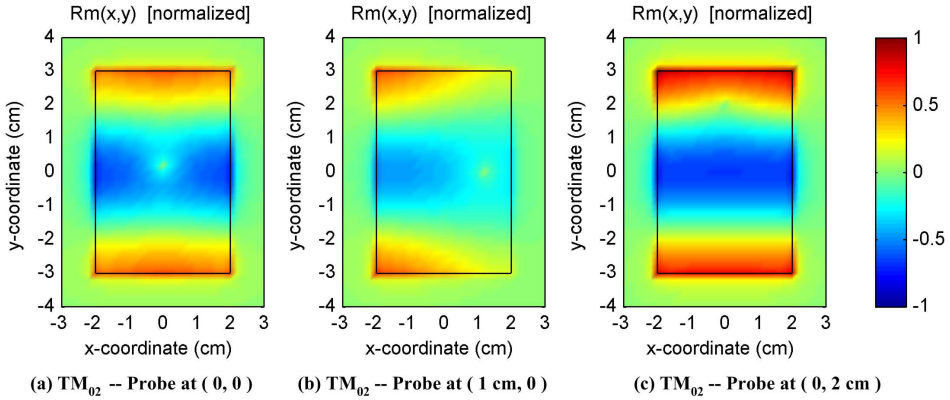

Figure 4.7**:** Modal residues of E_z associated with TM_{02} of the rectangular patch antenna for three probe-driven models. The perturbation caused by the location of the probe feed is apparent and affects the symmetry of the modal residue.

In addition to exciting a given resonance, a probe position should be matched to the characteristic impedance of the feed line. The input impedance of a probe-driven patch antenna is a function of the position of the probe, and locating a satisfactory position is often difficult. It is found here that as the position of the probe is moved, the input resistance at a resonant frequency is similar to the spatial variation of the unperturbed modal residue of E_z corresponding to that resonance. The input resistance R_{in} at three resonant frequencies $2.22\,\text{GHz}$ (TM_{01}), $3.16\,\text{GHz}$ (TM_{10}), and $4.47\,\text{GHz}$ (TM_{02}) is plotted in Fig. 4.8 as a function of the probe position. The variation of R_{in} is similar to the spatial variation of the unperturbed modal residues of E_z in Fig. 4.2(a), (b), and (d). As the probe position approaches a null of the modal residue R_{in} at the corresponding resonant frequency approaches zero, which agrees with the observation that a resonance will not be excited by a probe location in a null of a modal residue. Thus, the information gained by determining the modal residues can be useful when searching for a probe position. For example, a probe position matched to TM_{01} can be found by first choosing a value of y that achieves a desired R_{in}, such as 50Ω, then because R_{in} is relatively constant along x, the x value of the probe location can be selected such that the imaginary part of the input impedance is as close to zero as possible.

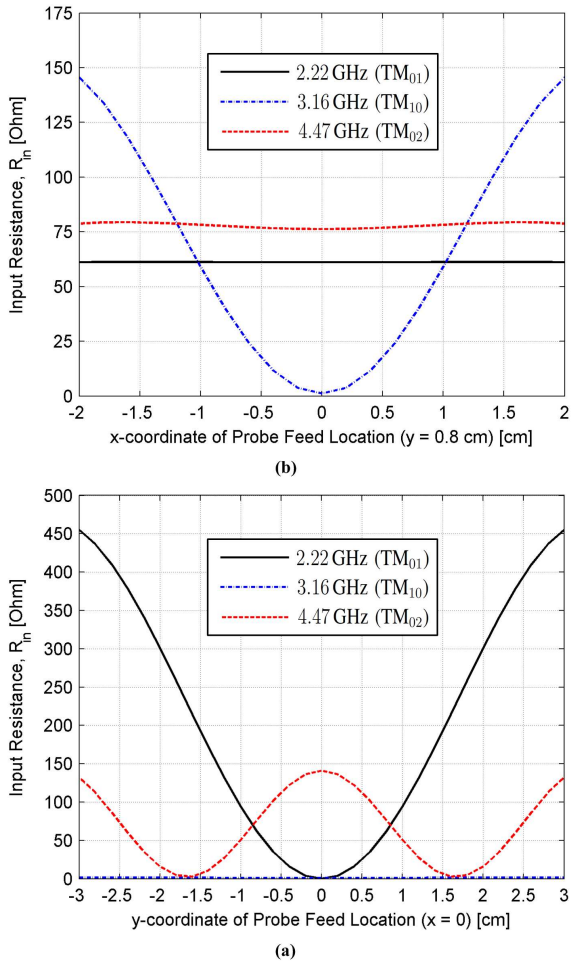

Figure 4.8**:** Input resistance, R_{in}, of rectangular antenna with probe feed positions for (a) y values along the $x-$axis and for (a) x values with $y = 0.8\,\text{cm}$. The variation of R_{in} is similar to the spatial variation of the corresponding unperturbed modal residues of E_z for TM_{01}, TM_{10}, and TM_{02} in Fig. 4.2.

Example 2: Non-Rectangular Patch Antennas (Ellipse, Bowtie, and Triangle)

The unperturbed modal residues and poles of three non-rectangular patch antennas are determined. The shapes considered are an ellipse (Fig. 4.9), a bowtie (Fig. 4.10), and a triangle (Fig. 4.11). Each patch is separated from a $6\,\text{cm} \times 6\,\text{cm}$ ground plane by $h = 0.6\,\text{cm}$, and E_z in a $5\,\text{cm} \times 5\,\text{cm}$ region between the patch and ground plane at $z = h/2$ is extrapolated. The region $\mathcal{R}$ is discretized with $\Delta x = \Delta y = 1\,\text{mm}$, which results in

$2,500$ spatial locations. Each antenna is modeled with FDTD and a current excitation is used to generate a response in $\mathcal{R}$ without a probe feed, as described in Section 4.4. The excitation waveform is a DGP with $f_{\text{max}} = 10\,\text{GHz}$, and E_z is extrapolated to determine the unperturbed modal residues. The response is sampled in the time domain at $\Delta t = 1.92\,\text{ns}$ intervals until the time response is effectively zero, and the frequency-domain response, which is sampled at $\Delta f = 10\,\text{MHz}$ intervals up to $10\,\text{GHz}$, is determined as the DFT of the time response. The response of each antenna is accurately extrapolated with $4\,\text{ns}$ of early-time data and $4\,\text{GHz}$ of low-frequency data. The necessary extrapolation parameters are selected by fitting at $K = 10$ locations in $\mathcal{R}$, as described in Chapter 3.

The unperturbed modal residues for each patch shape are shown to provide physical insight into natural resonant behavior. The spatial variation of each residue is similar to a TM_z cavity mode of a rectangular patch antenna that is perturbed by the non-rectangular shape. The input resistance R_{in} at resonant frequencies for each antenna is plotted versus the position of the probe feed. It is seen that the spatial variation of the modal residue associated with each resonant frequency has similar variation as that observed for R_{in}. Thus, the unperturbed modal residues can provide valuable information to aid in the search for a well-matched probe location. By determining the poles and modal residues of several non-rectangular patch shapes, the generality of the procedure in this work is illustrated.

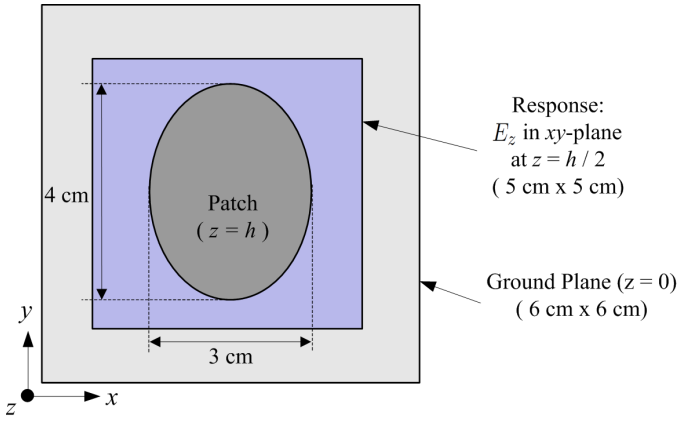

Figure 4.9: Geometry of a ellipse patch antenna ($h = 0.6$ cm).

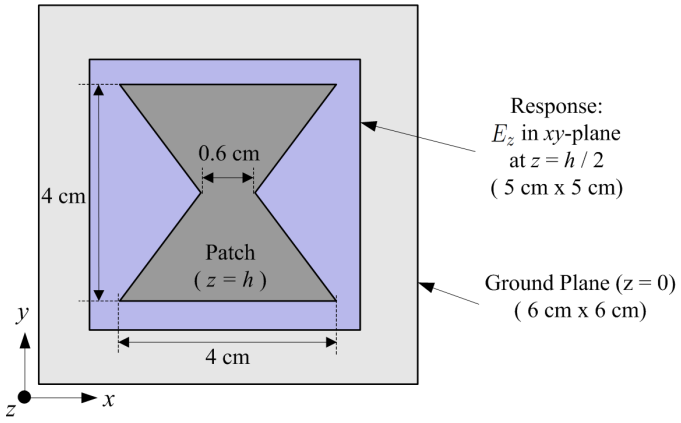

Figure 4.10: Geometry of a bowtie patch antenna ($h = 0.6$ cm).

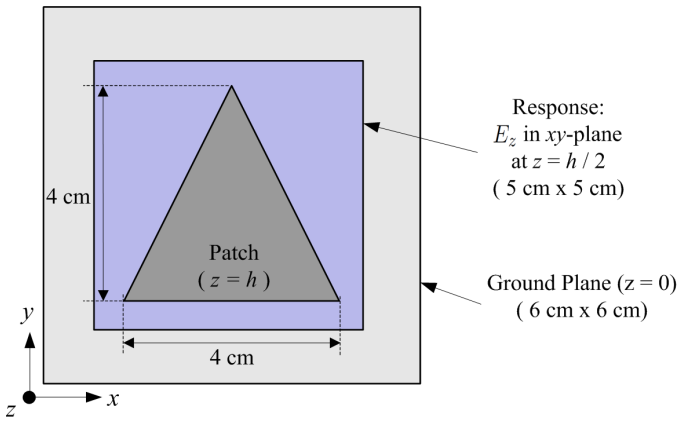

Figure 4.11: Geometry of a triangle patch antenna ($h = 0.6$ cm).

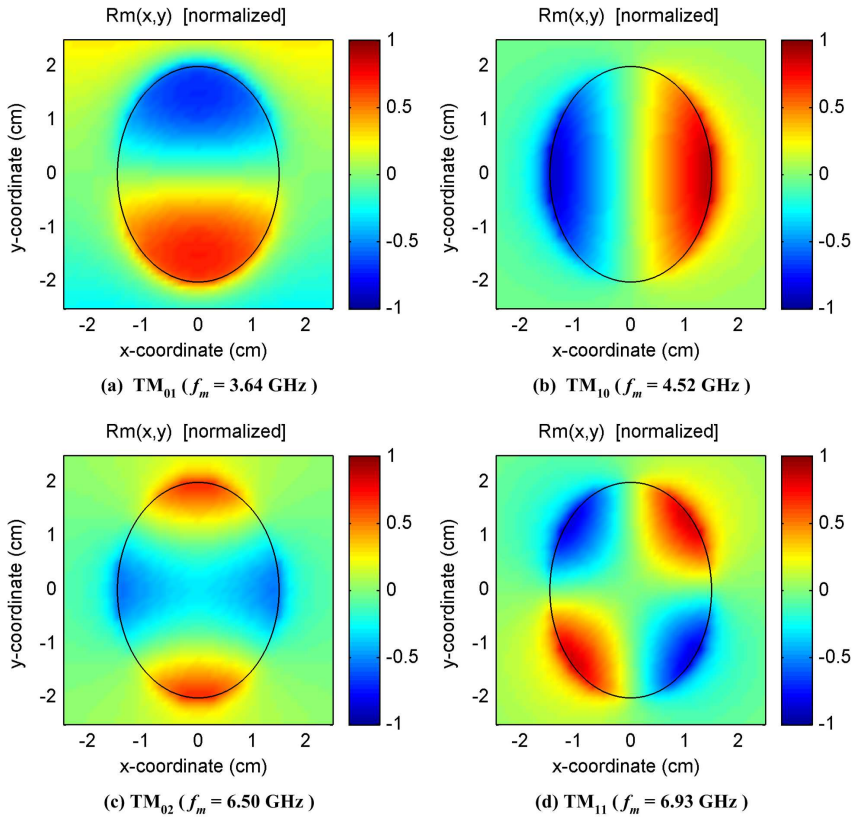

Figure 4.12**:** Unperturbed modal residues of E_z for the ellipse patch antenna in Fig. 4.9 which illustrate the modal behavior associated with (a) TM_{01}, (b) TM_{10}, (c) TM_{02}, and (d) TM_{11}.

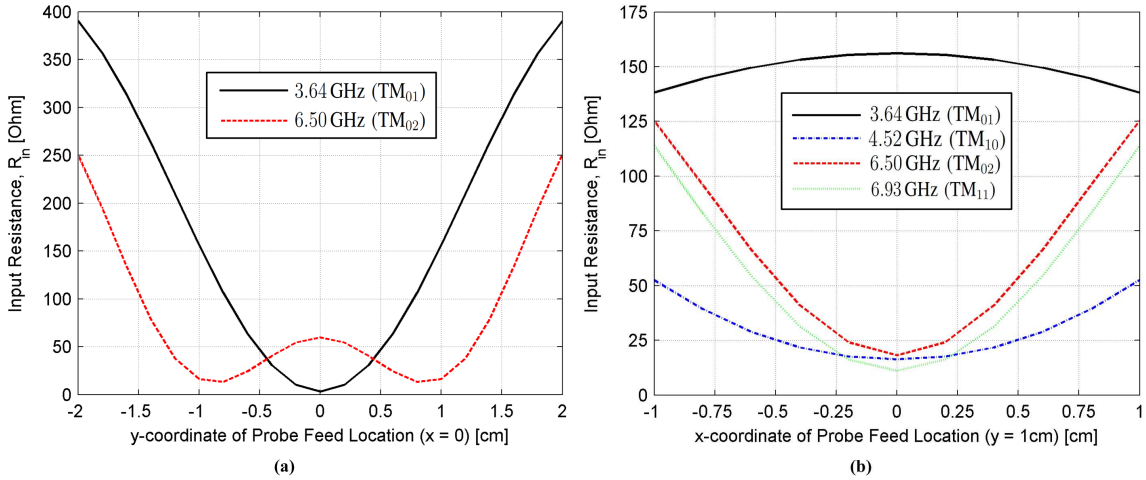

Figure 4.13**:** Input resistance, R_{in}, of the ellipse patch antenna with probe feed positions for (a) y values along the $x-$axis and for (a) x values with $y = 1.0\,\mathrm{cm}$. The variation of R_{in} is similar to the spatial variation of the modal residues of E_z in Fig. 4.12. The probe positions in (a) are in a null of TM_{10} and TM_{11} (Fig. 4.12(b) and (d)), and thus these resonances are not excited.

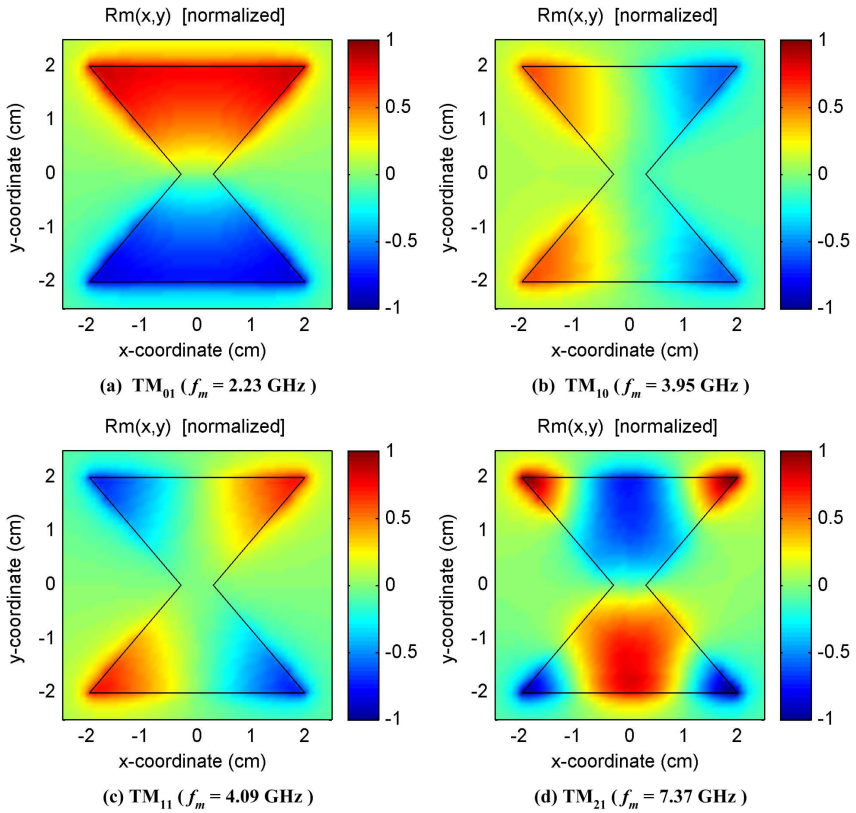

Figure 4.14**:** Unperturbed modal residues of E_z for the bowtie patch antenna in Fig. 4.10. The residues illustrate the symmetric modal behavior associated with (a) TM_{01}, (b) TM_{10}, (c) TM_{11}, and (d) TM_{21}.

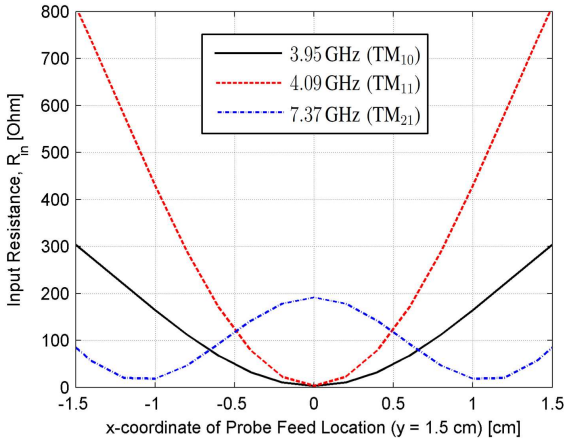

Figure 4.15**:** Input resistance, R_{in}, of the bowtie patch antenna for probe feed positions along x with $y = 1.5\,\mathrm{cm}$. The variation of R_{in} is similar to the spatial variation of the corresponding modal residues for TM_{10}, TM_{11}, and TM_{21} (Fig. 4.14(b), (c), and (d)).

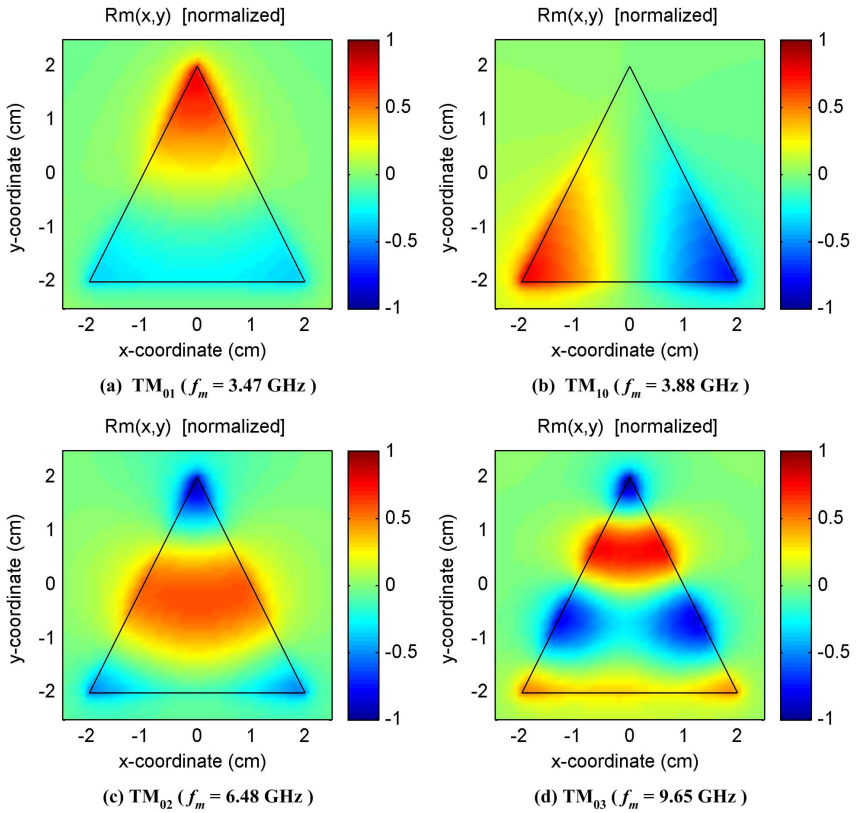

Figure 4.16**:** Unperturbed modal residues of E_z for the triangle patch antenna in Fig. 4.11. Residues illustrate the symmetric modal behavior associated with (a) TM_{01}, (b) TM_{10}, (c) TM_{02}, and (d)TM_{03}.

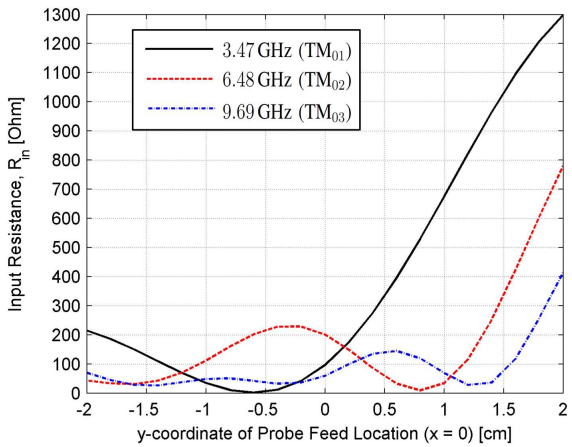

Figure 4.17**:** Input resistance, R_{in}, of the triangle patch antenna with probe feed positions for y values along the $x-$axis. The variation of R_{in} is similar to the spatial variation of the corresponding modal residues for TM_{01}, TM_{02}, and TM_{03} (Fig. 4.16(b), (c), and (d)).

Example 3: E-Shaped Patch Antenna

The final antenna considered is the E-shaped patch described in [26] and illustrated in Fig. 4.18. The unperturbed modal residues are determined by extrapolating E_z in a $9\,\text{cm} \times 7\,\text{cm}$ region ($\Delta x = \Delta y = 1\,\text{mm}$) between the E-shaped patch and ground plane at $z = h/2$ (Fig. 4.18). Three of the four modal residues (Fig. 4.19 (a), (c), and (d)) are similar to the TM_{01}, TM_{10}, and TM_{11} cavity modes of a rectangular patch antenna, respectively, whereas one resonance is due to the presence of the slots (Fig. 4.19(b)). Thus, the slots create a structural resonance which is not associated with a TM_z cavity mode. This example illustrates the generality of the approach because despite the fact that the resonance due to the slots is not a cavity mode, modal residues for each resonance are determined with the same procedure to extrapolate the response. Therefore, the procedure is not, in general, limited by the shape of the structure or the characteristics of its resonances.

The unperturbed modal residues provide physical insight into the operation of the antenna. The probe location specified in [26] excites the TM_{01} mode and the resonance due to the slots, and achieves dual-band operation at $1.9\,\text{GHz}$ and $2.4\,\text{GHz}$. By determining the unperturbed modal residues of the structure, one can identify the resonances responsible for the observed performance and any others that are supported by the structure, which could potentially lead to a new design. For example, the E-shaped patch has TM_{10} and TM_{11} resonances as well, but the probe location in Fig. 4.18 does not excite these resonances, as it is in a null of the corresponding modal residues. While these additional resonances can be used in a multi-band design, a probe location must be found which is well matched at each resonant frequency.

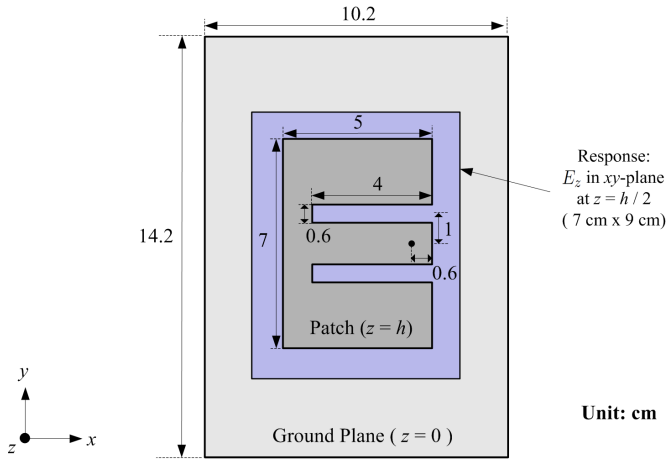

Figure 4.18**:** Geometry of the probe-driven E-shaped patch antenna ($h = 1.4$ cm).

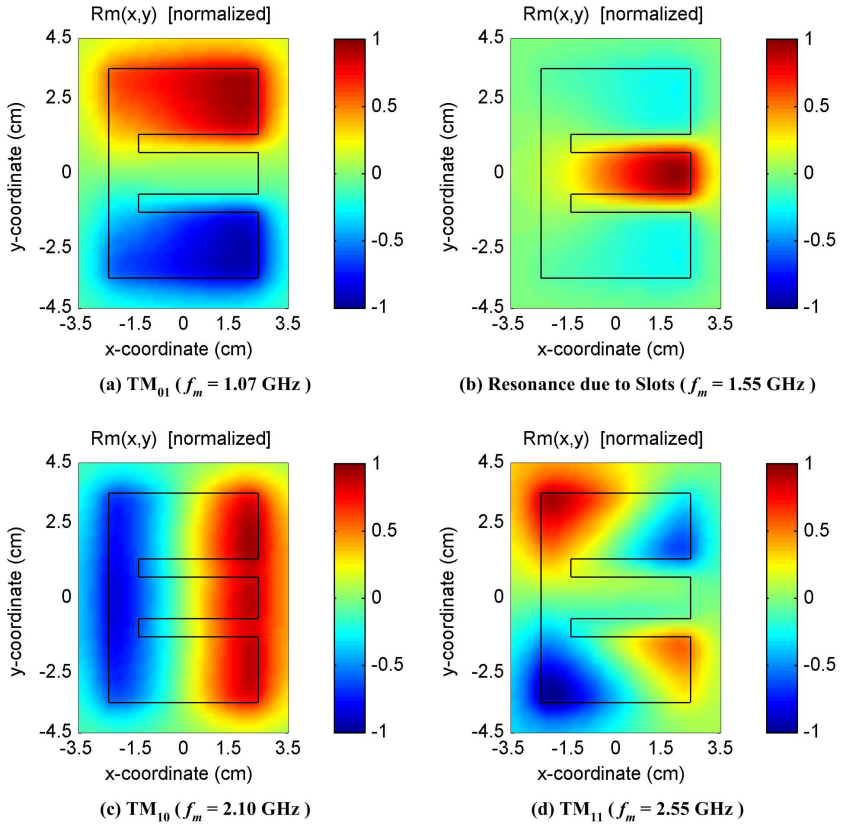

Figure 4.19**:** The unperturbed modal residues of the E-shaped patch antenna. The residues illustrate the behavior associated with cavity modes with (a) TM_{01}, (c) TM_{10}, and (d) TM_{11}, and (b) a resonance due to the slots. The probe feed location in Fig. 4.18 drives the TM_{01} mode and the resonance due to the slots.

4.6 Conclusions and Suggestions for Future Work

The use of modal residues for the analysis of resonant structure is presented in this chapter. Modal residues can provide valuable physical insight into resonant behavior, which can be very valuable in designing or understanding the EM characteristics of a structure. While applicable to many different types of resonant structures, several patch antennas are analyzed to demonstrate the approach. An excitation is used without a probe feed to determine the unperturbed modal residues, which illustrate the natural symmetry of the modes of a patch antenna. Unperturbed modal residues can be used to identify important parameters or dimensions, and also provide a straight-forward means to determine a probe position to excite a set of resonance(s). If the probe feed is located in the null of a modal residue, the corresponding resonance will not be excited. Additionally, the spatial variation of unperturbed modal residues is compared to the input resistance at resonant frequencies as the position of the probe feed is moved. The numerical examples presented demonstrate the generality of the procedure.

Several extensions to this work are apparent. First, the procedures described could be applied to design new multi-band patch antennas or to better understand and improve upon existing designs. The insight gained from the unperturbed modal residues of a structure could be utilized in conjunction with optimization techniques to devise "smarter" and more efficient ways to reach design goals. While it is shown that there is a connection between the spatial variation of unperturbed modal residues and the input resistance of a probe-driven model, a valuable contribution would be to determine how the modal residues could be used to accurately predict the value of R_{in} for any probe location on the patch. Additionally, the reactance of the input impedance must be minimal to achieve a good match, and so it would be beneficial to determine a procedure using modal residues to accurately

determine both the resistance and reactance of the input impedance at resonance frequencies.

It would also be interesting to further explore the connection between the unperturbed modal residues and the natural modes determined with a traditional SEM analysis. The procedure in this work is essentially a data-fitting approach and thus is dependent on the excitation applied, whereas the natural modes in SEM are determined as an undriven solution. While the two approaches are fundamentally different, the modes and poles determined are very similar. A further study comparing and contrasting the two approaches in terms of computational efficiency, applicability to various structures, numerical stability, etc., could provide valuable insight.

While patch antennas are used in this chapter to illustrate the procedure, other types of resonant structures could be analyzed with modal residues as well. To apply the procedure to a different type of structure one must determine an appropriate response and excitation. One relevant and potentially useful application is to use modal residues to analyze the structures of interest in EMI/EMC applications. The resonances of cavities, slots, and wires can produce strong EM fields, which can cause the disruption of sensitive digital circuits. Due to the complex interactions of the features of a system, it is often difficult to determine the influential parameters which drive the unwanted resonant behavior; however, an analysis with modal residues could potentially provide valuable physical insight to aid in this process. A complex system could be better understood using modal residues as a part of a systematic analysis procedure to identify the dominant resonances of system and determine their salient features.

REFERENCES

[1] J. Frye and A. Martin, "Extrapolation of time and frequency responses of resonant antennas using damped sinusoids and orthogonal polynomials," *IEEE Trans. Antennas Propag.*, vol. 56, no. 4, pp. 933–943, April 2008.

[2] M. Rao, T. Sarkar, T. Anjali, and R. Adve, "Simultaneous extrapolation in time and frequency domains using Hermite expansions," *IEEE Trans. Antennas Propag.*, vol. 47, no. 6, pp. 1108–1115, Jun 1999.

[3] M. Rao, T. Sarkar, R. Adve, T. Anjali, and J. Callejon, "Extrapolation of electromagnetic responses from conducting objects in time and frequency domains," *IEEE Trans. Microw. Theory Tech.*, vol. 47, no. 10, pp. 1964–1974, Oct 1999.

[4] M. Yuan, J. Koh, T. Sarkar, W. Lee, and M. Salazar-Palma, "A comparison of performance of three orthogonal polynomials in extraction of wide-band response using early time and low frequency data," *IEEE Trans. Antennas Propag.*, vol. 53, no. 2, pp. 785–792, Feb. 2005.

[5] J. Frye and A. Martin, "Time and frequency bias in extrapolating wideband responses of resonant structures," *IEEE Trans. Antennas Propag.*, vol. 57, no. 12, pp. 3934–3941, Dec. 2009.

[6] ——, "Bias in extrapolating responses from resonant structures using early-time and low-frequency data," *Proc. IEEE AP-S Society Int. Symp.*, June 2009.

[7] ——, "Extrapolation of electromagnetic responses of resonant structures," *Proc. IEEE AP-S Society Int. Symp.*, pp. 53–56, June 2007.

[8] ——, "Efficient extrapolation of wideband responses of highly resonant antennas and structures via a damped sinusoid and orthogonal polynomial expansion technique," *IEEE AP-S Int. Symp. and USNC/URSI Radio Science Meeting*, June 2006.

[9] T. Sarkar and O. Pereira, "Using the matrix pencil method to estimate the parameters of a sum of complex exponentials," *IEEE Trans. Magn.*, vol. 37, no. 1, pp. 48–55, Feb 1995.

[10] W. Ko and R. Mittra, "A combination of FD-TD and Prony's methods for analyzing microwave integrated circuits," *IEEE Trans. Microw. Theory Tech.*, vol. 39, no. 12, pp. 2176–2181, Dec 1991.

[11] Z. Bi, Y. Shen, K. Wu, and J. Litva, "Fast finite-difference time-domain analysis of resonators using digital filtering and spectrum estimation techniques," *IEEE Trans. Microw. Theory Tech.*, vol. 40, no. 8, pp. 1611–1619, Aug 1992.

[12] A. Shaw and K. Naishadham, "ARMA-based time-signature estimator for analyzing resonant structures by the FDTD method," *IEEE Trans. Antennas Propag.*, vol. 49, no. 3, pp. 327–339, Mar 2001.

[13] Y. Wang and H. Ling, "Multimode parameter extraction for multiconductor transmission lines via single-pass FDTD and signal-processing techniques," *IEEE Trans. Microw. Theory Tech.*, vol. 46, no. 1, pp. 89–96, Jan 1998.

[14] C. Christopoulos, *The Transmission-Line Modeling Method*. New York, NY: IEEE Press., 1995.

[15] R. F. Harrington, *Field Computation by Moment Methods*. Piscataway, NJ: IEEE Press, 1993.

[16] G. H. Golub and C. F. V. Loan, *Matrix Computations*. Baltimore, MD: Johns Hopkins Univ. Press., 1991.

[17] T. K. Sarkar, J. Koh, W. Lee, and M. Salazar-Palma, "Analysis of electromagnetic systems irradiated by ultra-short ultra-wide-band pulse," *Meas. Sci. Technol.*, vol. 12, pp. 1757–1768, Oct 2001.

[18] M. Yuan, A. De, T. Sarkar, J. Koh, and B. H. Jung, "Conditions for generation of stable and accurate hybrid TD-FD MoM solutions," *IEEE Trans. Microw. Theory Tech.*, vol. 54, no. 6, pp. 2552–2563, June 2006.

[19] J.-L. Hu, C. H. Chan, and T. Sarkar, "Optimal simultaneous interpolation/extrapolation algorithm of electromagnetic responses in time and frequency domains," *IEEE Trans. Microw. Theory Tech.*, vol. 49, no. 10, pp. 1725–1732, Oct 2001.

[20] P. Kozakowski and M. Mrozowski, "Low-order models from fd-td time samples," *IEEE Microw. Wireless Compon. Lett.*, vol. 12, no. 11, pp. 438–440, Nov 2002.

[21] X. Luo, M. Li, and J. Drewniak, "Time history extrapolation for FDTD modeling of shielding enclosure designs and EMI antenna geometries," *1998 IEEE Int. Sym. Electromagn. Compat.*, vol. 2, pp. 1172–1177 vol.2, Aug 1998.

[22] S. Rao, D. Wilton, and A. Glisson, "Electromagnetic scattering by surfaces of arbitrary shape," *IEEE Trans. Antennas Propag.*, vol. 30, no. 3, pp. 409–418, May 1982.

[23] S. Makarov, *Antenna and EM Modeling with MATLAB*. New York, NY: Wiley, 2002.

[24] A. Taflove and S. Hagness, *Computational Electrodynamics: The Finite-Difference Time-Domain Method*. Boston, MA: Artech House, 2000.

[25] J. Jin, *The Finite Element Method in Electromagnetics*. New York, NY: Wiley, 2002.

[26] F. Yang, X.-X. Zhang, X. Ye, and Y. Rahmat-Samii, "Wide-band E-shaped patch antennas for wireless communications," *IEEE Trans. Antennas Propag.*, vol. 49, no. 7, pp. 1094–1100, Jul 2001.

[27] T. Hikage, M. Omiya, and K. Itoh, "Considerations on performance evaluation of cavity-backed slot antenna using the FDTD technique," *IEEE Trans. Antennas Propag.*, vol. 49, no. 12, pp. 1712–1717, Dec 2001.

[28] L. Lo Conte, R. Merletti, and G. Sandri, "Hermite expansions of compact support waveforms: applications to myoelectric signals," *IEEE Trans. Biomed. Eng.*, vol. 41, no. 12, pp. 1147–1159, Dec. 1994.

[29] M. Abramowitz and I. Stegun, *Handbook of Mathematical Functions with Formulas, Graphs, and Mathematical Tables*. New York: Dover, 1965.

[30] B. Gustavsen and A. Semlyen, "Rational approximation of frequency domain responses by vector fitting," *IEEE Trans. Power Del.*, vol. 14, no. 3, pp. 1052–1061, Jul 1999.

[31] M. Sarto, "A new model for the FDTD analysis of the shielding performances of thin composite structures," *IEEE Trans. Electromagn. Compat.*, vol. 41, no. 4, pp. 298–306, Nov 1999.

[32] G. Antonini, "SPICE equivalent circuits of frequency-domain responses," *IEEE Trans. Electromagn. Compat.*, vol. 45, no. 3, pp. 502–512, Aug. 2003.

[33] V. Okhmatovski and A. Cangellaris, “Evaluation of layered media Green’s functions via rational function fitting,” *IEEE Microw. Wireless Compon. Lett.*, vol. 14, no. 1, pp. 22–24, Jan. 2004.

[34] Y. Rahmat-Samii and E. Michielssen, Eds., *Electromagnetic Optimization by Genetic Algorithms*. New York, NY: Wiley, 1999.

[35] S. Polstyanko, R. Dyczij-Edlinger, and J.-F. Lee, “Fast frequency sweep technique for the efficient analysis of dielectric waveguides,” *IEEE Trans. Microw. Theory Tech.*, vol. 45, no. 7, pp. 1118–1126, July 1997.

[36] C. Houck, J. Joines, and M. Kay, “A genetic algorithm for function optimization: a matlab implementation,” North Carolina State University, Raleigh, NC, Technical Report NCSU-IE-TR-95-09, 1995.

[37] M. Li, J. Nuebel, J. Drewniak, R. DuBroff, T. Hubing, and T. van Doren, “EMI from cavity modes of shielding enclosures-FDTD modeling and measurements,” *IEEE Trans. Electromagn. Compat.*, vol. 42, no. 1, pp. 29–38, Feb 2000.

[38] T. Sarkar, S. Park, J. Koh, and S. Rao, “Application of the matrix pencil method for estimating the SEM (singularity expansion method) poles of source-free transient responses from multiple look directions,” *IEEE Trans. Antennas Propag.*, vol. 48, no. 4, pp. 612–618, Apr 2000.

[39] J. F. Callejn, A. R. Bretones, and R. G. Martin, “On the application of parametric models to the transient analysis of resonant and multiband antennas,” *IEEE Trans. Antennas Propag.*, vol. 46, no. 3, pp. 312–317, Mar 1998.

[40] A. Driouach, A. R. Bretones, and R. G. Martin, “Application of parametric models to

inverse scattering problems," *IEE Proc.-Micvow. Antennas Propag.*, vol. 143, no. 1, pp. 31–, Feb 1996.

[41] N. Fichtner, U. Siart, Y. Kuznetsov, A. Baev, and P. Russer, "TLM modeling and system identification of optimized antenna structures," *Adv. Radio Sci.*, vol. 6, pp. 45–48, 2008.

[42] M. Van Blaricum and R. Mittra, "A technique for extracting the poles and residues of a system directly from its transient response," *IEEE Trans. Antennas Propag.*, vol. 23, no. 6, pp. 777–781, Nov 1975.

[43] F. Tesche, "On the analysis of scattering and antenna problems using the singularity expansion technique," *IEEE Trans. Antennas Propag.*, vol. 21, no. 1, pp. 53–62, Jan 1973.

[44] *Clemson University's Palmetto Cluster, http://citi.clemson.edu/palmetto*.

[45] *GEMS Software (General Electromagnetic Simulator), http://www.2COMU.com*.

[46] C. Balanis, *Antenna Theory: Analysis and Design*. New York, NY: Wiley, 1997.

[47] J. Robinson and Y. Rahmat-Samii, "Particle swarm optimization in electromagnetics," *IEEE Trans. Antennas Propag.*, vol. 52, no. 2, pp. 397–407, Feb. 2004.

[48] R. Harrington and J. Mautz, "Theory of characteristic modes for conducting bodies," *IEEE Trans. Antennas Propag.*, vol. 19, no. 5, pp. 622 – 628, Sep. 1971.

[49] ——, "Computation of characteristic modes for conducting bodies," *IEEE Trans. Antennas Propag.*, vol. 19, no. 5, pp. 629 – 639, Sep. 1971.

[50] M. Cabedo-Fabres, E. Antonino-Daviu, A. Valero-Nogueira, and M. Bataller, “The theory of characteristic modes revisited: A contribution to the design of antennas for modern applications,” *IEEE Antennas Propag. Mag.*, vol. 49, no. 5, pp. 52–68, Oct. 2007.

[51] E. Antonino-Daviu, M. Fabres, M. Ferrando-Bataller, and V. Penarrocha, “Modal analysis and design of band-notched uwb planar monopole antennas,” *IEEE Trans. Antennas Propag.*, vol. 58, no. 5, pp. 1457–1467, May 2010.

[52] C. Baum, “The singularity expansion method: Background and developments,” *IEEE Antennas Propag. Soc. Newsletter*, vol. 28, no. 4, pp. 14–23, Aug 1986.

[53] E. Heyman and L. Felsen, “A wavefront interpretation of the singularity expansion method,” *IEEE Trans. Antennas Propag.*, vol. 33, no. 7, pp. 706 – 718, jul 1985.